



ALMA MATER STUDIORUM
UNIVERSITÀ DI BOLOGNA

DEPARTMENT OF INDUSTRIAL ENGINEERING - DIN

SECOND CYCLE MASTER'S DEGREE in
AEROSPACE ENGINEERING Class LM-20
Aeronautics curriculum

Numerical Aeroacoustic Investigation of the Phase Shift Method for Multicopter Directional Noise Reduction

Dissertation in Applied Aerodynamics

Supervisor:

Prof. Gabriele Bellani

Co-Supervisors:

Dr.-Ing. Jianping Yin

Dr.-Ing. Thorsten Schwarz

Candidate:

Francesco Sessini

Examiner:

Prof. Dr.-Ing. Jan Delfs

Graduation session of March 2025
Academic Year 2023/24

In collaboration with:



DLR - German Aerospace Center

Institute of Aerodynamics and Flow Technology - Helicopter Department

Braunschweig, Germany

Abstract

This thesis presents a numerical investigation of the phase shift method applied to directional noise reduction in multirotor configurations with collective pitch control. To this end, a simulation toolchain was developed, integrating the unsteady free-wake panel code *UPM* for aerodynamic analysis and the Ffowcs Williams-Hawkings acoustic solver *APSIM* for noise prediction, developed by the German Aerospace Center (DLR) Institute of Aerodynamics and Flow Technology. The methodology was validated by reproducing experimental results from the NASA Langley research center on rotor phase shifting for hovering propellers, accurately capturing the polar distribution of sound pressure levels and the radiated sound power.

The validated toolchain was then applied to manned size quad-rotor and hexa-rotor configurations in trimmed forward flight. Rotor phase angles were optimized to reduce noise in designated ground regions. Acoustic pressure calculations at a ground plane 150m below the vehicle demonstrated that optimized phase angles effectively redirected noise away from targeted areas, achieving up to 10dB reductions in average sound pressure level compared to a baseline of 70dB corresponding to the case with unsynchronized rotors.

Spectral and time-domain analyses revealed that the phase shift method predominantly affects the blade passing frequency and its first three harmonics. The time histories of pressure fluctuations at selected observers, showing the contribution of the single rotors, revealed that noise canceling is enhanced by the symmetry of the configuration when applied to the front region, while its efficacy is somewhat reduced in the side regions.

These findings support rotor phase synchronization as a viable noise control strategy for multirotor aircraft, capable of steering sound emission away from sensitive areas without affecting the aircraft performance and avoiding the need to modify the flight path.

Acknowledgments

The research conducted in this thesis was hosted by the Helicopter department in the Institute of Aerodynamics and Flow Technology at the DLR site in Braunschweig, and it would not have been possible without Dr. Thorsten Schwarz, who believed in the project and provided his full support, for which I am truly thankful.

I am deeply grateful to my supervisor at DLR, Dr. Jianping Yin, for his constant guidance and support throughout every phase of this work, and to my university supervisor, Prof. Gabriele Bellani, for his precious assistance in the writing of this thesis.

A warm thank you goes to all members of the Helicopter department, for welcoming me and my colleagues as part of the team and providing help whenever needed. In particular, I wish to thank Gunther Wilke, who kindly provided me with his optimization algorithm for the purpose of this work, and dedicated a fair amount of his time in helping me understand it.

Finally, a special mention goes to my colleagues Diego Donnini and Aldo Chella, who shared this journey with me through both its challenges and its most rewarding moments. I am truly grateful for the opportunity to collaborate on this research and most of all for the wonderful friendship we built along the way.

Contents

1	Introduction	1
1.1	Electric VTOL aircraft	1
1.2	Rotorcraft noise	3
1.3	Noise reduction through rotor phase shifting	4
1.4	Scope of the thesis	5
1.5	Thesis layout	6
2	Theoretical background	7
2.1	Basics of Aeroacoustics	7
2.1.1	What is sound?	8
2.1.2	Derivation of the linear wave equation	9
2.1.3	Solutions to the wave equation and the multipole approximation	10
2.1.4	Acoustic sources of propellers and rotors	13
2.1.5	FFowcs William-Hawkings equation and the Farassat formulation	14
2.1.6	APSIM: Aeroacoustic Prediction System based on an Integral Method	17
2.2	Introduction to potential flow solvers	18
2.2.1	Governing equations	18
2.2.2	Panel methods	20
2.2.3	Vortex methods for rotor aerodynamics	21
2.2.4	UPM: Unsteady Panel Method	23
3	Methodology	27
3.1	Description of the simulation tool-chain	27
3.1.1	Vehicle trim procedure	28
3.1.2	Aerodynamic simulation	29
3.1.3	Acoustic simulation	31
3.2	Multirotor aerodynamic model	32
3.2.1	Rotor geometry and scaling	32
3.2.2	Parametric vehicle configuration	33
3.3	Flyover simulation setting	35
3.4	Optimization of rotor phases for directional noise reduction	36
3.4.1	Fast aeroacoustic simulation with single rotor aerodynamic solution	37
3.4.2	Surrogate based optimization	38
3.5	Calculation of sound power and far-field approximation	38
4	Validation of the method with experimental data	40
4.1	Description of the NASA experimental setup and numerical model	40
4.1.1	Experimental setup	40
4.1.2	Data post-processing	41

CONTENTS

4.1.3	Mathematical model	42
4.2	Comparison with experimental results	42
4.2.1	Convergence of calculated rotor mean thrust	42
4.2.2	Polar distribution of the overall sound pressure level	44
4.2.3	Radiated sound power	47
4.3	Effect of compactness ratio on radiated sound power	50
5	Results of phase shifting for directional noise reduction in forward flight	52
5.1	Source directivity and noise carpets	52
5.2	Pressure time series and frequency spectra	56
5.3	Discussion	63
	Conclusions	65
	Bibliography	67
A	Appendix	70
A.1	Results of the aerodynamic simulations in forward flight	70

List of Figures

1.1	Current examples of multirotor eVTOL aircraft.	2
1.2	Compound eVTOL from Airbus: CityAirbus NextGen.	3
1.3	Current examples of vectored thrust eVTOL aircraft.	3
1.4	Phase shifting concept scheme applied to a multirotor.	5
2.1	Numerical model of the blade and the wake in the free-wake panel method.	23
2.2	Induced velocity of 2D vortex singularity calculated with different viscous core models.	26
3.1	Representation of the rotor phase convention.	30
3.2	The two bladed rotor geometry.	33
3.3	Radial distributions of the rotor blade chord and twist (pitch) angle.	34
3.4	Rendering of the blade mesh used as UPM input.	34
3.5	Parametric rotor layouts.	35
3.6	Acoustic simulation setting in flyover.	36
4.1	Scheme of the NASA experimental setup.	41
4.2	Complete thrust timeseries of the isolated single rotor UPM simulation.	43
4.3	Snapshot of the developed wake from the isolated single rotor, at the last time step.	44
4.4	Thrust time-series for the last revolution as calculated by UPM and the corresponding moving averages, for each of the test cases of the double rotor experiment.	45
4.5	Rotor disc contour plot of percentage thrust difference between side by side counter-rotating rotors with a phase difference $\Delta\Psi = 90^\circ$ and the isolated one.	46
4.6	Snapshot of the developed wake from the two side by side counter-rotating rotors with phase shift $\Delta\Psi = 90^\circ$	46
4.7	Sound pressure level in [dB], plotted as a polar line against the azimuthal angle, at an elevation angle of 0° , for the double rotor experiment.	48
4.8	Sound pressure level in [dB], plotted as a polar line against the azimuthal angle, at an elevation angle of -45° , for the double rotor experiment.	49
4.9	Sound power level contours for a pair of co-rotating rotors (left) and counter-rotating (right).	51
5.1	Comparison of the average noise level calculated over the considered ground regions between the reference and the result of optimized phase shifting.	52
5.2	Contours of the SPL over the ground plane for the reference case with unsynchronized rotors, and for test cases conducted with optimized rotor phases.	55
5.3	Polar SPL directivity of the quad-rotor in forward flight for the reference case with unsynchronized rotors, and for test cases conducted with optimized rotor phases.	56
5.4	Polar SPL directivity of the hexa-rotor in forward flight for the reference case with unsynchronized rotors, and for test cases conducted with optimized rotor phases.	57

LIST OF FIGURES

5.5	Acoustic spectrum and pressure fluctuations over one rotation period at chosen observer locations for the quad-rotor in forward flight with rotor phases optimized to reduce noise in the front ground region.	59
5.6	Acoustic spectrum and pressure fluctuations over one rotation period at chosen observer locations for the quad-rotor in forward flight with rotor phases optimized to reduce noise in the port side ground region.	60
5.7	Acoustic spectrum and pressure fluctuations over one rotation period at chosen observer locations for the hexa-rotor in forward flight with rotor phases optimized to reduce noise in the front ground region.	61
5.8	Acoustic spectrum and pressure fluctuations over one rotation period at chosen observer locations for the hexa-rotor in forward flight with rotor phases optimized to reduce noise in the port side ground region.	62
A.1	Snapshot of the calculated free-wake of the quad-rotor configuration in level forward flight with optimized phase angles.	71
A.2	Snapshot of the calculated free-wake of the hexa-rotor configuration in level forward flight with optimized phase angles.	71
A.3	Disc contours representing loading and inflow on the rotors for the quad-rotor configuration in level forward flight, with phase angles optimized for noise reduction in the front ground region.	72
A.4	Disc contours representing loading and inflow on the rotors for the hexa-rotor configuration in level forward flight, with phase angles optimized for noise reduction in the front ground region.	73

List of Tables

3.1	Blade mesh parameters.	33
3.2	Variable pitch blade design parameters.	33
3.3	Design parameters of the vehicle configurations.	35
3.4	Microphone grids parameters.	36
4.1	Parameters of the NASA experimental case study.	40
4.2	UPM simulation parameters for the experimental case study.	40
4.3	NASA experimental test cases matrix.	42
4.4	Mean thrust values, comparison between NASA experimental values and numerical simulation results.	47
4.5	Radiated sound power level normalized with double the power radiated by single propeller, comparison between NASA experimental values and numerical simulation results.	50
5.1	Parameters for the flyover test case of the quad-rotor and hexa-rotor configurations.	53
5.2	Radiated sound power level [dB] on the hemispherical microphone grid, normalized with the power corresponding to the unsynchronised reference, for each of the optimization cases.	53
5.3	Calculated values of SPL [dB] and radiated sound power [W] on the hemispherical microphone grid in the flyover test case for the reference unsynchronized test and for the optimized case for each considered ground zone.	54

1 | Introduction

The widespread adoption of new aircraft technologies is heavily influenced by public acceptance, with perceived noise levels playing a central role in shaping the community opinion. This challenge is not new: in fact, the field of aeroacoustics emerged in the 1950s, pioneered by Lighthill,¹⁹ in response to the overwhelming noise generated by early jet aircraft. At the time, a deeper understanding of aerodynamic noise sources became essential to guide the development of better designs. Today, as the aviation industry undergoes another transformative phase with the rise of innovative rotary-wing aircraft, noise reduction remains a critical concern.

This thesis aims to contribute to this ongoing effort by focusing on rotorcraft noise, a topic of growing importance given the recent surge in interest surrounding advanced rotary-wing configurations, particularly electric vertical take-off and landing (eVTOL) vehicles. The research presented here is part of a broader study conducted at the Helicopter Department of the Institute of Aerodynamics and Flow Technology of the German Aerospace Center (DLR) in Braunschweig, in collaboration with Diego Donnini and Aldo Chella, which reported their results in the respective master thesis.^{33,34}

In this introductory chapter we first review the state of the art in electric vertical take off and landing vehicles (eVTOL), and then give a very basic introduction to rotorcraft noise sources. The main topic of the research is then presented as the rotor phase shifting technique, and the scope of the thesis is outlined.

1.1 Electric VTOL aircraft

In recent years the aerospace industry has shown great interest in the field of urban air transportation, commonly referred to as Urban Air Mobility. The ability of Vertical Takeoff and Landing (VTOL) aircraft to exploit low-altitude airspace in constrained environments has attracted the attention of stakeholders, institutions and companies.³⁹ But still to this day, it is not clear what type of aircraft configuration, between the many proposed, will be the best suited in terms of performance, efficiency, safety, and not least public acceptance.

A common denominator of many relevant designs is the use of rotary wings, or rotors, to provide both lift and propulsion. This comes at no surprise since a very simple application of fluid physics shows how the most efficient way to obtain hovering flight is to accelerate a large mass of air to a relatively small velocity. The use of distributed electric propulsion, which has benefits in terms of redundancy and efficiency of electric motors, has driven the design of new eVTOLs away from the conventional helicopter configuration. A review of recently proposed designs was given by Su,⁴⁰ Bacchini⁴² and Vieira.⁴¹ The main categories in which they fit are identified by the Vertical Flight Society⁴³ as:

- **multirotors:** rotary wing aircraft with four or more lifting rotors. They resemble traditional rotorcraft the most, sharing many of the same characteristics. The rotors are usually placed on top of the fuselage, interconnected by booms. The Volocopter Volocity, depicted in figure 1.1a, is a notable example employing 18 rotors. Co-axial counter-rotating rotors are often used, as in the



(a) Volocopter Velocity⁴⁴



(b) Jetson One⁴⁵

Figure 1.1: Current examples of multirotor eVTOL aircraft.

Jetson One single seater in figure 1.1b, due to enhanced propulsive efficiency and redundancy, although they are known to greatly increase noise. As for helicopters, flight velocity is controlled by the aircraft attitude: inclining the vehicle and thus the thrust balances the drag in forward flight. To control the attitude, moments are produced around the center of gravity by differential thrust, for example to produce a pitch down, or nose down moment the thrust of the back rotors is increased and the thrust of the front ones is decreased. To control rotor thrust there are two main strategies: either the rotor speed is varied or the blade pitch is adjusted collectively for all blades. Due to the increased rotational inertia of larger rotors, speed or *rpm* control becomes impractical for manned size vehicles, while it is very convenient for small unmanned ones for its simplicity of construction. Pitch control is a strategy taken directly from helicopters and has numerous advantages in the control of these new types of aircraft. Some designs already feature it as it is mentioned further down.

- **compound or lift+cruise:** integrates both multi-rotor and fixed-wing systems, allowing for vertical takeoff and landing like a multirotor drone while achieving efficient cruising like a fixed-wing aircraft. The flight begins with a vertical takeoff, where the multi-rotor system generates lift and controls attitude. Then the flight mode can be transitioned to fixed-wing as enough forward speed is gained. At this stage, aerodynamic control surfaces fully manage the aircraft, and the multi-rotor system is no longer needed, while horizontal thrust, or propulsion, is supplied by pushing or pulling propellers aligned horizontally. Notable examples are the City Airbus NextGen in figure 1.2 and the Autoflight Prosperity.
- **vectored thrust:** unlike the lift+cruise type, it uses the same propulsion system throughout the entire flight. The term vectored thrust refers to the ability to change the direction of propulsion. This can generally be achieved by tilting the rotor or tilting the wing, respectively referred to as tilt-rotor and tilt-wing. The Vertical Aerospace VX4 in figure 1.3a is an example of a tilt-rotor eVTOL with eight rotors and a fixed-wing configuration, with the front four rotors able to tilt from vertical to horizontal position when transitioning from hover to forward flight. In comparison, the Joby S4 in figure 1.3b features six tilt rotors, all of which can rotate vertically. Additionally, in both aircraft, variable propeller pitch allows the motors to operate efficiently across different flight conditions, and to control the hover attitude without varying rotor speed. A different example is the Lilium Jet, which employs 36 electric ducted fans embedded in the wing. Each of those fans has a very restricted disc area, allowing for a smaller wing with lower cruise drag and improved efficiency. The ducted design is also beneficial for noise shielding. However, the high disc loading strongly reduces hover efficiency and increases power consumption. The



Figure 1.2: Compound eVTOL from Airbus: CityAirbus NextGen.⁴⁶



(a) Vertical Aerospace VX4⁴⁷



(b) Joby Aviation s4⁴⁸

Figure 1.3: Current examples of vectored thrust eVTOL aircraft.

Airbus Vahana Alpha One is an example of a tilt-wing eVTOL with eight rotors. Unlike tilt-rotor designs, a tilt-wing aircraft rotates the entire wing to transition between vertical and forward flight. This configuration exposes the wing to high-speed airflow, allowing control surfaces to generate torque even at low speeds and delaying stall onset during transition. However, tilt-wing designs introduce aerodynamic complexities and increased sensitivity to wind during hover.

As previously discussed, a common thread among nearly all proposed configurations is the reliance on rotors and propellers. Given that this thesis focuses on the aeroacoustic noise generated by rotary wings, a brief, general introduction to rotorcraft noise generation is appropriate.

1.2 Rotorcraft noise

Helicopters are perceived as a very annoying source of noise by the general public.⁴¹ Despite the enormous progress which has been done from the 1950's till now in rotorcraft research to try and reduce their emitted noise, their sound signature is still between the most recognizable in the sky.

The noise we hear when an helicopter flies by is almost totally of aerodynamic nature, produced by the rotor blades interacting with the surrounding air. Other sources such as the engine are basically overwhelmed by the main and tail rotors. A rotor blade is, at the fundamental level, no different than an airplane wing in its fluid dynamic behavior, while showing a completely different acoustic

one. Why is that? The fundamental difference lies in the rapid rotation of the blade. In fact, if we were hypothetically able to sit on the rotating blade, we would not perceive any sound except for a light whooshing. What happens as the blade is rotating past our ears, is a periodic perturbation of the surrounding air: the blade displaces a volume of air just like a speaker membrane. Moreover, the force exerted on the blade by the flow, which enables the aircraft to fly, namely the lift, is also exerted back on the air and we perceive it in the form of a periodic pressure perturbation. Both of these phenomena arrive to us in the form of more or less pronounced pressure spikes, at a frequency which corresponds to the rotational frequency of the blade times the number of blades of the rotor: the *blade passing frequency*.

Acoustic sources of this type are referred to as *tonal noise*, since they are bound to a specific frequency and its harmonics, or integer multiples.

1.3 Noise reduction through rotor phase shifting

Several techniques have been employed to reduce rotor noise. The majority are passive, and span from optimization of the blade geometry to the modification of the anti-torque device for traditional helicopters (the fenestron and the NOTAR are notable examples).

An interesting active noise reduction technique has emerged in recent years, applicable to electric multirotor vehicles. This method exploits the rotors as coherent sound sources to create destructive interference of sound waves at selected observer positions. This technique, referred to as phase control or phase synchronization, involves adjusting the relative angular blade positions of multiple rotors rotating at equivalent speeds. By precisely controlling the phase angles, destructive interference can be used to reduce tonal noise in specific directions, thereby steering noise away from sensitive areas. The concept is visually explained in figure 1.4.

Schiller⁶ conducted an experimental campaign on fixed-pitch, hovering propellers, demonstrating that phase synchronization can achieve over 5 dB of reduction in sound power level at the blade passage frequency of a double rotor configuration. This study included both numerical and experimental analyses, confirming that relative phase control significantly affects the directivity and intensity of tonal noise. The research also showed that counterrotating and corotating rotor pairs exhibit different noise directivity patterns, with corotating pairs generally allowing for more uniform noise minimization. It provided the foundation for many other studies to follow, and is the main reference of this thesis.

Pascioni⁷ extended this research by modeling the sensitivity of phase control performance to various parameters, such as rotation rate, number of propellers, spacing, layout, and rotation direction. The considered application were tilt-wing aircraft with propellers parallel to the relative flow, not used for attitude control in advancing flight. Under optimal conditions, phase control was shown to reduce the average sound pressure level generated by the distributed propulsion vehicle on selected ground regions by up to 30 dB during a flyover event. However, practical limitations such as motor control errors and deviations in phase enforcement can quickly degrade this benefit. The study found that to achieve a 6 dB decrease at the blade passage frequency, standard deviation from the correct phase should not exceed 10° and deviation from the nominal rotation rate should not exceed approximately 0.5%.

Guan¹⁴ explored the feasibility of applying phase synchronization to quadrotors using numerical simulations. The study employed a multi-island genetic optimization algorithm to determine the optimal phase angles for noise minimization. Simulations indicated that for a quadrotor at an observation plane 5 meters below the vehicle, noise at a single point could be reduced by up to 30 dB, while a broader forward region experienced reductions of up to 12 dB. The results demonstrated that different rotor layouts, such as square and diamond configurations, influence the effectiveness of noise attenuation, with some configurations providing more uniform noise reduction than others.

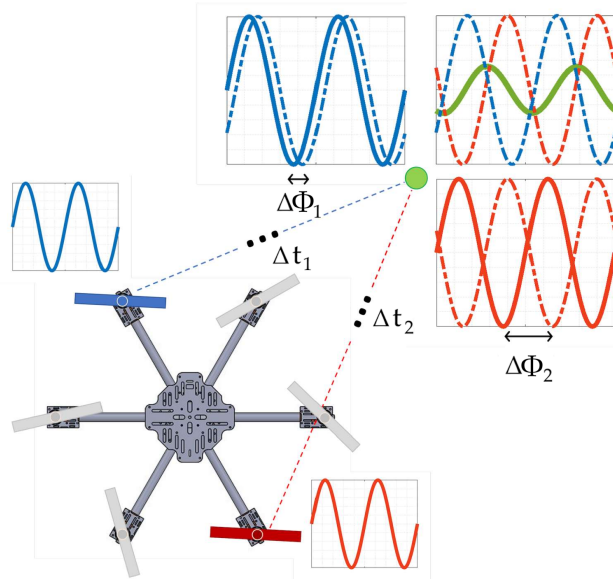


Figure 1.4: Phase shifting concept, from Valente.¹⁰ The contribution of each rotor to the pressure fluctuation arrives at the target at different time instants and therefore with different phases. The resultant phase shift of acoustic signals at the observer depends both on the relative rotor phases and on the difference in wave paths.

The works of Smith¹¹⁻¹³ provide a parametric analysis of the method applied to multirotors, considering the number of rotors and of blades, the rotational speed and the application to forward flight, but do not consider the attitude control and thus trim of the aircraft. In his findings he reported that the effect of forward flight is to diminish the capability of phase shifting at creating large zones of noise cancellation.

While phase control is conceptually similar to synchrophasing, a technique employed in fixed-wing propeller aircraft to reduce cabin noise,³⁷ it represents a novel approach in rotorcraft and electric vertical takeoff and landing (eVTOL) applications. Unlike traditional passive methods, phase synchronization does not require changes to rotor geometry or flight characteristics, making it an attractive solution for reducing urban noise pollution in emerging aerial mobility platforms.

1.4 Scope of the thesis

An important requirement of the phase shift technique is that rotors must share the same rotational frequency in order to produce coherent acoustic waves. This cannot be achieved with traditional control strategies which vary the rotational speed to regulate the thrust.

Thus the main idea behind this thesis work was to apply phase shifting to a multicopter configuration using *collective pitch control* to vary thrust and trim the aircraft, leaving free the speed control channel for phase synchronization. The study from Guan¹⁴ is the only one, to the author's current knowledge, which investigates rotor phase shifting applied to a quad-rotor configuration in forward flight, considering pitch variations necessary for attitude trim. However, the lifting line model used for the blades cannot capture the effect of pitch variation on the sectional pressure distribution and possibly on acoustics.

1. Introduction

The research work conducted for this thesis is aimed at evaluating the effectiveness of the phase shift method, applied to different configurations of collective pitch controlled multirotor aircraft, at steering noise emission in trimmed forward flight. The work was articulated as follows:

- a numerical toolchain was implemented for the evaluation of the acoustic signature of parametric multirotor configurations trimmed with variable pitch control, with phased rotors. The program operates a mid-fidelity, unsteady panel code with free-wake computation for the aerodynamic simulation of the rotors, and uses its output to compute linear sound propagation at the observer locations through a Ffowcs William-Hawkings based acoustic solver.
- the simulation toolchain was validated with experimental data of a synchronized double rotor configuration in hover available from NASA.⁶ The main focus was establishing if the influence of rotor phasing and rotor-to-rotor interactions on the magnitude and directionality of the noise signature was correctly captured by the simulations.
- an optimization of rotor phase angles was performed to obtain local minima of the sound pressure level at selected portion of the ground plane, for a quad-rotor and hexa-rotor configuration in trimmed forward flight. A surrogate based optimization algorithm³⁵ was applied to a fast noise prediction toolchain, developed appositely to speed up the computation by neglecting rotor-to-wake interactions and using the flow solution around an isolated rotor.

1.5 Thesis layout

Chapter 2 gives the theoretical background necessary for the understanding of the simulation software, as well as of the fundamental physics underlining aerodynamics and aeroacoustics of rotorcraft. Chapter 3 is dedicated to explaining the methodology behind the simulations computed in the course of this work, including the coupling between the different codes through the toolchain developed by the author. Chapter 4 reports a validation of the simulation procedure with experimental data, and discusses further the phase shift technique for noise control. Finally, chapter 5 presents the results of the optimization of phase angles in forward flight, aimed at steering noise projected on the ground plane by trimmed quad-rotor and an hexa-rotor configurations.

2 | Theoretical background

This chapter serves as a theoretical foundation to the work done in this thesis. The primary aim is to derive the mathematical formulations for the aerodynamic and acoustic problem employed by the simulation software, while giving a physical description of the involved phenomena and highlighting the necessary simplifying hypothesis. The first section deals with aeroacoustics, while in the second we outline the basics of vortex panel methods applied to rotorcraft aerodynamics.

2.1 Basics of Aeroacoustics

The science of acoustics is the study of all phenomena associated with propagation in a fluid or solid of small perturbations of pressure, density, velocity or displacement. Originally, it was limited to small pressure waves traveling through air which are detected by the human ear: sound. The study of propagation in water is dealt by underwater acoustics and in solids by ultrasonics and physical acoustics, including phenomena such as structural vibrations. We will limit ourselves to the original definition and specifically we will introduce the study of sound propagation through air from aerodynamic sources: aeroacoustics. In such a case, we are then basically dealing with an application of fluid dynamics.

The major problem when dealing with phenomena described by fluid dynamics is that the fundamental equations of motion are coupled, highly non-linear and sensible to the initial conditions. A general, analytic solution is not available and the approach needs to be numerical. In the field of computational fluid dynamics (CFD), the highest accuracy is obtained through direct numerical simulations (DNS), which solve the equations of motion directly without using a turbulence model. They are constrained to small Reynolds numbers due to the very small spatial and temporal scales of turbulence. Computational AeroAcoustics (CAA) is the equivalent of CFD for sound generation and propagation problems. To obtain the highest amount of fidelity, a CAA simulation would actually employ a DNS solution up to the finest scales of turbulence and solve for acoustic wave propagation directly. This brings even more complexity due to two main problems:

- i) range of scales: the simulation time-step has to be nearly 10 to 20 times smaller than the time period of the highest sound frequency. Audible frequencies go as high as $2 \cdot 10^4$ Hz, leading to a time step size of $\sim 10^{-6}$ s. Likewise, for accurately capturing the lowest frequency, at least 10 time periods worth of it need to be simulated. Thus, total simulation time can be more than 10^5 times greater than the time-step size. Similarly, the simulation needs to be carried out at a very fine spatial resolution over a large domain, since both generation and propagation of sound waves must be captured.
- ii) range of pressures: typically, pressure fluctuations in unsteady flows are in the order of 10^5 Pa. On the other hand, sound pressure goes as low as 10^{-5} Pa. The simulation therefore needs to keep track of pressures that can differ by a factor of 10^{10} , and its results become highly sensitive to truncation error. Even second order discretization schemes typically used for flow computations rapidly deteriorate the tiny sound pressure component in the overall pressure.

2. Theoretical background

A simplified modeling approach is to employ a first order approximation, namely a linearization, to describe the propagation of sound and treat the generation of it as a boundary condition problem. We will briefly derive the wave equation from the fundamental conservation laws, then focus on the main subject of this thesis: the sound generated by propellers and rotors. The basic theory behind it which is due to Ffowks, William and Hawkings and Farassat will then be outlined. Finally we present the numerical tool APSIM based on such theory which was employed in this work. But first we introduce the fundamental definitions used in acoustics. ^a

2.1.1 What is sound?

The human ear perceives sound due to the physical stimulation caused by a variation in time of air pressure, which is referred to as the *unsteady sound pressure*, or *acoustic pressure fluctuation*:

$$p'(t) = p(t) - \bar{p}, \quad \bar{p} = \lim_{T \rightarrow \infty} \frac{1}{T} \int_{-T/2}^{T/2} p(t) dt, \quad \overline{p'(t)} = 0 \quad (2.1)$$

in which \bar{p} is the steady part obtained by temporal averaging and is not perceived as sound.

This pressure fluctuation is measured at the *observer* location, meaning that it has propagated from a generic source as a wave moving at the speed of sound, in a sustained oscillation in space and time. It is important to distinguish it from other fluctuations in the pressure field which are not of acoustic nature and do not propagate as waves. For example, a microphone (which is nothing but a high frequency pressure transducer) placed inside of a turbulent flow (e.g. a wall tap measuring pressure in the boundary layer) which presents by definition velocity fluctuations, will measure a fluctuating pressure time signal. Such signal cannot be defined as acoustic per se, since it may not propagate in the field as a wave.

More over, an acoustic pressure (and density) local change is always coupled with a local motion of the medium. Actually, it is this local movement of fluid particles, described by the *acoustic particle velocity* \vec{u}' , which causes the pressure fluctuations. Since the particles oscillate in the direction of propagation, the resulting pressure and velocity waves propagates longitudinally at the speed of sound, not necessarily with the same phase.

An appropriate measure of the strength of acoustic signals is the *root mean square* or *rms* value of sound pressure:

$$p'_{rms} = \sqrt{p'^2} \quad (2.2)$$

The range of fluctuations detectable by our ears is extremely large, going from the order of 10^{-5} Pa (threshold of hearing) up to 10^2 Pa (threshold of pain). This is why we commonly employ a logarithmic scale when dealing with acoustic quantities. The most important variable introduced is the *sound pressure level* or *SPL*:

$$SPL = 10 \log \left(\frac{p_{rms}}{p_o} \right)^2 = 20 \log \left(\frac{p_{rms}}{p_o} \right) \quad (2.3)$$

in which p_o is the reference pressure, generally taken as the earing threshold $2 \cdot 10^{-5}$ Pa, and the pressure is squared to obtain a measure proportional to the energy of the wave.

^aThe theory reported in this section was taken from Delfs⁴ and Rienstra and Hirschberg.⁵

2. Theoretical background

2.1.2 Derivation of the linear wave equation

The dynamics of a compressible fluid are described by the famous Navier-Stokes equations:

$$\frac{d\rho}{dt} + \rho \nabla \cdot \vec{u} = \dot{m} \quad (2.4)$$

$$\rho \frac{d\vec{u}}{dt} = \vec{f} - \nabla p + \nabla \cdot \underline{\underline{\tau}} \quad (2.5)$$

$$\rho \frac{de}{dt} = -p \nabla \cdot \vec{u} + \underline{\underline{\tau}} : \nabla \vec{u} - \nabla \cdot \vec{q} + \zeta \quad (2.6)$$

which are obtained applying, in order, the conservation of mass, momentum and internal energy to a material volume of fluid and using the Reynolds theorem to derive the shown differential, or local, formulation. In those equations we find some virtual source terms which are employed to model physical phenomena which produce sound: \dot{m} is a virtual mass source (or sink), ζ is an internal heat source and \vec{f} is a generic bulk force.

Density variation in the fluid can be written as a function of pressure and entropy:

$$\delta\rho = \left(\frac{\partial\rho}{\partial p} \right)_s \cdot \delta p + \left(\frac{\partial\rho}{\partial s} \right)_p \cdot \delta s$$

given the speed of sound as $c^2 = \left(\frac{\partial p}{\partial\rho} \right)_s$ and defining $\sigma = -\frac{1}{\rho} \left(\frac{\partial\rho}{\partial s} \right)_p$, we get an equation for the pressure:

$$\frac{1}{c^2} \frac{dp}{dt} = \frac{d\rho}{dt} + \sigma\rho \frac{ds}{dt}$$

From the energy equation we can derive a relation for the entropy s and inserting it into the previous one we get the following expression for the pressure:

$$\frac{1}{c^2} \frac{dp}{dt} = -\rho \nabla \cdot \vec{u} + \frac{\sigma}{T} (\underline{\underline{\tau}} : \nabla \vec{u} - \nabla \cdot \vec{q} + \zeta) + \dot{m} \left(1 - \frac{\sigma p}{T\rho} \right) \quad (2.7)$$

which completes our set of governing equations for density, velocity and pressure for a generic compressible, viscous flow. If we exploit the constitutive equations for a perfect gas we can also substitute $c^2 = \gamma RT$ and $\sigma = 1/C_p$.

Lets further discuss the compressibility condition. Generally, relative density gradients occur in a flow when the acceleration, i.e. the material derivative of velocity, becomes high with respect to the square of the speed of sound. In the case of a steady flow around an aerodynamic body this occurs only if the free stream velocity is sufficiently high, but if the flow is unsteady the acceleration may be dominated by the time derivative of velocity and could then be high even for a fluid at rest. In that case we are typically dealing with sound.

Since our aim is to describe the acoustic pressure fluctuation p' which deviates from the ambient pressure $p^o := \bar{p}$, we can then apply the small perturbation theory to the governing equations and obtain the linear equations of gas dynamics. We just substitute the generic variable in the equations as $(\vec{\cdot}) = (\vec{\cdot})^o + \epsilon(\vec{\cdot})'$, let $\epsilon \rightarrow 0$ and neglect higher order terms:

$$\frac{d^o \rho'}{dt} + \rho^o \nabla \cdot \vec{u}' + \vec{u}' \cdot \nabla p^o + p' \nabla \cdot \vec{u}^o = \dot{m}' \quad (2.8)$$

$$\rho^o \frac{d^o \vec{u}'}{dt} + \nabla p' + \rho^o \vec{u}' \cdot \nabla \vec{u}^o + \rho' \vec{u}^o \cdot \nabla \vec{u}^o = \vec{f}' \quad (2.9)$$

$$\frac{1}{(c^2)^o} \left(\frac{d^o p'}{dt} + \vec{u}' \cdot \nabla p^o \right) + p^o \nabla \cdot \vec{u}' + \left(\frac{\rho^o p'}{p^o} \right) \nabla \cdot \vec{u}^o = \frac{\gamma - 1}{\gamma} \frac{\rho^o}{p^o} \zeta' + \frac{1}{\gamma} \dot{m}' := \theta' \quad (2.10)$$

2. Theoretical background

in which $d^\circ/dt := \partial/\partial t + \vec{u}^\circ \nabla$ is the lagrangian (material) derivative taken along the mean flow, and θ' incorporates unsteady mass and heat sources. The perturbations from viscous stresses, viscous dissipation and heat flux were neglected since they are generally small.

If we make the assumption of still sources inside a stagnant homogeneous media, we can simplify further the perturbation equations as:

$$\frac{\partial \rho'}{\partial t} + \vec{u}' \nabla \rho^\circ + \rho^\circ \nabla \cdot \vec{u}' = \dot{m}' \quad (2.11)$$

$$\rho^\circ \frac{\partial \vec{u}'}{\partial t} + \nabla p' = \vec{f}' \quad (2.12)$$

$$\frac{1}{(c^2)^\circ} \frac{\partial p'}{\partial t} + p^\circ \nabla \cdot \vec{u} = \dot{\theta}' \quad (2.13)$$

Now we can derive the linear wave equation for the pressure fluctuation through the following manipulation: $\frac{\partial}{\partial t}(2.13) - \rho^\circ \nabla \cdot (2.12 \cdot \frac{1}{\rho^\circ})$ and obtain:

$$\frac{1}{c_\infty^2} \frac{\partial^2 p'}{\partial t^2} - \nabla^2 p' = \frac{1}{\gamma} \frac{\partial \dot{m}'}{\partial t} + \frac{\gamma - 1}{c_\infty^2} \frac{\partial \dot{\zeta}'}{\partial t} - \nabla \cdot \vec{f}' = \frac{\partial \dot{\theta}'}{\partial t} - \nabla \cdot \vec{f}' := Q_p \quad (2.14)$$

in which we made the assumption of a constant mean density medium, and Q_p represents the sources term. We recognize the equation as an hyperbolic, second order partial differential equation: the wave equation.

2.1.3 Solutions to the wave equation and the multipole approximation

The spherically symmetric solution to the homogeneous (no sources) wave equation in three-dimensional space is due to d'Alambert:

$$p'(r, t) = \frac{1}{r} f(t - r/c_\infty) \quad (2.15)$$

which describes the free-field (i.e. not considering obstacles) propagation of a pressure wave originated by a still point source radiating sound isotropically, or as we will define it later on, a monopole source. The term r is the radial distance from the source and f is a generic function of time and distance. To find the solution to the field in presence of a generic source term, we can modify equation 2.15 exploiting the superposition principle. First we rewrite it for a source located at a point $\vec{\xi}$ and define the distance as $r := \|\vec{x} - \vec{\xi}\|$, we also introduce the retarded, or emission, time $\tau = t - r/c_\infty$.^b Then we define a source domain made by a continuous distribution of point sources, and the resulting solution is obtained superposing the single ones, which results in an integration:

$$p'(\vec{x}, t) = \int_{V_s} \frac{1}{r} f(\tau(t, r), \vec{\xi}) dV(\vec{\xi}) \quad (2.16)$$

in which V_s is the domain defined by the source locations $\vec{\xi}$. When inserting this solution in the non-homogeneous wave equation, through some manipulation, we obtain:

$$p'(\vec{x}, t) = \frac{1}{4\pi} \int_{V_s} \frac{Q_p(\tau(t, r), \vec{\xi})}{r} dV(\vec{\xi}) \quad (2.17)$$

and if we substitute the expression for the source term, taking note that it must be evaluated at the emission time τ :

$$p'(\vec{x}, t) = \frac{1}{4\pi} \left[\int_{V_s} \frac{1}{r} \frac{\partial}{\partial \tau} \left(\left(1 - \frac{\sigma_\infty p_\infty}{\rho_\infty T_\infty} \right) \dot{m}' + \frac{\sigma_\infty}{T_\infty} \dot{\zeta}' + \frac{f'_r}{a_\infty} \right)_\tau dV(\vec{\xi}) + \int_{V_s} \frac{[f'_r]_\tau}{r^2} dV(\vec{\xi}) \right] \quad (2.18)$$

^bWe indicate with the subscript ∞ variables referred to the undisturbed flow, thus constant.

2. Theoretical background

in which the subscript $\tau = t - r/c_\infty$ marks terms evaluated at the retarded (or emission) time, $\vec{\xi}$ and \vec{x} are the source's and observer's coordinates vectors, $r = \|\vec{x} - \vec{\xi}\|$ is the distance between source and observer. This equation describes the free field propagation of sound waves produced by a continuous, bounded distribution of point sources.

Let us now introduce the Green's function G as another way to express the solution to the wave equation. Consider a particular source expressed as a δ Dirac function in space and time:

$$\frac{1}{c_\infty^2} \frac{\partial^2 G}{\partial t^2} - \nabla_x^2 G = \delta(\vec{x} - \vec{\xi}) \delta(t - \tau) \quad (2.19)$$

The equation describes the pressure field p' , which we represent here with G , due to a unit point source at $\vec{x} = \vec{\xi}$ firing a needle pulse at $t = \tau$. The Green's function G then basically represents the impulsive response of the wave field. We can then easily verify that the solution relative to any source distribution Q_p is given by the convolution between G and Q_p :

$$p'(\vec{x}, t) = \int_{V_\infty} \int_{-\infty}^t G(\vec{x}, t, \vec{\xi}, \tau) Q_p(\vec{\xi}, \tau) d\tau dV(\vec{\xi}) \quad (2.20)$$

In our case, since we already solved the wave equation under free field conditions (2.17), we can determine the free field Green's function G_o as:

$$G_o(\vec{x}, t, \vec{\xi}, \tau) = G_o(r, \tau - t) = \frac{\delta(\tau - t + \|\vec{x} - \vec{\xi}\|/c_\infty)}{4\pi\|\vec{x} - \vec{\xi}\|} = \frac{\delta(\tau - t + r/c_\infty)}{4\pi r} \quad (2.21)$$

We will limit our discussion to the free-field case.

We now come to the definition of a fundamental mathematical tool in acoustic modeling: the multipole expansion. ^c It is an approximation of the Green's function G_o through a spatial Taylor expansion around the central point $\vec{\xi}_o$ inside the source domain $V_s(\vec{\xi})$:

$$G_o(\vec{x}, t, \vec{\xi}, \tau) = G_o(\vec{x}, t, \vec{\xi}_o, \tau) + (\nabla_{\vec{\xi}} G)_o(\vec{\xi} - \vec{\xi}_o) + \frac{1}{2!} (\vec{\xi} - \vec{\xi}_o)^t \mathcal{H}_{\vec{\xi}}(G)_o(\vec{\xi} - \vec{\xi}_o) + o(\|\vec{\xi} - \vec{\xi}_o\|^2) \quad (2.22)$$

in which $\mathcal{H}_{\vec{\xi}}$ is the Hessian matrix in the source centered spatial coordinates.

The solution for a generic source Q_p then is given as seen by the convolution $G_o \circledast Q_p$, and by adopting index notation and explicitating the dependence of G_o on $\vec{\xi}$ and \vec{x} we get the resulting pressure field:

$$p'(\vec{x}, t) = \sum_{i=0}^{\infty} \sum_{j=0}^{\infty} \sum_{k=0}^{\infty} (-1)^{i+j+k} \frac{\partial^{i+j+k}}{\partial x_1^i \partial x_2^j \partial x_3^k} \left(\frac{m_{ijk}(\tau_o)}{4\pi r_o} \right) \quad (2.23)$$

$$m_{ijk}(\tau_o) = \int_{V_s} \frac{1}{i!j!k!} (\xi_1 - \xi_1^o)^i (\xi_2 - \xi_2^o)^j (\xi_3 - \xi_3^o)^k Q_p(\vec{\xi}, \tau_o) dV(\vec{\xi})$$

in which τ_o is the retarded time w.r.t. the fixed reference point $\vec{\xi}_o$, and the abbreviation m_{ijk} is the multipole moment of order 2^{ijk} of the source Q_p . The single m_{000} term of order zero in the (triple) summation is the monopole moment, the terms with order one m_{100}, m_{010} and m_{001} are the dipole moments. Terms of order two ($i + j + k = 2$) form the quadrupole moment and so on.

We can rewrite the moments explicitating their dependence on direction by applying the chain rule:

$$\frac{\partial^{i+j+k}}{\partial x_1^i \partial x_2^j \partial x_3^k} (m_{ijk}(\tau_o)) = \left(\frac{\partial r_o}{\partial x_1} \right)^i \left(\frac{\partial r_o}{\partial x_2} \right)^j \left(\frac{\partial r_o}{\partial x_3} \right)^k \cdot \frac{\partial m_{ijk}(\tau_o)}{\partial t^{ijk}} = \cos^i \theta_1 \cos^j \theta_2 \cos^k \theta_3 \cdot \frac{\partial m_{ijk}(\tau_o)}{\partial t^{ijk}} \quad (2.24)$$

^cThe multi-pole expansion is not applied only in acoustics, on the contrary it was employed much time before in electromagnetism and afterwards in aerodynamics too: sources and doublets of potential flow are nothing but monopoles and dipoles.

2. Theoretical background

in which the partial derivatives of r_o w.r.t. the observer location \vec{x} are the directional cosines of position \vec{x} w.r.t. source position $\vec{\xi}$. Thus the dipole and higher order moments exhibit a non-isotropic spatial pattern made by radiation lobes.

We can now explicitate the source term Q_p in order to understand how it could be approximated by the multipole expansion, as defined in equation 2.14. Let us call $\partial\theta'/\partial t := Q_{m,v}$ the component of sound sources due to unsteady mass injection and heat source, and $\nabla \cdot \vec{f}' := Q_f$ the part due to unsteady forces. Then we can calculate the corresponding moments. The monopole moment of $Q_{m,v}$ is:

$$m_{000}[Q_{m,v}] = \int_{V_s} Q_{m,v} dV(\vec{\xi}) = \frac{\partial}{\partial t} \int_{V_s} \theta' dV(\vec{\xi}) \quad (2.25)$$

which is the rate of change in time of the mass and heat sources over the source volume. Instead, the monopole moment of Q_f is zero:

$$m_{000}[Q_f] = \int_{V_s} Q_f dV(\vec{\xi}) = - \int_{V_s} \nabla_{\vec{\xi}} \cdot \vec{f}' dV(\vec{\xi}) = - \int_{\partial V_s} \vec{f}' \cdot \vec{n} dS = 0 \quad (2.26)$$

since $\vec{f}' = \vec{0}$ outside of V_s and thus its net flux through its boundary ∂V_s must be zero. Thus the total monopole contribution is only given by mass and heat sources.

The first term of the dipole moment of $Q_{m,v}$ is:

$$m_{100}[Q_{m,v}] = \frac{\partial}{\partial t} \int_{V_s} (\xi_1 - \xi_1^o) \theta' dV(\vec{\xi}) \quad (2.27)$$

and the dipole moment of the force term is given by the total force exerted by the source volume on the fluid, the first moment m_{100} is the first component, m_{010} the second and m_{001} the third:

$$m_{100}[Q_f] = \int_{V_s} f'_1 dV(\vec{\xi}) \quad (2.28)$$

and the total dipole contribution to the pressure fluctuation:

$$p'_d = p'_{100} + p'_{010} + p'_{001} = \nabla_x \cdot \left[-\frac{1}{4\pi r_o} \left(\frac{\partial}{\partial t} \int_{V_s} (\vec{\xi} - \vec{\xi}_o) \cdot \theta'(\vec{\xi}, \tau_o) dV(\vec{\xi}) + \int_{V_s} \vec{f}'(\vec{\xi}, \tau_o) dV(\vec{\xi}) \right) \right] \quad (2.29)$$

The mass / heat source contribution is only given by its spatial variation across the source volume, whether the force contribution is given by the bulk force vector. Thus one can generally represent the mass / heat source as an acoustic monopole and the force as a dipole. The approximation converges to the actual contribution faster the smaller the source domain is, since higher order terms are dependant on $(\vec{\xi} - \vec{\xi}_o)$.

The final result which is fundamental in acoustic numerical simulations regards the point source abstraction. Since higher order terms in the multipole expansion get smaller with the source domain size, we ask ourself what would happen if the sources were infinitesimally small located at the center $\vec{\xi}_o$:

$$\begin{aligned} \dot{m}'(\vec{x}, t) &= \dot{m}'_p(t) \delta(\vec{x} - \vec{\xi}_o) \\ \zeta'(\vec{x}, t) &= \zeta'_p(t) \delta(\vec{x} - \vec{\xi}_o) \\ \vec{f}'(\vec{x}, t) &= \vec{f}'_p(t) \delta(\vec{x} - \vec{\xi}_o) \end{aligned} \quad (2.30)$$

in which subscript p stands for point. Inserting them in the multipole expansion:

$$p'(\vec{x}, t) = \frac{1}{4\pi} \left[\frac{1}{r_o} \left(\frac{\partial \theta'_p}{\partial t} \right)_{\tau_o} - \nabla_x \cdot \left(\frac{\vec{f}'_p}{r_o} \right)_{\tau_o} \right] \quad (2.31)$$

we see how all higher order terms vanish, such that mass/heat point sources represent pure monopoles and point forces represent pure dipoles.

2.1.4 Acoustic sources of propellers and rotors

Until now we only dealt with still sources in a quiescent medium. Rotary wings on the other hand radiate sound while in motion and the resulting noise signature is profoundly shaped by this core characteristic. This section will serve as a little introduction to the specific application, hoping to give an intuitive understanding of the relevant phenomena before the formal derivation of the necessary equations.^d

A propeller can be generally described as an open, rotating, bladed device aimed at producing thrust. Rotors respond to a very similar definition but are typically associated with helicopters and operate in a fundamentally different condition: while a propeller sees a flow which is always axisymmetric, since its direction of travel is parallel to its rotational axis, an helicopter rotor sees a tangent component of the relative wind when in forward flight. Thus the difference in nomenclature stands mainly in the operating conditions, which are very important in many aspects, not least noise generation. We will not be strict about the nomenclature since we will always be treating helicopter-like applications in which rotors serve both functions of lift and propulsion in flight.

The major propeller noise components are:

- thickness noise, caused by the displacement of air by the blade passage, it is modeled as a moving mass source/sink
- steady-loading noise, due to the steady (constant in time) component of the blades lifting force, it is modeled as a moving force source
- unsteady-loading noise, caused by variation of the lift force in time, mainly due to non-symmetrical flow in forward flight and blade-vortex interaction
- impulsive noise, due to sonic conditions on the advancing blade
- broadband noise, differently from the previous tonal sources it presents a flat spectrum across frequencies and is related to viscous effects, mainly turbulence generation and interaction

The tonal, or harmonic, component of propeller noise is recognizable as a periodic signal, which pulses at a constant period. The frequency of this noise is given by the blade passing frequency (BPF) equal to the number of blades times the rotational speed of the rotor in revolutions per second. Since this sound is the result of many types of sources, as listed above, the resultant signal is not a pure sinusoid and many harmonics exist.

Broadband noise contains contribution across all frequencies and is typically of smaller importance. Its prediction requires either the solution of viscous flow at least in the vicinity of the blade or the use of simplified models. We did not consider it in the current work since the phase shift technique is supposed to only affect the tonal components.

Steady sources are those which would appear constant in time to an observer on the rotating blade. They produce periodic noise only because of their rotation.^e The transverse periodic displacement of air by the passing blade element is the cause of thickness noise. The amplitude is proportional to the blade volume and the shape of the wave form (and thus frequency characteristics) are dependent on the geometry of the airfoil. It is represented as a monopole source distribution and is the dominant source in hovering flight. Loading noise originates from the pressure field that surrounds the blade generating a resultant force, which moving in the medium creates a pressure fluctuation.

Unsteady sources are time-dependant in the rotating blade reference system. They include both the periodic and the random variations of blade loading. The main contribution to the periodic part is

^dThe theory was taken from NASA.³⁶

^eThis is easy to comprehend: sitting on the wing of an airplane we would not hear anything except for a constant whooshing sound caused by turbulence in the boundary layer and steady vortex generation.

2. Theoretical background

dissimetry of lift in forward flight, caused by a variation in dynamic pressure at a frequency of once per revolution, for each blade. The resulting noise directivity is no more constant around the azimuth but instead presents lobes, peaks and valleys. Unsteady loading events are also caused by interaction with the wake shed by a preceding rotor, the ingestion of atmospheric turbulence or blade vortex interaction. Those typically produce contributions to higher frequencies.

Limiting the discussion to inviscid flows at low tip Mach numbers, we only have to deal with thickness, or monopole, noise and loading, or dipole, noise. We analyze their qualitative characteristics for hover and forward flight.

Hovering harmonic noise

In general, a simple pressure pulse is produced for each blade during one revolution, and the parts of the rotor disk having the highest Mach number in the direction of the observer are the dominant ones.

Thickness noise is the predominant contribution to the pressure time history, especially in-plane. The shape of its pressure pulse is symmetrical, with two small positive peaks separated by a large negative one. Its origin can be explained in simple terms as follows: the leading edge of the blade with increasing thickness causes a positive air mass displacement, while the trailing edge causes a negative one, those effects are Doppler-amplificated (the concept is explained in the next sections) when the observer line of sight is perpendicular to the blade producing two large opposing flux peaks, which occur at slightly different times due to finite chord length. The time derivative of this mass flux is the cause of the pressure fluctuation of said shape.

The steady force noise causes instead an asymmetric pressure pulse and does not radiate in the rotor plane. It is the main source out of plane, while still being quieter in hovering than the in-plane thickness noise. The origin of this steady loading noise can be explained like this: imagine a fixed point in space located on the rotor plane. When a blade, represented by a single lift force vector, passes by this point the pressure experiences a temporary perturbation. While the force is steady in the rotating frame, its derivative is non zero in the inertial frame, and it creates a sound source.

Forward flight harmonic noise

The aerodynamics of a rotor in forward flight are complex, especially considering blade flapping and cyclic pitch inputs. In our case application of rigid blades with only collective control, the behavior simplifies but still exhibits all of the complexities with respect to the flow field. Putting it in simple terms, the main factor at play when a rotor transitions into non-axial flight is the periodic variation of relative flow experienced by the blade as it goes around the azimuth: on the advancing side the flight speed adds to the blade rotational speed, and the opposite happens on retreating side. This is the cause of long known problems such as drag divergence, retreating stall and dissimetry of lift. The net effect is a periodic variation of rotor air loads rich in low-frequency harmonics of the BPF.

2.1.5 Ffowcs William-Hawkings equation and the Farassat formulation

The Ffowcs Williams-Hawkings (FW-H)²⁰ equation is basically a generalization of Lighthill's acoustic analogy¹⁹ for bodies in motion. ^f The idea is to enclose those bodies with a control surface and derive the whole wave field outside of it assuming variables on the surface are known. We proceed through a manipulation of the Navier-Stokes equations without any actual simplification. Similarly to the Kirchoff integral formulation, we introduce the Heaviside function $H(f)$, in which $f = 0$ is the parameterization of our control surface ($H(f) = 0$ if $f < 0$, i.e. inside of the surface). Then we multiply the mass balance 2.4 (with $\dot{m} = 0$) and the momentum balance 2.5 by $H(f)$, replacing

^fTheory for this section was taken from the works of Farassat from 1975¹⁷ and 2007¹⁸

2. Theoretical background

$p' = p - p_\infty$. Taking the time derivative of the former and subtracting the divergence of the latter, we obtain:

$$\frac{1}{c_\infty^2} \frac{\partial^2}{\partial t^2} (H(f)p') - \nabla^2 (H(f)p') = \frac{\partial}{\partial t} (\rho_\infty v_n \delta(f)) - \nabla \cdot (p \vec{n} \delta(f)) \quad (2.32)$$

in which v_n is the local normal velocity of the surface, p is the gauge pressure ($p - p_\infty$) on the surface, \vec{n} is the unit normal to the surface and δ is the Dirac function. The Heaviside function here simply means that pressure fluctuations are evaluated only outside of the control surface. This is the FW-H equation for a solid surface, i.e. considering $f = 0$ as the solid boundary of the body in motion, neglecting the so called *quadrupole* noise term due to turbulence. We have essentially converted a problem of noise generation by a moving surface to a linear sound propagation problem applying what is known as the *acoustic analogy*. The first term on the r.h.s. is referred to as thickness noise, the second is loading noise. They are described by monopole and dipole sources, respectively. One must be careful when using this nomenclature, noting that sources in motion have a distinct character from the corresponding still sources. For example: a still monopole radiates noise isotropically, with no preferential direction, a rotating monopole instead radiates mainly in the plane of rotation!

Solution of the wave equation with moving sources

Equation 2.32, while it has identified the expression for noise sources of moving surfaces (rotating blades in our case), did not actually bring us any closer to solving the pressure wave field caused by such sources. We have now to solve the wave equation for the two source terms on the r.h.s. by referring to the acoustic linear theory developed previously in this chapter.

Let us consider a point source placed on a moving surface in a quiescent medium. We have to solve the pressure wave equation 2.14 considering the changing location of source terms. With Q being the generic acoustic source, we have:

$$\frac{1}{c_\infty^2} \frac{\partial^2 p'}{\partial t^2} - \nabla^2 p' = Q(\vec{x}, t) \delta(f(\vec{\xi}, \tau)) \quad (2.33)$$

in which we used the δ Dirac function to define a point source on the parametric surface $f(\vec{\xi}, \tau)$. We can find the solution using the known free-field Green's function 2.21 by applying the convolution:

$$p'(\vec{x}, t) = \int_{-\infty}^t \int_{V_\infty} Q(\vec{\xi}, \tau) \delta(f(\vec{\xi}, \tau)) \frac{\delta(\tau - t + |\vec{x} - \vec{\xi}|/c_\infty)}{4\pi|\vec{x} - \vec{\xi}|} dV(\vec{\xi}) d\tau \quad (2.34)$$

We will call the argument of the δ function as $g := \tau - t + r/c_\infty$. The equation $g = 0$ actually represents a surface: we can imagine to fix the observer space-time variables, then we can write it as $|\vec{x} - \vec{\xi}| = c_\infty(t - \tau)$. In the source space-time variables it describes a sphere with center \vec{x} and radius $c_\infty(t - \tau)$, and as the source time τ reaches the observer time t the sphere shrinks to zero, with a rate of contraction equal to sound speed. When that happens, the integral value becomes different from zero by the properties of $\delta(g)$: sound pressure is produced. Thus g represents the causality condition in acoustics and ensures that sound reaches the observer only when it has traveled the necessary radial distance.

The $\vec{\xi}$ and \vec{x} frames are fixed to the undisturbed, quiescent medium. It is convenient to introduce a new frame $\vec{\eta}$ fixed to the moving surface. Each point on the moving surface is described by its position $\vec{\eta}$ which we call the Lagrangian variable, since it is then linked to the inertial reference frame through its trajectory: $\vec{\xi} = \vec{\xi}(\vec{\eta}, \tau)$. Thus applying the transformation $\vec{\xi} \rightarrow \vec{\eta}$, noting that they are isometric

2. Theoretical background

thus with unit Jacobian, the equation becomes:

$$\begin{aligned} p'(\vec{x}, t) &= \int_{-\infty}^t \int_{V_\infty} Q(\vec{\xi}(\vec{\eta}, \tau), \tau) \delta(f(\vec{\xi}(\vec{\eta}, \tau), \tau)) \frac{\delta(g)}{4\pi r} dV(\vec{\eta}) d\tau = \\ &= \int_{-\infty}^t \int_{V_\infty} \tilde{Q}(\vec{\eta}, \tau) \delta(\tilde{f}(\vec{\eta}, \tau)) \frac{\delta(g)}{4\pi r} dV(\vec{\eta}) d\tau \end{aligned} \quad (2.35)$$

with $(\tilde{\cdot})$ denoting functions written in the moving reference frame. Next we use the transformation $\tau \rightarrow g$, of which we first have to calculate the Jacobian $\partial g / \partial \tau$:

$$g = \tau - t + \frac{|\vec{x} - \vec{\xi}(\vec{\eta}, \tau)|}{c_\infty} \quad (2.36)$$

$$\frac{\partial g}{\partial \tau} = 1 + \frac{1}{c_\infty} \frac{\partial r}{\partial \xi_i} \frac{\partial \xi_i}{\partial \tau} = 1 - \frac{\vec{e}_r v_i}{c_\infty} = 1 - M_r \quad (2.37)$$

in which $M_r = \vec{e}_r v_i / c_\infty$ is the Mach number of point $\vec{\eta}$ in the radiation direction (towards the observer) at time τ , \vec{e}_r is the i^{th} component of the unit radiation versor, v_i is the i^{th} component of the velocity of point $\vec{\eta}$ in the $\vec{\xi}$ frame. Note that we applied the index notation for summation. The equation becomes:

$$\begin{aligned} p'(\vec{x}, t) &= \int_{-\epsilon}^{+\epsilon} \int_{V_\infty} \tilde{Q}(\vec{\eta}, \tau) \delta(\tilde{f}(\vec{\eta}, \tau)) \frac{\delta(g)}{4\pi r |1 - M_r|} dV(\vec{\eta}) dg \\ &= \int_{V_\infty} \left[\frac{\tilde{Q}(\vec{\eta}, \tau)}{4\pi r |1 - M_r|} \delta(\tilde{f}) \right]_{g=0} dV(\vec{\eta}) \end{aligned} \quad (2.38)$$

with ϵ being a positive small number.

The expression $|1 - M_r|$ is known as the Doppler factor: it is responsible for a convective amplification of the pressure signal, which is strengthened when the velocity points towards the observer (thus $M_r > 0$) and is weakened in the opposite direction. We must not confuse this effect with the more famous Doppler effect which is related to the frequency shift, and is of course present, according to a convection factor $d\tau/dt = \frac{1}{|1 - M_r|}$, which causes the shift to higher frequencies when the source is moving towards the observer.

In the subsonic regime $1 - M_r > 0$, such that we can drop the absolute value. The condition $g = 0$ makes the source, or retarded time τ dependent on the other variables $(\vec{x}, t, \vec{\eta})$:

$$g = \tau - t + \frac{|\vec{x} - \vec{\xi}(\vec{\eta}, \tau)|}{c_\infty} = 0 \quad (2.39)$$

The equation, which is to be solved numerically for a generic surface trajectory, gives the emission time τ_e , corresponding to a certain emission position $\vec{\xi}(\vec{\eta}, \tau_e)$ and observer position \vec{x} .

We can use this notation in the equation:

$$p'(\vec{x}, t) = \int_{V_\infty} \frac{\tilde{Q}(\vec{\eta}, \tau_e)}{4\pi r_e (1 - M_{r_e})} \delta(\tilde{f}(\vec{\eta})) dV(\vec{\eta}) \quad (2.40)$$

where $M_{r_e} = \vec{M}(\vec{\eta}, \tau_e) \cdot \vec{e}_{r_e}$ and $\vec{M}(\vec{\eta}, \tau_e) = \vec{v}(\vec{\eta}, \tau_e) / c_\infty$.

We can now pass from an integral on the entire domain volume to a surface integral by exploiting the properties of the δ function:

$$p'(\vec{x}, t) = \int_{\tilde{f}=0} \frac{\tilde{Q}(\vec{\eta}, \tau_e)}{4\pi r_e (1 - M_{r_e})} dS := \int_{\tilde{f}=0} \left[\frac{Q(\vec{\xi}, \tau)}{4\pi r (1 - M_r)} \right]_{\tau_e} dS \quad (2.41)$$

in which we also defined a short-hand notation for the integration with subscript τ_e , which does not simply mean to use retarded time in the equation (as is done usually for still sources) but means that the whole integrand needs to be evaluated at the emission time, in the emission source location at the emission distance, with functions written in the local Lagrangian reference system.

2. Theoretical background

Derivation of the Farassat formulation

The following solution for thickness and loading noise terms in the FW-H equation was given by Farassat, and is thus commonly named Farassat 1 or Farassat 1A. Basing on our previous results in solving equation 2.33, which resulted in 2.41, finding the solution for the thickness noise in equation 2.32 is straightforward:

$$p'_T(\vec{x}, t) = \frac{\partial}{\partial t} \int_{f=0} \left[\frac{\rho_0 v_n}{4\pi r(1 - M_r)} \right]_{\tau_e} dS \quad (2.42)$$

The derivation of the loading noise solution requires some intermediate passages, due to the presence of the divergence operator. The procedure is analogous to the one done for the generic source Q , involving the use of the Green's function to solve for the wave equation with loading noise sources. We exploit the following identity:

$$\frac{\partial}{\partial x_i} \left(\frac{\delta(g)}{r} \right) = -1/c_\infty \frac{\partial}{\partial t} \left(\frac{e_{r_i} \delta(g)}{r} \right) - \frac{e_{r_i} \delta(g)}{r^2} \quad (2.43)$$

which lets us turn the divergence into a time derivative, and now we can apply result 2.41 to obtain the loading noise solution:

$$p'_L(\vec{x}, t) = \frac{1}{c_\infty} \frac{\partial}{\partial t} \int_{f=0} \left[\frac{p \cos \theta}{4\pi r(1 - M_r)} \right]_{\tau_e} dS + \int_{f=0} \left[\frac{p \cos \theta}{4\pi r^2(1 - M_r)} \right]_{\tau_e} dS \quad (2.44)$$

in which $\cos \theta = \vec{n} \cdot \vec{e}_r$, i.e. angle of the normal to the surface relative to the observer line of sight, at the emission time.

The sum of loading and thickness noise forms Farassat formulation 1. Further mathematical manipulation of the equations results into evaluating analitically the observer time derivative (instead of performing it numerically) and gives formulation 1A, which is superior in terms of computational time.

2.1.6 APSIM: Aeroacoustic Prediction System based on an Integral Method

The Aeroacoustic Prediction System based on an Integral Method, APSIM, has been developed at the DLR Institute of Aerodynamics and Flow Technology for the prediction of rotor or propeller noise radiated in the free far-field. The methodology of APSIM is based on the FW-H formulation and only linear sound propagation is taken into account, as explained in detail in the previous sections.

The program is designed to calculate wave propagation over large distances in uniform flows, taking as input the flow solution in the vicinity of the rotor blades or directly on them. In addition to the formulation of the FW-H equation for solid surfaces, that we presented earlier and is the one employed in the course of the present work, the program can also apply a permeable surface formulation in which quadrupole noise due to turbulence and non-linear sources is also taken into account. The latter formulation requires a detailed solution to the viscous flow inside of a volume enclosing the rotor blades, generally obtained with a compressible Navier-Stokes flow solver.

In the solid surface formulation, only the blade geometry together with the surface pressure distribution for each time-step are required. Acoustic pressure fluctuations at specified grid (observer) points are calculated through Farassat formulas for thickness 2.42 and loading noise 2.44.⁸ Thickness noise is only given by the geometry and kinematics of the blades, while loading noise is determined by the aerodynamic loads acting on them, namely the lift.

The code was extensively validated by comparing results with lab²¹ and field²³ experimental data, as well as with analytical formulations.²⁴

⁸To be precise, formulation 1A is implemented due to the enhanced precision and reduced computational time.

2.2 Introduction to potential flow solvers

To perform the acoustic simulation through the derived theory, the pressure distribution on the moving blade surface is a required input. In principle, the complete governing equations would need to be solved in order to obtain the value of the wall pressure. The procedure is numerical and it always involves some degree of simplifying assumptions, the level depending on the required accuracy.

The first applications of numerical fluid dynamics were limited to incompressible, irrotational and steady flows through the solution of the Laplace equation of velocity potential. This was in the early age of computers when more complex implementations were impractical due to the limited resources, and potential solvers, usually coupled with an approximated solution to the steady boundary layer equations, were the industry standard. Simulations of fixed wing aircraft then progressively moved towards mesh-based Navier-Stokes solving techniques, which offer higher solution accuracy at the expense of more computational effort.

Flow simulations of rotary wings pose a different degree of difficulty. The inherent unsteadiness and complexity of the flow involved make detailed computations, such as URANS (Unsteady-Reynolds Averaged Navier-Stokes), highly time and resource expensive even for today's technology, due to the required fine discretization in space and time. In this field, mid-fidelity potential flow based methods are still largely employed especially for studies in the early stage of development. Aeroacoustic computations commonly involve the use of such methods as an input, since they are capable of capturing many of the important features which influence sound generation in rotors (steady and unsteady loading, blade-vortex interaction, blade geometry) while requiring a lowered computational cost. Studies involving multi-rotor configurations, such as the present work, represent a perfect application for such methods.

We now give an overview on the theory, assumptions and limitations of panel methods, moving then to free-wake vortex methods applied to rotorcraft. It is important to mention that while the general background theory for potential solvers is common to all codes, the actual implementation can vary substantially. Here we keep the description consistent with the code employed in the current work, which will then be presented. ^h

2.2.1 Governing equations

Let us start again from the Navier-Stokes equations 2.4 and 2.5. Considering an isentropic flow we can neglect the energy conservation. Furthermore, if we assume the flow to be incompressible, and cancel mass source and bulk forces terms, we obtain:

$$\nabla \cdot \vec{u} = 0 \quad (2.45)$$

$$\frac{\partial \vec{u}}{\partial t} + \vec{u} \cdot \nabla \vec{u} = -\frac{1}{\rho} \nabla p + \nu \nabla^2 \vec{u} \quad (2.46)$$

Applying the curl operator to the momentum balance, through some vector algebra we obtain the vorticity equation:

$$\frac{\partial \vec{\omega}}{\partial t} + \vec{\omega} \times \vec{u} = -\nabla \left(\frac{p}{\rho} + \frac{u^2}{2} \right) - \nu \nabla \times \vec{\omega} \quad (2.47)$$

If then we assume the flow field to be irrotational the velocity can be written in terms of its potential (in a simply connected domain) as $\vec{u} = \nabla \Phi$, and the equations become:

$$\nabla^2 \Phi = 0 \quad (2.48)$$

$$\left(\frac{\partial \Phi}{\partial t} + \frac{p}{\rho} + \frac{u^2}{2} \right) = f(t) \quad (2.49)$$

^hThe theory reported in this section is taken from Buresti,² Katz and Plotkin,¹ Leishman,³ Segalini³¹ and Lee.³²

2. Theoretical background

which represent respectively the Laplace equation for the velocity potential and the unsteady Bernoulli equation, where $f(t)$ is an integration constant. We note two very important features: the solution of the velocity and pressure fields is decoupled, and viscosity is not present anymore, even though we did not make any assumption in that respect. Thus an irrotational field behaves as if viscosity was zero.

The Laplace equation is a linear partial differential equation requiring boundary conditions for its solution. The condition at the boundary far from the body is trivial and imposes the velocity equal to the undisturbed free stream one. The condition at the wall, or at the surface of our aerodynamic body, needs some more discussion. We know from boundary layer theory that fluid in close proximity to a surface actually sticks to it due to friction, and its velocity at the wall becomes zero: this is the no-slip condition. Unfortunately, no solution exists to the Laplace equation with such boundary conditions, except for the trivial identically null one. This has a fundamental physical explanation: as soon as a moving surface is introduced, vorticity is generated at the wall and injected into the field which cannot then be irrotational. However, from the Prandtl boundary layer theory we also know that for high Reynolds numbers, vorticity remains almost totally confined inside a thin layer attached to the body. More over, the pressure is constant in the direction perpendicular to the wall and equal to the one just outside of the vorticity layer. Thus the flow surrounding an aerodynamic body may be reasonably treated as irrotational, and the pressure field calculated at the body surface represents a first approximation of the real one (since it considers a boundary layer of zero thickness).ⁱ

The solution to the Laplace equation is obtained by imposing the impermeability condition instead of the no-slip one. Then the formulation of the problem becomes:

$$\nabla^2 \Phi = 0 \quad (2.50)$$

$$\left(\frac{\partial \Phi}{\partial t} + \frac{p}{\rho} + \frac{u^2}{2} \right) = f(t) \quad (2.51)$$

$$\left(\frac{\partial \Phi}{\partial n} \right)_{wall} = 0, \quad (\nabla \Phi)_{\infty} = \vec{u}_{\infty} \quad (2.52)$$

When solving the flow around a lifting body, such as an airfoil or a wing, an additional condition is necessary since lift generation is tightly coupled with the vorticity present in the boundary layer. Having neglected this vorticity, we leave undetermined the amount of circulation around our body, which as we know from the Kutta-Joukowski theorem is related to lift:

$$\vec{L} = \rho \cdot \vec{u}_{\infty} \times \vec{\Gamma} \quad (2.53)$$

The amount of circulation can be fixed by imposing the flow to leave the airfoil at the trailing edge, which is known as the Kutta condition. The actual implementation in the solver can take various formulations, as we will see.

Let us remind the simplifying hypothesis necessary to arrive to this formulation of the problem: the flow is considered irrotational and incompressible, the Reynolds number is ideally infinite, leading to a zero thickness boundary layer and thus no viscous effects, and most importantly the flow is always attached to the immersed bodies. If no additional corrections are made, a panel code will over predict lift since it does not account for the growth of boundary layer on the upper surface of the wing, and will not predict any form of drag except for the induced one. More over, onset and development of stall are not considered. While additional models can and are usually implemented to at least partially correct for those effects in the computations, they must be kept in mind as fundamental limitations to the potential model.

ⁱA coupled iteration between the potential flow solution and the boundary layer calculation can be employed to obtain an higher order solution, correcting for the thickness of the boundary layer by modifying the body geometry or introducing a transpiration velocity.

2.2.2 Panel methods

Panel methods exploit the linearity of the Laplace equation to build complex flow solutions upon superposition of elementary, known ones. The body and the shed wake are described by a structured grid which forms rectangular panels on which the discrete solutions, or singularities, are placed. By using distributed solutions, we automatically satisfy both the Laplace equation and the boundary condition at infinity.

The general solution of the velocity potential can be obtained by integration on the body and wake surfaces:

$$\Phi(\vec{x}) = \frac{1}{4\pi} \int_{S_B} \left[\frac{1}{r} \nabla(\Phi - \Phi_i) - (\Phi - \Phi_i) \nabla \frac{1}{r} \right] \cdot \vec{n} dS - \frac{1}{4\pi} \int_{S_W} \left[\Phi \cdot \vec{n} \cdot \nabla \frac{1}{r} \right] dS + \Phi_\infty(\vec{x}) \quad (2.54)$$

in which S_B and S_W indicate the body and wake surfaces, Φ_i indicates the potential inside of the body, and we separated the induced velocity potential Φ from the external flow potential Φ_∞ . We can now introduce the source and doublet potentials as:

$$-\sigma = \frac{\partial}{\partial n}(\Phi - \Phi_i), \quad -\mu = \Phi - \Phi_i$$

and the solution becomes:

$$\Phi(\vec{x}) = -\frac{1}{4\pi} \int_{S_B} \left[\frac{1}{r} \cdot \sigma - \mu \frac{\partial}{\partial n} \left(\frac{1}{r} \right) \right] dS + \frac{1}{4\pi} \int_{S_W} \left[\mu \frac{\partial}{\partial n} \left(\frac{1}{r} \right) \right] dS + \Phi_\infty(\vec{x}) \quad (2.55)$$

The distribution of the singularities on the surfaces is arbitrary and is chosen depending on the physics of the problem. The strength on the other hand is unknown and needs to be solved for by applying both the impermeability condition and the Kutta condition. This formulation for calculating the velocity potential is the usual implementation in panel codes, since it only deals with scalar terms. Point sources are used to displace streamlines to simulate thickness, and doublets are used to introduce circulation in lifting bodies. This can be confusing since, as we will see later, vortex lines and sheets are the fundamental components when simulating the wake of a rotor. We will briefly address the matter in what follows.

On the equivalence between a constant strength doublet panel and a vortex ring

From equation 2.55 we have the general expression for the velocity potential due to a doublet distribution on a surface panel:

$$\Phi_\mu(\vec{x}) = \int_S \left[\mu \frac{\partial}{\partial n} \left(\frac{1}{r} \right) \right] dS \quad (2.56)$$

in which the doublet strength μ can be a generic function of the local coordinates in the individual panel, i.e. its distribution on the panel can be arbitrary. Let us consider a uniform strength distribution, then the induced velocity is:

$$\vec{v}(\vec{x}) = \frac{1}{4\pi} \sum_{i=1}^4 |\vec{r}_i| (\hat{l}_i \times \hat{r}_i) \mu_o \int_l \frac{1}{|\vec{r}_i|^3} dl \quad (2.57)$$

where \vec{l}_i represents the i^{th} side, and \vec{r}_i the distance from it. We recognize the similarity to the velocity induced by a line vortex, given by the Biot-Savart law:

$$\vec{v}(\vec{x}) = \frac{\Gamma}{4\pi} \int_{-\infty}^{+\infty} \frac{d\vec{l} \times \vec{r}}{|\vec{r}|^3} \quad (2.58)$$

The resulting velocity is the same as the one induced by four line vortices each of strength $\Gamma = \mu_o$ placed at the sides of the panel: a vortex ring. Thus by using doublet panels we do not need to deal with vector quantities (which are necessary to describe vortex lines) and the approach is equivalent to using closed vortex filaments which inherently satisfy the Helmholtz conservation laws.

2.2.3 Vortex methods for rotor aerodynamics

Vortex methods are an alternative to Eulerian methods, or grid based methods. They are Lagrangian methods that only require computational elements where the “action” is, i.e., where the vorticity is. The computation neglects some details but is incredibly sped up. Sometimes, the increasing level of complexity of Navier-Stokes solving methods has a diminishing return in terms of accuracy. As a matter of fact, in many flows of physical interest, only a small fraction of the entire flow volume is occupied by fluid that contains vorticity. The rest of it is essentially vorticity free. For an incompressible fluid, it is sufficient to follow only the evolution of the vorticity field because the velocity field can be computed from it and from boundary conditions.

Rotary wing aerodynamics pose a difficult challenge to modeling and simulation as was mentioned at the beginning of this brief overview. Vortex methods offer a simplified description founded on some fundamental results, which are a consequence of applying the hypothesis made for the general potential flow model:

- i) vorticity is confined on the lifting bodies as *bound* vorticity and on zero thickness sheets representing the wake as *trailed* and *shed* vorticity. The entire flow field outside from them is irrotational.
- ii) Helmholtz theorems describe the vortex wake behavior thus vortex lines and sheets are material and are convected in the flow by the velocity field.

Which means that vortex tubes retain their identity and simply move as material volumes. Inviscid flows can thus be represented with Lagrangian computational elements that are, roughly speaking, sections of a vortex tube. Each element is convected with the fluid velocity, and the vorticity vector associated to that element is strained by the local velocity gradient.

Bound vorticity on the rotor blades originates from the cross-stream vorticity present in the boundary layers and is responsible for generation of lift. It is modeled by a distribution of doublets (equivalent to vortex rings) on a panel discretization of the mean camber surface. The distribution along the chord is arbitrary and in the current model is considered proportional to local profile thickness.

The span-wise variation of bound vorticity, or circulation, generates trailed, stream-wise oriented vorticity lines at each radial station of the blade. The strength of trailed vorticity is dependent on the gradient of circulation along the blade:

$$\gamma_t = \frac{\partial \Gamma}{\partial r} \quad (2.59)$$

The gradient is generally maximum near the tip where pressures must equalize and thus circulation goes to zero. Vorticity lines trailed in the near tip region rapidly roll up and combine in a concentrated tip vortex which is the main contributor to the induced flow on the rotor blades.

The azimuthal, or time variation of circulation gives rise to shed, span-wise vorticity lines because of the Kelvin theorem on conservation of total vorticity. The formula is:

$$\gamma_s = -\frac{1}{u_t} \frac{\partial \Gamma}{\partial \Psi} \quad (2.60)$$

where u_t is the tangential velocity at the blade. The wake is discretized into vortex rings containing both shed and trailed vorticity.

The basic implementation of the Kutta condition affects the position of the shed wake and its circulation. A Kutta panel of fixed elongation is placed after the trailing edge, parallel to the mean camber panel. The doublet strength, or circulation on the panel is calculated by imposing the velocity to be parallel to the panel, in other words the perpendicular component must be zero. If the trailing edge is not cusped, thus it has a finite angle, then it must also be a stagnation point and both the normal and tangential components must be zero. Additionally, the circulation on wake panels must

2. Theoretical background

be constant in time and the panels should be parallel to the local velocity vector. The latter condition is addressed in the calculation of the evolution in time of the wake panels position.

Derivation of the algebraic problem through influence coefficients

Having set the Kutta condition in three dimensions, imposing the boundary conditions on each blade panel leads to a system of linear algebraic equations which is solved for the strength of the singularities. We need to solve only for the sources and doublets placed on the blade outer and mean camber surfaces, in fact the circulation (doublet strength) of the wake panels is fixed and set by the Kutta condition. Non the less, induced velocity must be evaluated from all panels, including the wake. Lets assume the blade to be divided into N_B surface panels plus N_C camber panels, and the wake into N_W panels, or vortex rings equivalently. Additionally we have N_K Kutta panels. The boundary condition will be specified in each of the surface and Kutta panels at a *collocation point*. The circulation of the Kutta panels is set as equal to the circulation at the trailing edge (the last mean camber panel) at each time step.

By rewriting the impermeability boundary condition for each of the N_B collocation points through equation 2.55 we get:

$$\nabla (\Phi(\vec{x} \in S_B)) \cdot \hat{n} = \nabla \left\{ -\frac{1}{4\pi} \int_{S_B} \left[\frac{1}{r} \cdot \sigma - \mu \frac{\partial}{\partial n} \left(\frac{1}{r} \right) \right] dS + \frac{1}{4\pi} \int_{S_W} \left[\mu \frac{\partial}{\partial n} \left(\frac{1}{r} \right) \right] dS + \Phi_\infty(\vec{x}) \right\} \cdot \hat{n} = 0 \quad (2.61)$$

That is, for each collocation point on the blade surface panels, the summation of the influences of all body panels (surface and mean camber) and wake panels is needed. The integration is limited now to each individual panel element, and for a unit singularity element (σ or μ), it depends on the panel's geometry only. The integration can be performed analytically or numerically prior to this calculation. For a constant-strength σ source the influence of the generic panel j at the control point i is given by the integration on its surface:

$$\nabla \left[-\frac{1}{4\pi} \int_{S_j} \left(\frac{1}{r_{ij}} \right) dS_j \right] \cdot \hat{n}_i = A_{ij} \quad (2.62)$$

and for a constant-strength μ element belonging respectively to the mean camber surface (bound vorticity) and to the wake we have:

$$\nabla \left[\frac{1}{4\pi} \int_{S_j} \frac{\partial}{\partial n_j} \left(\frac{1}{r_{ij}} \right) dS_j \right] \cdot \hat{n}_i = B_{ij} \quad (2.63)$$

$$\nabla \left[\frac{1}{4\pi} \int_{S_j} \frac{\partial}{\partial n_j} \left(\frac{1}{r_{ij}} \right) dS_j \right] \cdot \hat{n}_i = C_{ij} \quad (2.64)$$

Those integrals are a function of the panel surface position (thus coordinates of its four corners) and the collocation point, thus only of geometric variables.

The equation can finally be rewritten in terms of the influence coefficients A_{ij} , B_{ij} , C_{ij} :

$$\sum_{j=1}^{N_B} A_{ij} \sigma_j + \sum_{j=1}^{N_C+N_K} B_{ij} \mu_j = R_i - \sum_{j=1}^{N_W} C_{ij} \mu_j, \quad i = 1 \dots N_B + N_K \quad (2.65)$$

which is a linear system of algebraic equations to be solved at each time step of the simulation and results in determining the values of singularities on the blade and on the newly shed wake panels. The constant R_i contains the external flow velocity and depends on the motion of the blade panel.

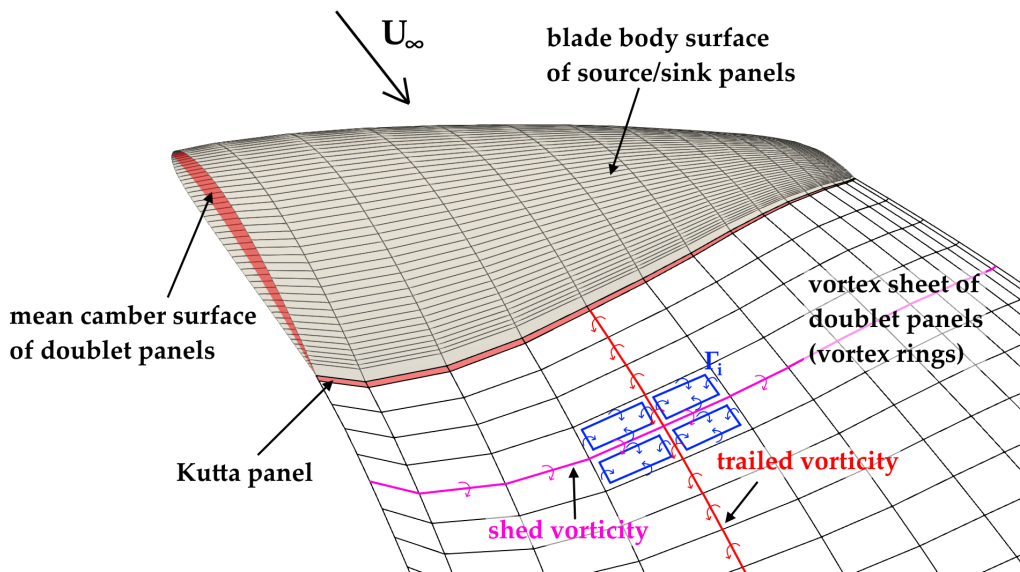


Figure 2.1: Numerical model of the blade and the wake. Each wake panel is a constant doublet distribution, which is equivalent to a vortex ring of constant strength. The difference in circulation between adjacent panel edges forms lines of vorticity which we refer to as streamwise trailed vorticity and spanwise shed vorticity.

Time integration of the free-wake position

Evaluation of the wake position is a fundamental part of rotary wing simulation, since it determines the core feature of rotor aerodynamics which is the inflow on the disc.

The time-marching free-wake method, in contrast to prescribed wake models, allows the vortex sheet consisting of vortex filaments to move in free motion as it propagates downstream and is deformed by its own induced velocity.

According to the Kutta condition, which acts as a bridge between the wake field and the lifting surface vortices in the vortex methods, the strength of a nascent shed wake vortex element is equal to the strength of a blade vortex element placed at the trailing edge in the previous time step. Once the wake vortices are shed, their strengths remain constant according to Helmholtz's theorem.

Since the vortex surface cannot bear external forces, the discrete vortex rings are allowed to convect freely staying tangent to the local stream velocity, which is induced by other vortex elements in the wake region. Biot-Savart's law in equation 2.58 provides the induced velocity components at any of the wake grid points, which are referred to as *Lagrangian markers*. The rate of change of their position is a partial differential equation in time and space which can be solved using finite differences, minding that especially in certain conditions the solution can be highly numerically unstable.

2.2.4 UPM: Unsteady Panel Method

The free-wake Unsteady Panel Method UPM^j is a potential flow solver developed at the Helicopter Division of DLR Institute of Aerodynamics and Flow Technology. It is capable of treating flows around complex three dimensional configurations in combination with a non-linear unsteady free wake. The code was originally developed for rotorcraft applications and can be used to evaluate the interaction of the main rotor wake with the tail rotor as well as with the fuselage and empennages. Its versatility allows for the implementation of multiple lifting rotors, which is the case of the present work. Reports

^jInformation in this section were taken from the UPM documentation.²²

2. Theoretical background

and comparison of the code results with experimental data and higher fidelity CFD codes can be found in the works of Ahmed,²⁶ Yin,^{27,28} Yin and Ahmed^{29,30} and Kunze.²⁵

The implementation of the potential flow solution follows the theory developed until now, and the lifting blade is modeled by:

- i) a source/sink distribution on the surface to simulate the displacement effect of the blade
- ii) a surface with bound vorticity (constant strength doublet panels) inside the blade (corresponding to the mean camber surface) to model the lift. To aid in numerical stability the circulation increases from zero at the leading edge to the full circulation at the trailing edge using an arbitrary weighting function.
- iii) a short zero-thickness elongation of the trailing edge along its bisector, called the Kutta panel, on which the Kutta condition of tangential flow at the trailing edge is applied, fixing the total strength of the circulation of the blade section.

UPM is an inherently unsteady method, capable of describing the evolution in time of the flowfield. At the start of any simulation, no wake is present and rotors (or wings) are impulsively set in motion. Then at each time-step (specified as degrees of rotor rotation) a row of wake panels is shed from the Kutta panel of each blade, and the system of equations 2.65 is solved using the updated influence coefficients (since the geometry of the problem changes).

The procedure to update the free-wake position and solve for the flow field at each time step can be summed up as follows:

- i) at the beginning of a time step, all rotor blades or wings move to their new positions.
- ii) while repositioning a blade a new wake row is released from the Kutta panels and is added to the existing wake. The spanwise distribution of circulation on a new row of wake panels is the same as the bound circulation of the blade. The circulation distribution on the wake row will remain unchanged throughout the whole simulation.
- iii) now the linear system of equations 2.65 is set-up and solved.
- iv) at the end of the time step the self-induced velocities of the wake are computed (i.e. the velocity induced by wake filaments onto each other) and the wake positions are advanced in time. The calculation can be done either through an explicit Adams-Bashfort method or a predictor corrector Adams-Bashfort/Adams-Moulton scheme. Thus, the whole wake surface is freely deformed according to the locally induced velocities.

Unsteady pressure and the Kutta condition

As said, the code considers an unsteady flow and calculates the pressure on the blades surface with the unsteady Bernoulli equation 2.51, which can be recast as the pressure coefficient c_p :

$$c_p = 1 - \frac{u^2}{u_\infty^2} - \frac{2}{u_\infty^2} \frac{\partial \Phi}{\partial t} \quad (2.66)$$

The calculation of $\partial \Phi / \partial t$ is computed through backwards finite differences. The behavior of the problem thus differs fundamentally from the steady flow case and requires a modification to the Kutta condition.

The classical Kutta condition requires a flow direction tangential to the bisector of the upper and lower airfoil surface. This is achieved by adding a so-called Kutta-panel at the trailing edge in the direction of the mean chord. Zero normal velocity at the center of the Kutta-panel is enforced. In

2. Theoretical background

steady aerodynamics, this ensures the same pressure on both sides of the airfoil at the trailing edge. In unsteady flow conditions, the classical Kutta panel treatment does not give identical pressures on both sides of the airfoil near the trailing edge. Therefore, an improved version, the so-called *Pressure Kutta Condition*, adjusts the airfoil circulation until the pressure difference vanishes.

The solution requires an iterative procedure due to the non-linearity of the pressure equations. A starting solution is obtained by computing the first iteration using the classical tangential flow Kutta condition. Experience has shown that for unsteady flow simulations, the Kutta panel should be about 2% chord length. A too-small panel may increase the number of iterations required for convergence of the pressure Kutta condition, but the converged solution is independent of the size of the Kutta panel.

Vortex core modeling

The tangential induced velocity of a 2D-vortex singularity is given by:

$$v_{\theta}(r) = \frac{\Gamma}{2\pi} \cdot \frac{1}{r} \quad (2.67)$$

The velocity $v_{\theta}(r)$ approaches infinity at the vortex center. In reality, effects of flow viscosity smooth out the high peak velocities. Modified equations have been proposed to model these effects near the vortex center, which also stabilize the inherently unstable vortex structure.

The vortex core models available in UPM are:

- Rankine: the flow is split into two regions: an inner region that rotates like a solid body (thus with constant non zero vorticity) and an outer region where potential flow is retained:

$$v_{\theta}(r) = \frac{\Gamma}{2\pi} \cdot \min \left\{ \frac{r}{r_c^2}, \frac{1}{r} \right\} \quad (2.68)$$

- Lamb-Oseen: derived from the Navier-Stokes equations as a solution in the form of a Gaussian:

$$v_{\theta}(r) = \frac{\Gamma}{2\pi} \cdot \frac{1 - e^{-\alpha(r/r_c)^2}}{r} \quad (2.69)$$

where $\alpha = 1.25643$, chosen to match experimental data.

- Kaufmann-Scully: this model provides a smoother transition between the core velocity and the outer potential vortex:

$$v_{\theta}(r) = \frac{\Gamma}{2\pi} \cdot \frac{r}{r_c^2 + r^2} \quad (2.70)$$

- Vatisas: a family of vortex models:

$$v_{\theta}(r) = \frac{\Gamma}{2\pi} \cdot \frac{r}{(r_c^{2n} + r^{2n})^{1/n}} \quad (2.71)$$

where n is a free parameter. Setting $n = 1$ gives the Kaufmann-Scully model, while $n \rightarrow \infty$ results in the Rankine model.

The swirl velocity for all models is plotted in figure 2.2, showing that the peak value differs across models, while they all converge to the irrotational model far from the center. The Lamb-Oseen vortex and Vatisas with $n = 2$ are in good agreement. Experimental data suggest the Lamb-Oseen model is the most accurate. Therefore, it is recommended to apply the approximate Vatisas $n = 2$ model for the tip vortex when the roll-up model is activated. In the wake, individual vortex filaments discretize

2. Theoretical background

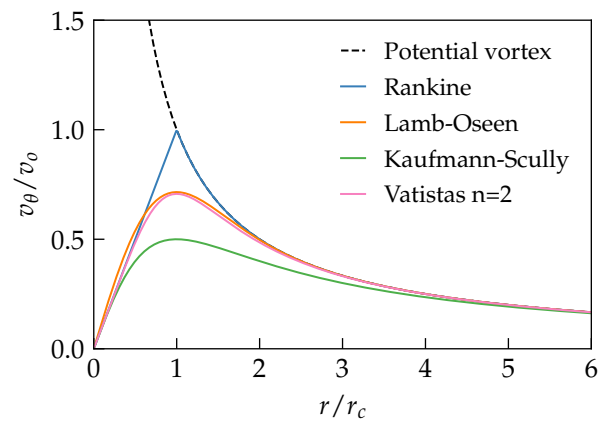


Figure 2.2: Induced velocity of 2D vortex singularity calculated with different viscous core models. The radial distance is adimensionalized with the core radius, and the velocity with the value at the vortex core calculated with the irrotational model.

the vorticity sheet without physical meaning. Thus, the Kaufmann-Scully model is preferred for wake modeling to reduce instabilities. Those indications were respected for the simulations in the present work. The actual dimension of the vortex core is a free parameter to be chosen by the user. It strongly affects the induced velocities on the rotor and the development of the wake itself. Too small of a value can induce instabilities and unphysical behavior. The value considered here, as reported in the results chapters, is equal to 80% of the cord length at 75% of the radius. Viscous diffusion can be modeled by a progressive enlargement of the core through various laws. A simple linear growth model was considered here.

3 | Methodology

In this chapter, we outline the simulation procedure adopted in this thesis to study the effect of rotor phase shifting on the noise directivity of manned multicopters, particularly during forward flight. The first section deals with the structure of the simulation tool-chain, through a step by step description.

In chapter 4 we will analyze in detail the application of phase shifting to the simpler case of small scale hovering rotors, using the described methodology. To apply the same concept to larger size crewed electric aircraft, a conceptual design of a feasible vehicle configuration was carried out in Donnini's thesis.³³ The design features a variable number of coplanar rotors controlled by collective pitch, and a scaled up version of the same blade geometry used in the validation campaign, as it is explained in detail in sections 3.2.1 and 3.2.2.

3.1 Description of the simulation tool-chain

To obtain the acoustic signature of the analyzed vehicle it is first necessary to perform an aerodynamic simulation, which provides the flow solution at the blades surface and assumes that the flight condition, the vehicle's attitude and all of the control inputs are known, as well as obviously the vehicle geometry. The result becomes then the input of the acoustic solver. In order to automate the procedure and to study the effect of relevant parameters, such as rotor phase vector, number of rotors, hub to hub distance or flight velocity, without having to manually change inputs each time, a toolchain was implemented through wrapping scripts in Python language. It operates the panel code UPM and the acoustic solver APSIM, handling the required input and output data for the two programs and performing some post-processing, without requiring user intervention except for the initial settings.

To reproduce realistic flight condition, a trim procedure which couples with the panel code was also developed by Donnini³³ and constitutes the first important step in the simulation toolchain, as will be explained in the following section.

The main toolchain script, after a preamble to import modules and define some functions, lists the required input parameters, which make up the simulation testcase:

- number of rotors: selected between 4, 6 and 8, configuration parameters are automatically adjusted
- phase angle matrix: contains as columns the rotor phase vectors, one for each test case we want to run
- flight condition: airspeed vector modulus and the flight path angle, limited to steady level climb or steady climb/descent.
- environment parameters: flight altitude determines all the atmospheric variables as prescribed by the ISA

3. Methodology

The rotor positions are automatically adjusted, as well as the drag model and the vehicle weight, as described in the geometry section 3.2.1. Some tuning parameters for the trim procedure can also be specified, they are discussed in the trim section.

The instructions of the program are then contained inside a for loop which iterates through the phase angles matrix, so that it is possible to run a batch of simulation testcases corresponding to a number of rotor phases combinations.

This outer routine is contained in the script `run_FM+UPM+APSIM_toolchain.py` and is articulated in three inner routines:

1. `trim_script.py` : the trim computation, which provides the collective pitch angle for each rotor and the aircraft attitude to achieve the prescribed steady flight condition.
2. `run_UPM.py` : the aerodynamic UPM computation of the simulation testcase, defined by the flight condition and the trim inputs.
3. `run_APSIM.py` : the acoustic APSIM calculation of the sound pressure level and the pressure time histories over a specified grid.

In each of those steps the program calls the corresponding script and modifies the input parameters inside of it before running it. As a last step, a folder corresponding to the testcase is created and all the relevant results are stored inside of it. The three main steps will be described in some more detail in what follows.

3.1.1 Vehicle trim procedure

The chosen multirotor vehicle configuration is numerically trimmed by a Python script^a. We refer here to the hexarotor configuration as the example, but an analogous procedure applies to the quadrotor and octarotor described in the vehicle layout section 3.2.1.

To achieve the desired acoustic wave interference, all sound sources need to be coherent, which means that they must have the same frequency. Thus all rotors must rotate at a fixed constant speed, and in addition to that each of them must keep the prescribed phase w.r.t. the reference rotor. This means that the traditional rpm control technique for multirotors which exploits speed variation to achieve thrust control cannot be employed.

We adopted here a collective pitch control technique, which still exploits differential thrust for pitch and roll authority but instead of varying the rotors rpm it changes the blade pitch, in the same way of the collective control of a helicopter. In this way, the speed setting of the electric motors would be free for the acoustic control. On the practical side, this would mean added complexity due to the needed pitch linkages and actuators, but would also have benefits in vehicle flight performance.³³ Moreover, the use of rpm control becomes impractical on larger size rotors due to the higher rotational inertia.

The possible steady flight conditions considered in the trim procedure are hover, level forward flight and steady climb or descent. Due to the symmetry of those conditions, a first approach was to limit the control to 3 degrees of freedom (DoF), considering only the surging, heaving and pitching motions. This proved to be satisfactory for the forward flight condition while greatly improving the computational time. It was thus adopted in the simulations for this thesis and the description will be limited to it in this brief section, but another procedure extended to 6 Dof was also developed.³³

Surge and heave motions are given by translational dynamics in x and z directions respectively, and pitching motion is determined by rotational dynamics around the y axis. The vector containing

^aThe trim procedure was developed and implemented by Donnini and is discussed in detail in his thesis work.³³

3. Methodology

the corresponding forces and moment resultant is expressed in a local horizontal reference system, which is parallel to the inertial one but fixed in the vehicle center of gravity, and is termed \vec{y} :

$$\vec{y} = \begin{bmatrix} F_x \\ F_z \\ M_y \end{bmatrix}$$

Those components are evaluated by averaging the aerodynamic forces acting on the rotors, provided by the UPM computation for each time step, over one rotation, and are then completed by the vehicle weight force and the drag of rotor booms and fuselage, which was estimated with a simplified model. The resultant longitudinal forces are the rotor thrust and drag (so called *H-force*), respectively perpendicular and parallel to the rotor plane, the fuselage drag applied to the center of pressure and parallel to the wind direction, and the rotor booms drag applied to the rotors plane geometric center. The drag produced by the rotors induces a pitch up moment, instead the fuselage drag creates an opposite pitch down moment, since the center of gravity is estimated between the rotors plane and the fuselage center of pressure. Other smaller sources of moments come from the rotor hubs as calculated by UPM due to lift dissymmetry in forward flight.

The objective of the trim is to make all \vec{y} components equal to zero or as close to it as possible. The so called trim vector \vec{x} must also contain 3 components in order for the problem to be solvable. A mapping matrix is employed to correlate it to the control inputs, which are the six collective pitch angles θ_0^i of the rotors, and to the attitude pitch (or elevation) angle Θ , which are the unknowns of the equilibrium problem. The mapping matrix is in this case:

$$\begin{bmatrix} \theta_0^1 \\ \theta_0^2 \\ \theta_0^3 \\ \theta_0^4 \\ \theta_0^5 \\ \theta_0^6 \\ \Theta \end{bmatrix} = \begin{bmatrix} -1 & 1 & 0 \\ 0 & 1 & 0 \\ 1 & 1 & 0 \\ 1 & 1 & 0 \\ 0 & 1 & 0 \\ -1 & 1 & 0 \\ 0 & 0 & -1 \end{bmatrix} \cdot \begin{bmatrix} x_1 \\ x_2 \\ x_3 \end{bmatrix}$$

The problem is then solved numerically for \vec{x} by means of a Newton-Raphson iterative algorithm, approximating the Jacobian matrix with finite differences. The main idea of the well known method is to linearize the behavior of the function to approximate its value at the n^{th} step:

$$\vec{y}^{(n)} \approx \vec{y}^{(n-1)} + \vec{J}(\vec{x}^{(n-1)}) \cdot \Delta\vec{x}, \quad \Delta\vec{x} = \vec{x}^{(n)} - \vec{x}^{(n-1)}$$

Setting $\vec{y}^{(n)} = \vec{0}$ we can solve the linear system and obtain $\vec{x}^{(n)}$.

Before the trim iteration, a UPM computation is performed automatically for a number of rotor revolutions sufficient to achieve a developed wake and converged rotor thrust. This serves as a basis for the subsequent computations which are restarted from it. Then the trim loop begins: the Jacobian matrix is computed by running one simulation revolution with a step input of each trim variable, then the approximate solution of the input vector is used to compute the new control variables and restart another revolution to compute the actual value of \vec{y} . If its norm is less than the tolerance the iteration is stopped. All the output produced is saved into a corresponding folder.

3.1.2 Aerodynamic simulation

Once the trim procedure is complete, the collective pitch angle for each rotor θ_0^i and the elevation angle Θ are collected and used as input for the UPM aerodynamic simulation of the multirotor in the prescribed steady flight condition.

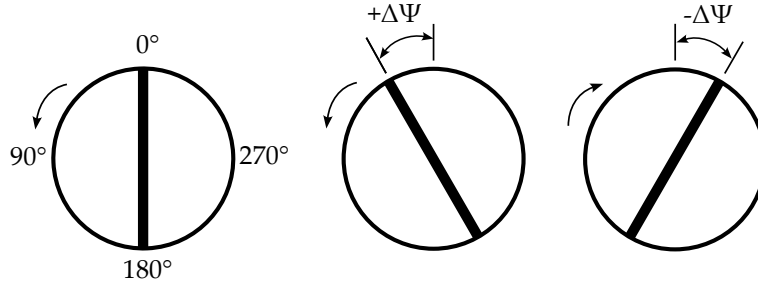


Figure 3.1: Representation of the rotor phase convention. Blade azimuthal angle is referred as Ψ positive counter-clockwise, phase difference by $\Delta\Psi$. On the left we have the reference rotor, on the right the other two with their phase shifted by $\Delta\Psi > 0$, thus both advanced. Depending on the direction of rotation, the phase angle Ψ will either be positive or negative.

The other fundamental input is the rotor phase vector $\vec{\Psi}$, which specifies the angular position of each rotor (meaning the position of the first blade) at the start of the simulation. That position obviously changes as the simulation goes forward, but since the rotors have exactly the same angular speed they remain synchronized. It is thus more straightforward to express the phase as relative to one of the rotors instead of as an absolute value. In this way we also avoid to consider the same phasing more than once, expressing it with different but equivalent vectors. The convention adopted here is the following: the first rotor is always the reference and thus is set at zero phase in the UPM computation, while we specify the phase difference, or phase shift, $\Delta\Psi$, for all others. Using this convention, the direction of rotation of the reference rotor is not important. A positive angle means that the rotor is advanced in its direction of rotation w.r.t. the first rotor, and a negative one means it is retarded. If we denote the rotor direction with χ equal to $+1$ for counterclockwise and -1 for clockwise, and set the reference rotor at $\Psi = 0$, the generic rotor shifted by an angle $\Delta\Psi \in [-90^\circ, +90^\circ]$ will start at:

$$\Psi = \chi \cdot \Delta\Psi$$

With the positive direction of the azimuthal angle Ψ being counterclockwise. A graphical explanation is shown in figure 3.1. The phase shift is limited to a value of plus or minus half a revolution because in this case the rotors have two blades spaced 180° from each other.

A corresponding script made to set program inputs and run UPM is called by the outer routine, after having updated its parameters first. The input to the UPM program is made up by the panel geometry files, a parameters file called `UPM.dat` and a file which specifies the position and motion of all model components called `motion.dat`. In `UPM.dat` we find all the options regarding the aerodynamic computations, the most relevant were explained in section 2.2.4.

The motion file is organized as a tree structure, in which the inertial frame is at the root and serves as the reference. Then each components is represented as a node, in which a list of one or more "elemental motions" describes the time-dependent transformation sequence from the coordinate system of the parent motion node to the one of the current node. Translational and rotational motions can be specified by either constant values or as functions of time with polynomials or periodic Fourier series.

The reference systems as used by UPM are the:

- i) inertial reference frame, earth-fixed, with the z axis pointing up.
- ii) local horizontal frame, parallel to the inertial frame but fixed to the aircraft center of mass.
- iii) *helicopter* body frame, fixed to the center of mass, follows the attitude of the aircraft. The x axis points to the nose, y to the left and z points up. If Euler angles are all zero it is parallel to the local horizontal.

3. Methodology

- iv) fixed rotor hub frame, parallel to the body frame and centered in the rotor hub.
- v) rotating hub frame, referenced to the fixed one but rotating around z at the rotor frequency.

We will refer to this frame system but keep the usual convention for the elevation angle Θ being positive nose up. In addition, whenever referring to the azimuthal angle, both around a single rotor and the complete vehicle, the convention will be to have the zero on the x axis and the positive direction counterclockwise looking from above.

In the present case, the helicopter node represents the multicopter vehicle's fuselage. Here we specify the attitude angles, in particular the elevation angle Θ which is a trim variable, and the motion of the aircraft with the true airspeed vector (TAS). Then each rotor has its own node referenced to the helicopter node which defines the location of the fixed rotor hub axis system w.r.t. the body axis. The rotating hub system then sets the angular speed of the rotor, and two more nodes define the position of the blades inside that system. Here we specify the phase (the angular position of the blade in the rotating reference system) and the blade pitching motion as a first order Fourier series, with only the first coefficient being non zero and setting the collective pitch of the rotor.

After the compilation of the input files, the simulation is started and it will run for the specified number of rotor revolutions, at the set time step. The output is then automatically organized by the script into separate folders:

- **tecplot:** located in the APSIM working directory, contains the pressure distribution on the blades surface for each time step in the last rotation written in tecplot .tec data format.
- **forces:** aerodynamic forces coefficients and integral values. The normal force coefficient c_n is given for each blade section at every time step, the thrust and other hub forces and moments are given integrated over the radius as function of rotation angle. Lift, drag and moment section coefficients are also saved.
- **inflow:** values of the induced velocity at the blade leading edge as function of rotation angle.
- **panels:** the program normally outputs all the blade and wake panels as a structured grid for the entire simulation. To save drive space, the wrapping script selects either the file for the last time step containing the complete wake or the entire last rotation.
- **pressure:** the pressure coefficient c_p is given over the cord of each blade section at last timestep.

3.1.3 Acoustic simulation

The acoustic prediction software APSIM requires as input the pressure distribution on the blades as calculated by the aerodynamic solver. For each time step of the last rotation, a data file is stored containing a structured grid representing the aerodynamic surfaces in the local horizontal reference system, with the relative unsteady pressure in Pa expressed as the difference between absolute pressure and undisturbed flow pressure p_∞ , as a cell centered variable.

The corresponding script first updates the simulation parameters file `inp.dat` with the environmental variables and the parameters of the microphone grid. The flight speed vector is also specified, and is considered in the calculation by solving for sound propagation in a uniform flow. The simulation requires a collection of points, so called *microphones*, on which to calculate the value of the acoustic pressure. Those must be specified as a structured grid with indexes (i, j, k) , which is usually a surface and thus with $k = 0$. The script automatically handles different grid files as needed. A description of the simulation setting and microphone grids used is found in section 3.3.

The microphone grid is specified in the same reference system as the blade motion. This means that relative motion between the ground and the vehicle is not considered and doppler effect caused

3. Methodology

by it is neglected^b. The effects of ground reflection and of atmospheric absorption were neglected as well in the current work.

The program routine is then divided in two main parts: the computation of sound emission (or better of the estimation) for the non synchronized configuration, and the complete simulation which considers the effective synchronization of rotors and computes the sound sources all at once. To estimate the noise emission of a configuration of rotors equivalent to the one considered in the aerodynamic simulation but with uncontrolled phase relation between rotors, some simplifying assumptions were made:

- the phase of each rotor is random. This is what generally happens with rpm control of motors: the controller follows the speed set point but does not track the relative phase.
- the rotor-to-rotor and rotor-to-wake aerodynamic interferences are weakly dependent on the rotor relative phasing. This was discovered to be a reasonable assumption in forward flight.

As a consequence the total acoustic emission was calculated summing on a linear energy basis, which is equivalent to summing in the frequency domain, the acoustic pressures generated by each rotor. Operatively, the script isolates each rotor pressure data and performs a separate acoustic simulation, then the squared rms value of the acoustic pressure in each grid node is summed between all rotors. The output is the SPL distribution on the considered grid, representing the baseline to which we can compare the effect of rotor phase synchronization.

Next, the complete simulation is computed from the unaltered pressure files from UPM, for the specified microphone grids. The output from the APSIM program consists in three data files: the acoustic pressure time histories over each grid point, the corresponding Fourier spectrum showing the SPL values across the integer and half-integer multiples of the blade passing frequency, and the overall SPL (OSPL) value. The sound pressure levels computed with the application of some usual weighting functions in acoustics such as A-weighting are also available.

3.2 Multirotor aerodynamic model

The vehicle considered in this study is a conventional VTOL (vertical take-off and landing) multi-rotor design, in which the rotors are laid out at the vertices of a regular polygon, in a plane on top of the fuselage. As discussed in the trim procedure section, the control of rotor thrust is performed by collective pitch variation in order to maintain synchronization. The aerodynamic model implemented consists only of the lifting surfaces, i.e. the rotor blades, while the fuselage and rotor booms are considered only in the trim procedure as previously mentioned through a simplified drag model.

3.2.1 Rotor geometry and scaling

The adopted rotor geometry features two blades model CF125 designed by KDE Direct, the same used in the experimental setup by Schiller et al.⁶ described in chapter 4. Since the simulation toolchain was validated on the acoustic data reported in said study, it was decided to keep the same blade geometry in the course of this research work. The geometric data was obtained by scanning the blade and then approximating the profile with 4 digits NACA airfoils with sharp trailing edge, to obtain a smooth shape. The blade profiles are shown in figure 3.2, and in 3.4 we see a rendering of the blade mesh generated for the panel solver UPM. Table 3.1 lists the relative parameters. A root cut-out of 30% was used in order to avoid instabilities of the calculated free wake at low radial stations.

Such geometry was scaled up from its original dimensions in order to design a parametric multi-rotor configuration suitable for a manned size vehicle. The criteria was to keep a tip speed and a

^bNote that the effect of the moving flow on sound propagation is considered, and also the Doppler effect caused by relative motion between rotating noise sources on the blade and the grid observer.

3. Methodology

Table 3.1: Blade mesh parameters.

blade sections	16
airfoil panels	94
total panels	1410
root cut-out	30% radius

Table 3.2: Variable pitch blade design parameters.

Radius	1.1m
c_{75}	0.168m
tip speed	121m/s
collective range	$0^\circ - 20^\circ$

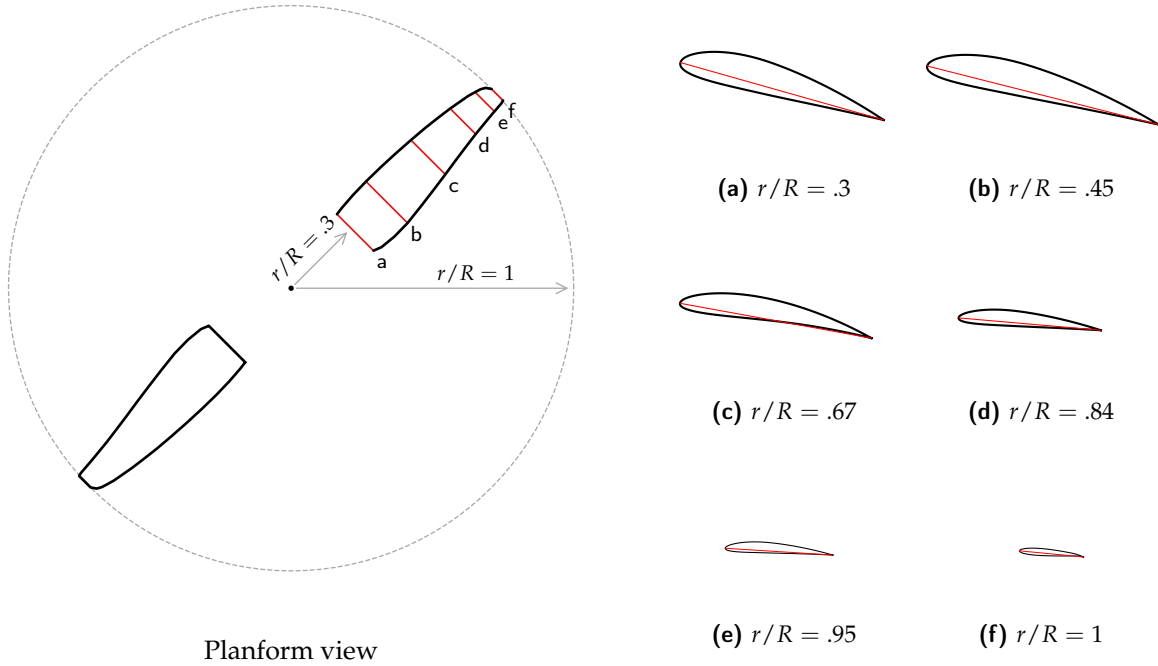


Figure 3.2: The two bladed rotor geometry, sectioned at the highlighted radial stations to show the corresponding blade profile. The chord is drawn as a red line.

hover thrust coefficient near the values of the original size fixed-pitch propeller, ensuring to fall inside a suitable range of pitch angle, avoiding the onset of stall. Even then, it is inevitable that the up-scaled rotor will not be in the design conditions intended by the manufacturer, not only because the Reynolds number is affected ($\sim 10^5$ for the original and $\sim 10^6$ for the up-scaled) but also because since variable pitch is introduced, geometric and consequently kinematic similitude cannot be maintained. Future developments in noise directional control through rotor phasing would certainly benefit from additional experimental campaigns for result comparison.

The up-scaled rotor dimensions and characteristics are listed in table 3.2, and the distribution of twist and chord length along the radius is represented in figure 3.3. As can be seen, the geometry already has 16° of pitch at the root. Hover is maintained with an additional 3.5° of collective.

3.2.2 Parametric vehicle configuration

The reference configuration is the hexa-rotor, designed by Donnini³³ to be similar to the Volocopter 2X. In addition, to be able to study the effect of rotor number on the phase shift method, a total of three configurations were considered with either 4, 6 or 8 rotors. The blade geometry, rotor radius and rotational speed are kept constant across configurations. The weight of the vehicle, as well as the approximated fuselage drag model were scaled with the number of rotors in order to keep

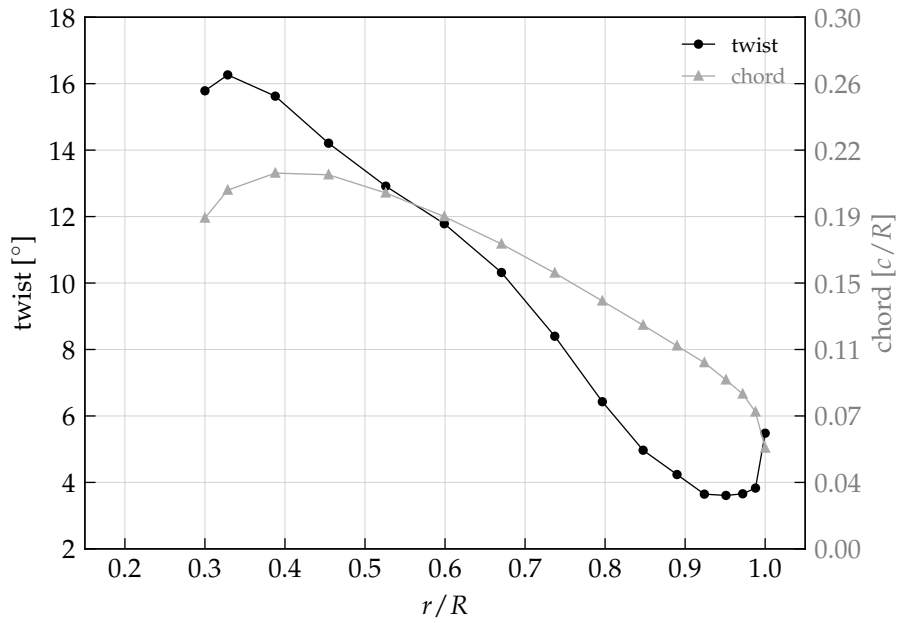


Figure 3.3: Radial distributions of the rotor blade chord and twist (pitch) angle. The chord is expressed as a fraction of tip radius.

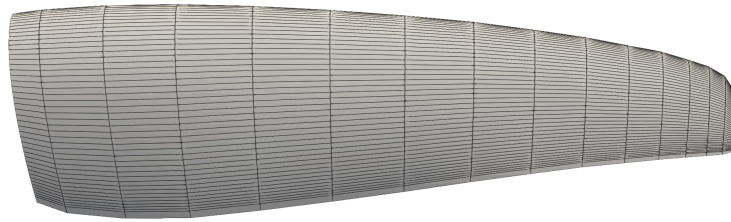


Figure 3.4: Rendering of the blade mesh used as UPM input.

the same disc loading and a similar attitude in forward flight. Relevant parameters are listed in table 3.3, and in figure 3.5 we find the layout of rotors seen from above. Adjacent rotors are always counter-rotating: this is a requirement for flight controllability in the quad-rotor and the hexa-rotor, but different arrangements could be used with 8 rotors. For example, a configuration which still grants maneuverability consists in using co-rotating couples, alternating counterclockwise to clockwise rotating ones.

In the current aeroacoustic analysis, due to time constraints, the application was limited to the quad-rotor and the hexa-rotor, thus we leave out the description of the octa-rotor and we refer to Donnini³³ for more details.

The preferred forward flight direction always intersects two rotors, and coincides with the x-axis in figure 3.5. The rotors are numbered from above starting with the one immediately on the right of the flight direction and proceeding clockwise. It is notable that different orientations in forward flight are possible and they affect the acoustic signature, as studied by Smith et al.¹¹

Table 3.3: Design parameters of the vehicle configurations.

	Quad-rotor	Hexa-rotor
Weight [kg]	300	450
Tip-tip diameter [m]	4.67	7
Hub-hub distance [m]	3.3	3.5
Rotor diameter [m]	2.2	"
Disc loading [N/m^2]	735.75	"

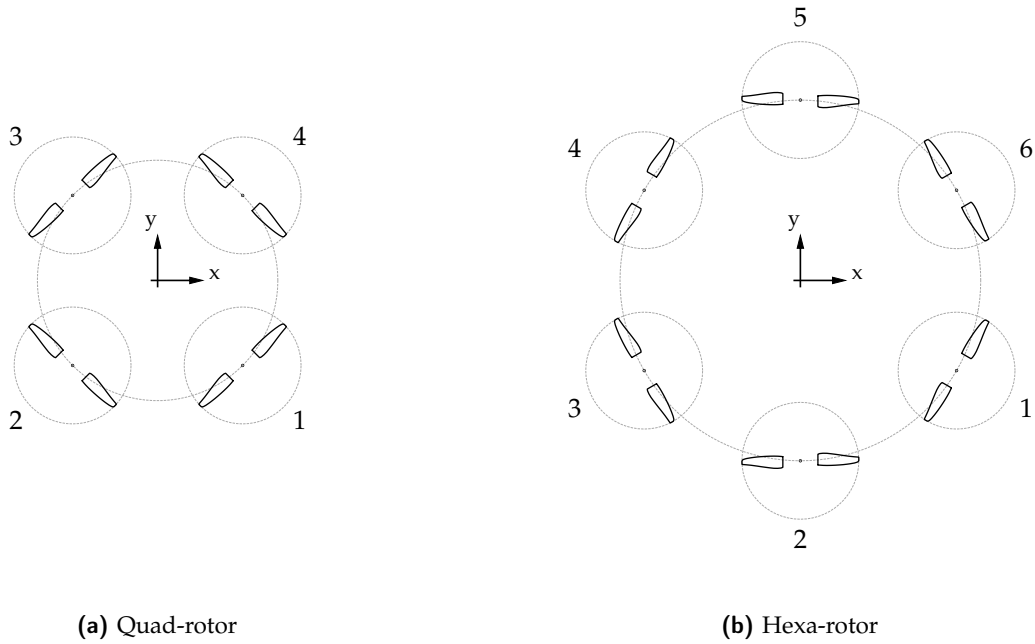


Figure 3.5: Parametric rotor layouts.

3.3 Flyover simulation setting

As said, the aerodynamic simulation is performed for the specified vehicle geometry, with the trim rotor collective pitch inputs calculated in the considered flight condition. Then its output is used to simulate sound propagation. Since the results presented in this thesis focus on forward flight, we will limit the description to the flyover simulation case.

In each forward flight simulation, two measurement grids are used:

- the hemispherical grid, centered with the vehicle, with a radius of 14.5m.
- the ground plane, a rectangular grid placed under the vehicle at a distance equal to the flight altitude, measuring 450x300m.

The hemispheric surface captures all of the sound propagation that can affect any ground observer, and is used mainly to calculate the radiated sound power and the noise directivity. Its distance from the source is estimated by accounting for validity of the far-field approximation. The ground plane measurement grid represents what in aeroacoustics is commonly referred to as the noise *footprint* or the *noise carpet*. It gives an estimate of sound perceived by ground observers, in a more direct way

3. Methodology

Table 3.4: Microphone grids parameters.

	hemisphere	ground plane
grid points	976	961
dimensions	15m radius	450 × 300m sides

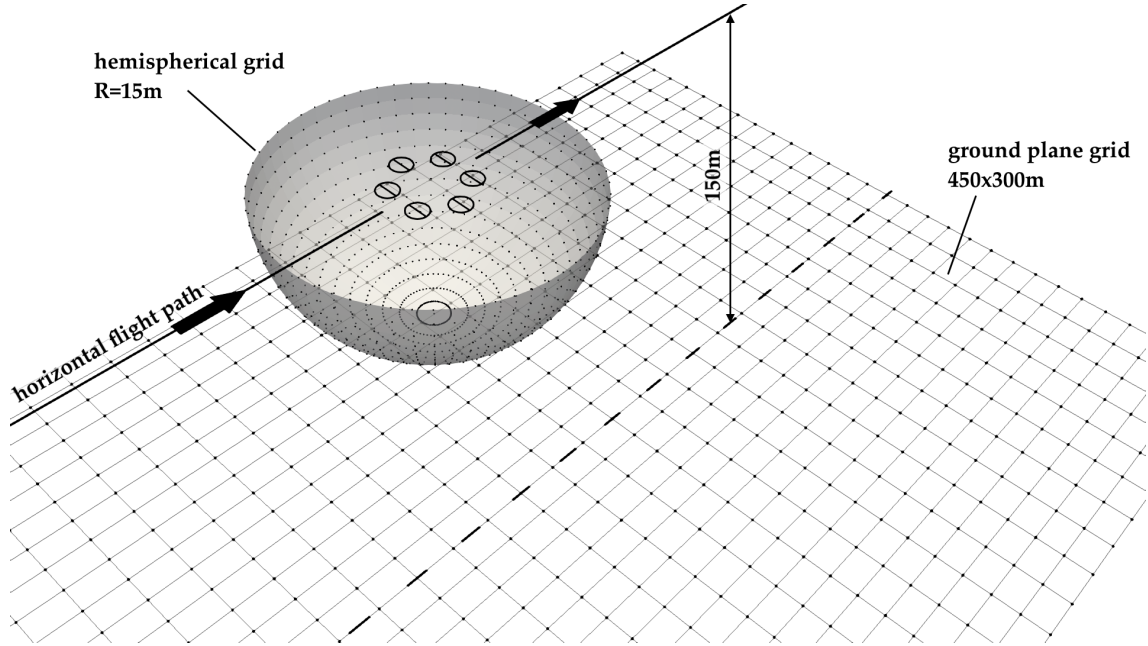


Figure 3.6: Acoustic simulation setting in flyover. The vehicle (hexa-rotor in this image) is represented by its rotors. The two measurement grids, the hemisphere and the ground plane, show a dot for each microphone location. The dotted line passes through the middle of the ground plane.

than the hemisphere measurements. It is although limited by the fact that radial distance from the source is not constant and thus noise levels are affected by the inverse square law. This must be kept in mind when evaluating the effects of phase shift on sound directivity.

The altitude at which simulations are conducted, and thus distance between vehicle and ground plane, was chosen as 150m. Considering the ISA (International Standard Atmosphere) model with a ground temperature of 23°C, the corresponding air density and speed of sound are respectively 1.17473kg/m³ and 344.417m/s. The FAA (Federal Aviation Administration) code of federal regulations (CFR) specifies the helicopter noise requirements for certification in title 14, chapter 36 under subpart H.³⁸ It requires sound measurements for fly-overs to be made at this distance and prescribes the SPL threshold values, corrected for human sound perception. This specification was adopted not to specifically refer to noise limits for light helicopters, but mainly to use a recognized standard. The aim of the study is in fact to study the potential noise reduction on an example configuration and not to achieve a specific noise requirement. In figure 3.6 we can see the setting of the acoustic simulation for the flyover.

3.4 Optimization of rotor phases for directional noise reduction

The noise reduction method is based on phase change in sound sources to obtain destructive interference of pressure waves at selected observer locations. In our case the rotors are the sources, or better the rotor blades, and we control the azimuthal position of each one thereby changing the phasing.

3. Methodology

Solving analytically for the set of phases which produce the desired interaction in a point in space is intractable even for a small number of sources,⁷ let alone doing it for multiple observer locations. On the other hand, solving it by brute force would require a very high number of calculations, as the amount of possible combinations of phases is given by:

$$N_c = \left(\frac{360^\circ}{\delta\Psi \cdot N_b} \right)^{N_r - 1} \quad (3.1)$$

in which $\delta\Psi$ is the chosen angular resolution in degrees, N_b is the number of blades and N_r the number of rotors. In the exponent we have $N_r - 1$ since one rotor is always the reference, as explained in section 3.1.2.

Thus the approach was to apply an optimization algorithm to the simulation toolchain. To reduce the computational time, a simplified simulation procedure was adopted which does not account for aerodynamic interactions between rotors and uses the output of a single aerodynamic simulation for an isolated rotor, in the test flight condition, to run the complete acoustic simulation. The results are then computed with the complete simulation procedure. The main focus was the application to a trimmed forward flight condition as set up in the previous section.

The objective function of the optimization is the mean value of the overall sound pressure level over a specified region of the ground plane in figure 3.6, mathematically:

$$\min \left(\frac{1}{N_{obs}} \sum_{i=1}^{N_{obs}} SPL_i \right) \quad (3.2)$$

with N_{obs} being the number of observer points (microphones or grid points), and subscript i indicating the single observer. As said, the aim was to find the set of phases which would produce a local minimum of SPL in the desired region. The optimization procedure, which analyzes only the specified set of observers and not the entire plane, looks for the absolute minimum described by expression 3.2 with respect to the variable space given by the phase angles. It is thus important to underline that the mean value of SPL in the minimized region may not be the absolute minimum of the entire observation plane but only a local one.

3.4.1 Fast aeroacoustic simulation with single rotor aerodynamic solution

As explained in chapter 2, the mid-fidelity solver UPM offers a considerably reduced computation time with respect to higher fidelity counterparts, while still being able to capture the aerodynamic phenomena influencing the study. Non the less, the optimization study asked for a great number of computations to be performed varying the rotor phase angles, and it led to the necessity of speeding up the procedure even more.

The fundamental idea was that the interference between the aft rotors and the wakes shed by the front ones could be, in some flight conditions, weak enough to be neglected. This would happen for a sufficiently high flight speed and attitude pitch down angle. Thus a custom toolchain was developed by the author which performs a single aerodynamic simulation of an isolated rotor, in the same attitude and trim state as the complete configuration. The resulting grid files representing the rotor blades with the pressure distribution are then used to build the complete rotor configuration, by translating them into the correct position, and shifting them in time to adjust for phase angle. The resulting data can then be used to calculate the acoustic interference of phased rotors. This reduces drastically the required computation time not only because the UPM simulation considers only one rotor, but also because if the flight condition stays the same, it is possible to test different phase angles without having to recompute the aerodynamic solution and only perform the acoustic one.

3.4.2 Surrogate based optimization

Since the optimization problem is not convex, meaning that there exists multiple set of phases which result in a local minimum of the average SPL in a certain region, the algorithm must incorporate strategies to avoid getting stuck in sub-optimal values. The optimization software here adopted is the surrogate based optimization algorithm POT (Powerful Optimization Tools) with SuMo (Surrogate Modeling) developed by Gunther Wilke. We report in this section a very brief summary of the theory explained in detail in his PhD thesis.³⁵

Surrogate based optimization (SBO) is a sub-group of numerical optimization strategies and is an acceleration mechanism for regular optimization. Through mathematical abstraction of the true function, here the simulation code, a quickly to evaluate surrogate is created. The search of the optimum in this surrogate is a lot faster than in the true function. However, this mathematical abstraction is likely to lack in accuracy compared to the true function and thus has to be improved in regions of interest.

SBO typically follows these steps:

1. Design of Experiments (DoE): Initial sampling of the design space using techniques like Latin Hypercube Sampling or space-filling designs.
2. Surrogate Model Construction: Common models include Gaussian Processes, Radial Basis Functions, and Polynomial Regression.
3. Optimization and Refinement: While regular optimization directly searches for the best goal function, surrogate-based optimization requires adaptive sampling to find the best design. This means improving the surrogate model even in less relevant regions to confirm their insignificance. A proper optimization strategy and careful selection of algorithms are essential for choosing infill points. Depending on the order of the design space and on the application (global or local) different algorithms are employed, such as the Hooke and Jeeves pattern search, the Differential Evolutionary algorithm and the Simplex pattern search method.
4. Stopping Criteria: Optimization stops when a convergence criterion, such as function improvement or model confidence, is met.

3.5 Calculation of sound power and far-field approximation

To evaluate the sound power radiated through the hemisphere, the measurement grid is considered to be in the acoustic far-field and thus the approximation of locally planar wave front is employed. As a consequence pressure and velocity fluctuations are synchronized and the acoustic particle velocity has only a radial component perpendicular to the wave front. The sound intensity can then be calculated from the pressure values alone:

$$\vec{I} = \overline{p' \vec{u}'} , \quad |\vec{I}| \approx I_r = \overline{p' u'_r} \approx \frac{\overline{p'^2}}{c_\infty \rho_\infty} = \frac{p_{rms}^2}{c_\infty \rho_\infty} \quad (3.3)$$

where p' and \vec{u}' are the acoustic pressure fluctuations and particle velocity, with r indicating the radial component. The radiated sound power is obtained by multiplying the local surface element by the normal component of the intensity and summing up over the entire hemisphere. Given the hypothesis, the normal component is equal to the radial component of the intensity (simply named I) and thus the overall power P is obtained through:

$$P = \sum_{i=1}^N I_i A_i \quad (3.4)$$

3. Methodology

The value of $\overline{p^2}$ in the center of the local panel is obtained by interpolation of the values at the grid nodes. The validity of the far-field approximation can be assessed through some theoretical considerations, as a first approach. We will here illustrate the basic theory behind it.

Near-field and far-field are a differentiation of the pressure fluctuations field into sub-domains in which the main wave propagation mechanism changes. The existence of those sub-domains can be seen in the formulation of the general free-field solution to the wave equation in presence of a bounded continuous distribution of point sources, which we derived in chapter 2. Equation 2.18 explicitly shows a part of the pressure signal which scales as $1/r^2$, thus significant only for observers near the source, and a part proportional to $1/r$ which is compressible in nature and dominates the regions far from the source.

The same function written in the frequency domain, i.e. $\hat{p}'(\vec{x}, \omega)$, shows compressibility effects, related to speed of sound c_∞ , only in the form of the wave number $k = \omega/c_\infty$, which is always multiplied by r . For $k \cdot r \rightarrow 0$ the pressure field will behave as incompressible. We define the distance $d_s(\vec{x})$ as the minimum distance between the observer and the source region (if the source is not a point), which means that:

$$d_s(\vec{x}) = \min_{\vec{\zeta} \in V_s} [|\vec{x} - \vec{\zeta}|] = \min_{\zeta \in V_s} [r] \quad (3.5)$$

The acoustic far-field, the region dominated by unsteady, compressible processes, is then characterized by a ratio

$$\frac{d_s}{\lambda} = \frac{d_s \cdot k}{2\pi}$$

which is of the same order as unity, i.e. $d_s/\lambda \sim 1$, no matter the characteristic geometric extension of the source region (thus independently of the compactness of the source).

In the present case, the characteristic wave number is the one calculated on the BPF, and the distance to be considered is the radius of the measurement hemisphere minus the distance between the center and the tip of the furthest propeller from it. Speaking in terms of n multiples of the rotor diameter D :

$$\lambda = \frac{c_\infty}{BPF}, \quad \frac{d_s}{\lambda} = \frac{n \cdot D \cdot BPF}{c_\infty}$$

It is interesting to express the BPF as function of the tip speed v_t :

$$BPF = \frac{\omega}{2\pi} \cdot N_{blades} = \frac{\omega}{\pi}, \quad \omega = \frac{v_t}{R} = 2 \frac{v_t}{D}, \quad \lambda = \pi c_\infty \frac{D}{2v_t}$$

thus:

$$\frac{d_s}{\lambda} = \frac{n \cdot D}{\lambda} = \frac{2n \cdot v_t}{\pi \cdot c_\infty} \quad (3.6)$$

which shows that the ratio is proportional to the rotor tip-speed and the separation distance expressed as a multiple of the rotor diameter. In the experiment from Schiller⁶ studied in chapter 4, the separation was approximately 5 times the diameter, the tip-speed 84.65m/s and the ratio was then around 0.12. Since the hypothesis was assessed in the reference paper by checking that the acoustic pressure had indeed a $1/r$ dependency at the considered distance, this ratio may then be deemed sufficiently high. It is important to note that the exact boundaries of near and far-field often depend on the specific phenomenon, and this considerations hold for noise generated by rotors, being limited to tonal noise at the blade passing frequency, which is expected to be the predominant harmonic.

4 | Validation of the method with experimental data

The simulation toolchain applied to hovering, fixed-pitch propellers was validated with the experimental data presented by NASA research scientist N. Schiller in his work "Tonal noise control using rotor phase synchronization".⁶ In his experimental campaign on phase control of fixed pitch propellers he investigated the possibility of altering the tonal noise signature of a double rotor configuration in the hover condition. The experiments were performed in the NASA Langley Structural Acoustic Loads and Transmission (SALT) anechoic chamber. Together with experimental data, he also reports results from a numerical model.

The experimental case, as well as some other case studies performed numerically by Schiller, were reproduced with the methodology presented in chapter 3 and the results are reported in what follows. The main focus of the validation was establishing if the influence of rotor phasing and rotor-to-rotor interactions on the magnitude and directionality of the noise signature was correctly captured by the simulations.

4.1 Description of the NASA experimental setup and numerical model

4.1.1 Experimental setup

The tests were performed on a static dual rotor assembly. Both clockwise and counter-clockwise propellers were used depending on the test case. Each rotor has two blades model CF125 from KDE Direct, with a diameter of 317mm. A detailed description of the blade geometry has been given in section 3.2.1. Hub-to-hub separation is 400mm, which corresponds to 1.26 times the rotor diameter and gives a tip clearance of 83mm. Each hub attaches to a short shaft placing the rotor plane at a distance of 59mm from the horizontal support arm. Both shafts are connected to a single brushless DC motor by means of a belt and pulleys, in this way the rotation is synchronized and the relative phase offset is mechanically fixed. It must be noted that phase control is technologically achievable even with independent motors by means of a microcontroller coupled with electronic motor speed

Table 4.1: Parameters of the NASA experimental case study.

blade geometry	KDE-Direct CF125
rotor diameter	317mm
Hub-to-hub separation	400mm
rotational speed	5100rpm
BPF	170Hz

Table 4.2: UPM simulation parameters for the experimental case study.

time step size	6°
number of revolutions	16
vortex core radius	0.8 · c_{75}
environment	SL 23°C
wake size	unrestricted

4. Validation of the method with experimental data

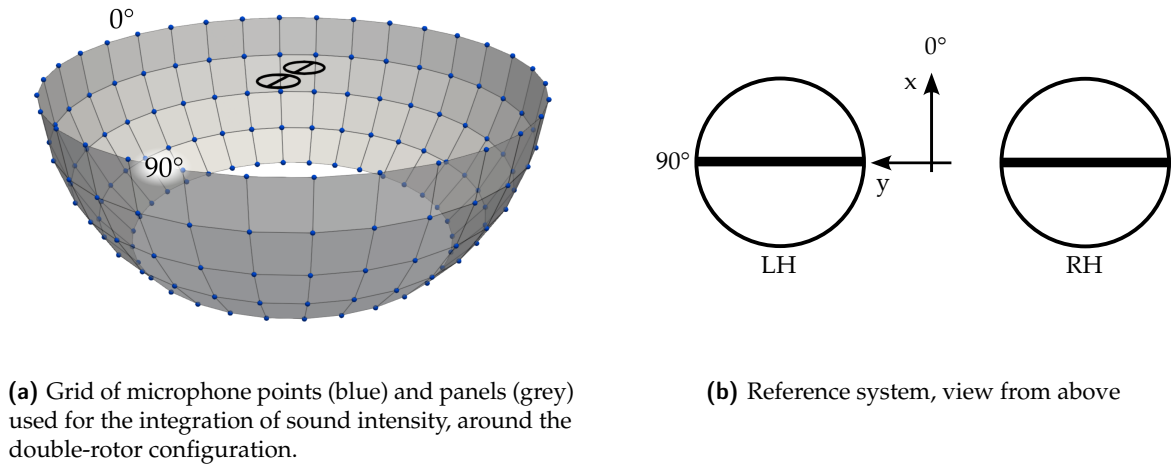


Figure 4.1: Scheme of the NASA experimental setup.

controllers, as was demonstrated by Patterson⁸ and Valente.⁹

An optical tachometer was used to set the propeller speed to $5100rpm$ corresponding to a blade passing frequency (BPF) of 170Hz. A multi-axis load cell measured the total thrust. The rotor assembly was mounted on a rotating stage on top of a test stand which located it in the center of the anechoic chamber. Interior dimensions of the chamber are 9.63 by 7.65 by 4.57m. The wedges on walls, ceiling and floor eliminate wave reflections creating a near free-field acoustic environment down to about 100Hz.

For the acoustic measurements, five free-field microphones were placed at a radial distance of 1.9m from the center of the test bench, all on the same azimuthal angle starting at 0° elevation angle and going down to -11.25° , -22.5° , -33.75° and -45° . Keeping the microphone array stationary, the test bench was rotated to take the measurements for a total of 31 different azimuthal angles in 11.25° steps, in order to capture the sound directivity on a portion of the hemisphere, as shown in figure 4.1a. The direction of rotation of the rotors is described as seen from above, and a right handed reference system is placed with the origin in the mid point between the rotors, resting on the rotors plane, with the x axis pointing to the front of the rotors and the y axis pointing to the left hand propeller, as can be seen in figure 4.1b. The azimuthal angle is considered 0 at the x axis and positive counter-clockwise.

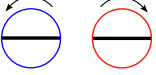
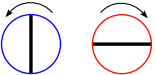
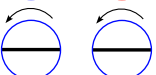
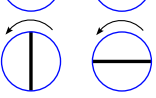
4.1.2 Data post-processing

The output of the test were the pressure time histories over the measurement points. From them it is possible to calculate the acoustic spectra using an FFT algorithm. Since the study was focused on tonal noise corresponding to the BPF, the root mean square of the pressure fluctuations p'_{rms} and consequently the sound pressure level (SPL) were calculated by integrating the spectrum over an interval of 10Hz centered around said frequency. The reason is flow recirculation in the test room, which influences the harmonic content of rotor noise due to the wake being ingested and causing unsteady loading events. To isolate the steady loading noise source the integration around the BPF was performed as described.

To evaluate the sound power radiated through the hemisphere, the measurement grid was considered to be in the far-field and thus the approximation of locally planar wave front was employed. The procedure is the same as described in section 3.5. A note should be made on the fact that the measurement grid resulting from the experiment stops at an angle of 45° below the rotors plane, instead the integration performed on the output of the numerical simulation included the whole hemisphere. However, the sound power values were normalized to account for this difference, as

4. Validation of the method with experimental data

Table 4.3: Test cases matrix. Rotors viewed from above, left hand rotor stands on the left.

Testcase	Configuration	Phase shift	Scheme
(a)	Single ccw	n/a	
(b)	Counter-rotating	0°	
(c)	Counter-rotating	90°	
(d)	Co-rotating	0°	
(e)	Co-rotating	45°	
(f)	Co-rotating	90°	

explained in section 4.2.3.

4.1.3 Mathematical model

In the referenced paper, the experimental data was used to validate a numerical model which predicts the rotor loads and calculates the propagated sound using the acoustic analogy for thickness and loading noise, similarly to what was done in the present work (the difference stands mainly in the aerodynamic modeling).

The isolated rotor loads were calculated by solving the 2-D flow around the blade sections, generating airfoil tables, which were then an input to solve for the thrust using the blade element momentum theory (BEMT). The inflow velocity was also an input.

The blade geometry and the radial loading were then used to calculate the tonal noise by means of the Farassat1 formulation of the Ffowcs-Williams Hawkins equation (see section 2.1.5).

This model was used to study the effect of rotor distance, in terms of compactness ratio, on the radiated sound power. Moreover, it was used to assess the potential benefit of phase synchronization on a multi-copter with pairs of co-rotating synched rotors. Both studies are discussed further down the chapter.

4.2 Comparison with experimental results

A total of six test cases were considered in the experimental campaign and were reproduced numerically in this work. The test matrix is displayed in table 4.3. The reported results of the experiments were the overall sound pressure level distribution around the azimuth (SPL polars) at two elevations of the hemisphere, which show the noise directivity, plus the total thrust measured by the load cell.

In the current work, each simulation was performed for a number of revolutions sufficient to reach a reasonably converged result, as analyzed further in what follows.

4.2.1 Convergence of calculated rotor mean thrust

UPM is an inherently unsteady solver and each simulation begins without any wake panels and with the rotors being impulsively started, thus it always contains the starting vortex. For this reason, the

4. Validation of the method with experimental data

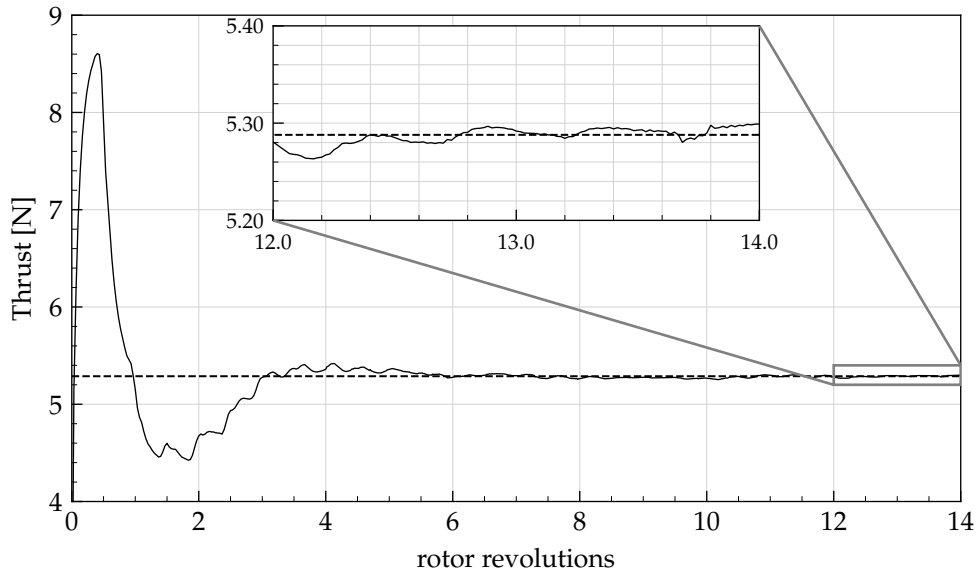


Figure 4.2: Complete thrust timeseries of the isolated single rotor UPM simulation showing the convergence of the computation. The dotted line is the thrust value averaged over the last 3 revolutions.

calculation requires some simulation time to converge to a steady state, and it is important to check if that is in fact the case. In figure 4.2 we can observe the behavior of the thrust for the isolated rotor over 14 revolutions. Right at the start, the value jumps to a maximum since no wake and thus no inflow is present, then it rapidly decreases to a minimum as the starting vortices and the first tip vortices are released into the field and remain close to the rotor disc. As those vortices are convected down and the classical helicoidal shape and the restriction of the wake is achieved, the thrust increases again and then settles to a steady value.

The shape of a hovering rotor wake is fundamentally determined by the self and mutually induced velocities of the vortex filaments, which being material lines, as per the Helmholtz theorems, are convected in the flow by the resulting velocity field. Core features of the slip-stream wake can however be predicted, via simplifying assumptions, through basic momentum theory: namely the contraction of the wake, thus the inboard movement of the tip vortices, is required to satisfy the momentum balance equation applied to the air mass, and is observable in figure 4.3. The wake visualization is also an important step to assure that the simulation is giving physical results.

In figure 4.4 we find the thrust line plots over the last rotor revolution, for each of the testcases, together with the computed moving average. All the cases involving two rotors were simulated for 16 revolutions, 2 more than the single rotor case, to achieve an acceptably steady oscillation of the thrust value. This thrust oscillation is caused both by the mutual aerodynamic interactions between near rotor blades and by the alteration of the induced inflow due to the two wakes mixing.¹⁶ In figure 4.5 we can see a contour plot of the normal force over the rotor discs for testcase (c), in which the load on the isolated propeller has been subtracted to highlight the differences caused by aerodynamic interactions. The oscillation presents two peaks and two valleys, this is explained by the fact that each of the two blades during one revolution goes through a more loaded region of the disc and a less loaded one. In particular, the blades experience lighter loading as they go through the inner region of accentuated up-wash.¹⁶

For the same testcase the free-wake is also shown in figure 4.6. We can see that the wake is skewed towards the right rotor: this causes additional induced flow on it and thus a difference on the mean thrust which is slightly lower for the right rotor in this particular test case, as represented in plot 4.4c. The positioning of the wake in the field is not predictable and changes in time, although it does seem

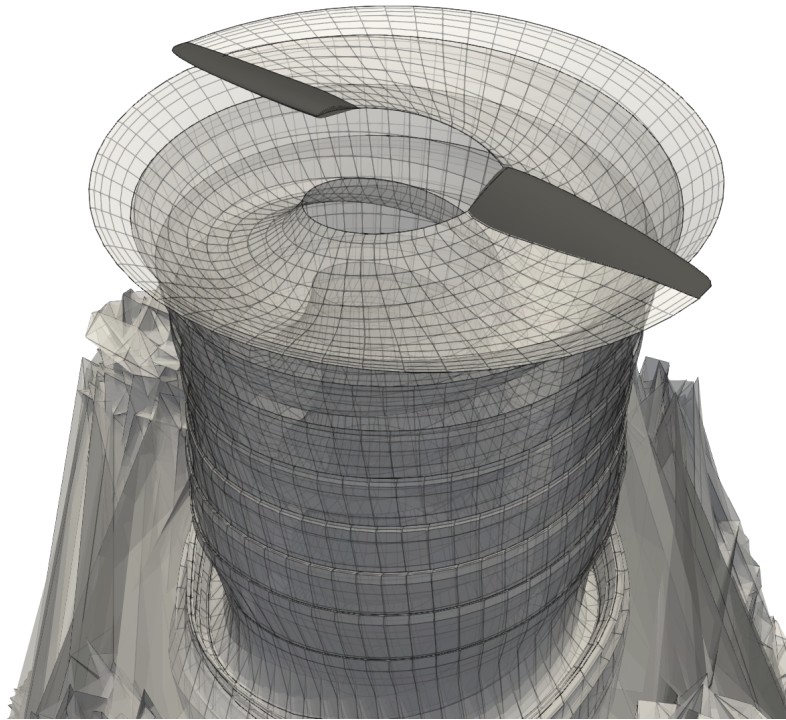


Figure 4.3: Snapshot of the developed wake from the isolated single rotor, at the last time step. Rotor blades are colored in dark grey. The grid lines delimit wake panels, which are slightly transparent to show the internal shape of the wake. We can observe the wake restriction which happens just below the rotor plane.

to stay symmetric for synchronized rotors.

The measured values of mean thrust are reported in table 4.4. The simulation results are averaged over the last rotation. A general practice when reproducing experimental results with free-wake panel codes is to trim the simulation to the measured rotor thrust by either adjusting the vortex core radius or the collective pitch angle of the blades (see Yin,²¹ section 3.3). The dimension of the vortex core used for wake modeling affects the average induced flow on the rotor and thus the mean thrust value, by changing the effective angle of attack of blade elements. The same effect is obtained geometrically by varying the pitch. In the current validation, the vortex core was kept at a value that ensured reasonable wake stability. Since the relevant acoustic results were correctly captured, it was decided not to chase the perfect agreement of the average thrust by altering the core radius or the rotor geometry.

4.2.2 Polar distribution of the overall sound pressure level

As said, the main result of the experiments were the polar plots of the sound pressure level over two elevations of the hemisphere, they are collected in figure 4.7 and 4.8. The simulation results closely match the experimental data, as can be seen. The measurements taken out of the rotors' plane, at -45° , present the largest discrepancy, see figures 4.8e and 4.8f. Higher scatter is present in the measurements over this region, as evidenced in the article. The region under the rotors is dominated by the loading noise, which radiates mainly out of plane, contrary to thickness noise sources which emit in the plane. During hovering, thickness noise is the major source and we find that SPL levels get lower as we go down the hemisphere, but this changes quickly when transitioning to forward flight.

As expected, sound radiation from the hovering, isolated propeller is uniform over the azimuth, as depicted in 4.7a and 4.8a. It is maximum in the rotor's plane and diminishes under it, as discussed

4. Validation of the method with experimental data

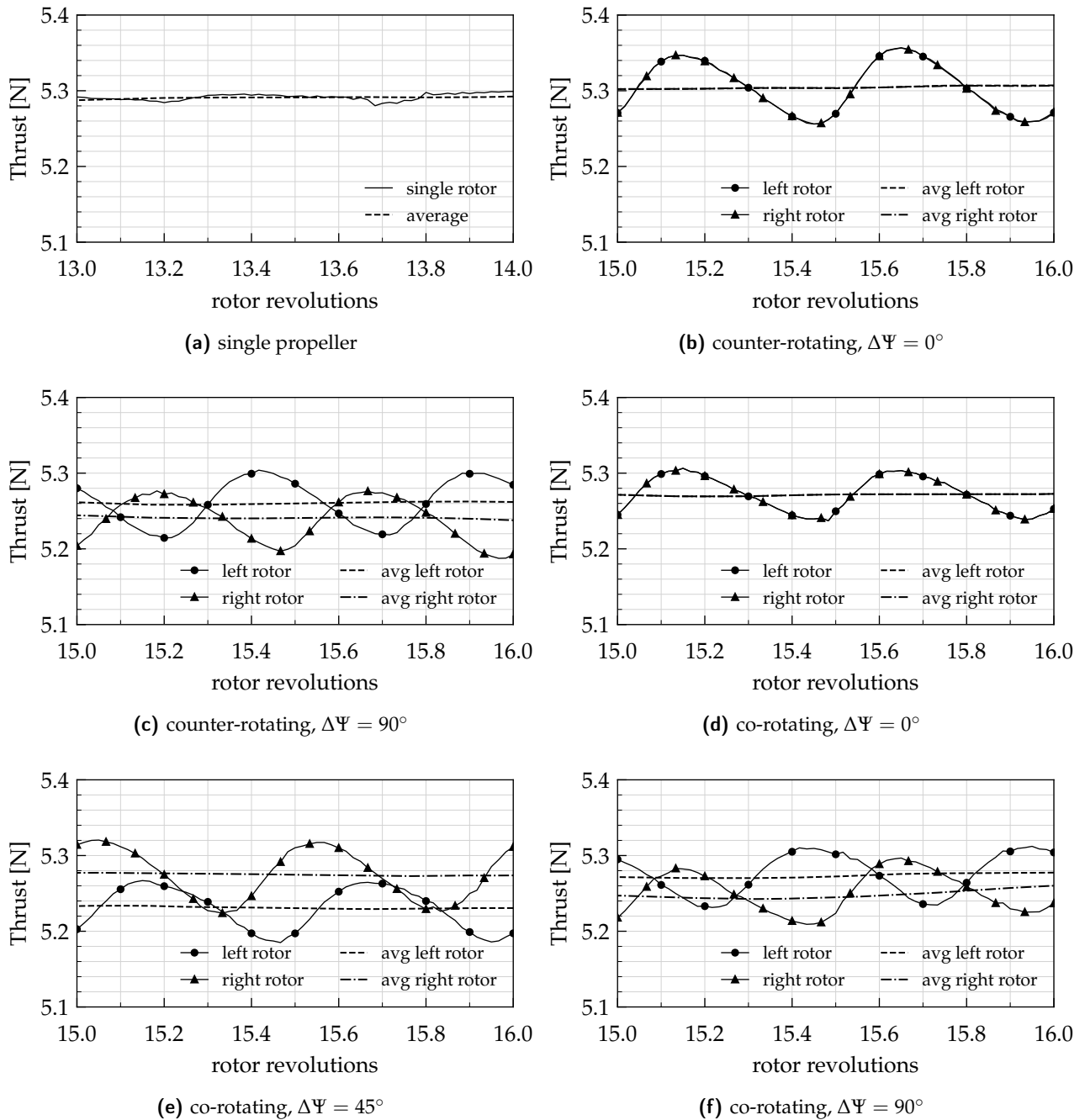


Figure 4.4: Thrust time-series for the last revolution as calculated by UPM and the corresponding moving averages, for each of the test cases of the double rotor experiment.

4. Validation of the method with experimental data

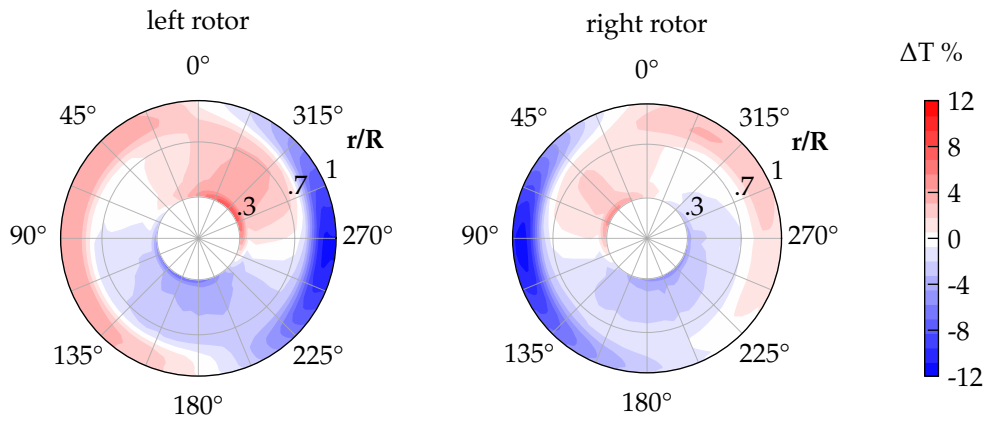


Figure 4.5: Rotor disc contour plot for testcase (c) of percentage thrust difference between side by side rotors and the isolated one. The rotors are counter-rotating with a phase difference $\Delta\Psi = 90^\circ$, the left rotor is counter-clockwise while the right one is clockwise.



Figure 4.6: Snapshot of the developed wake from the two side by side counter-rotating rotors with phase shift $\Delta\Psi = 90^\circ$, at the last time step. Left hand rotor stands on the left. Rotor blades are colored in dark grey. The grid lines delimit wake panels, which are slightly transparent to show the internal shape of the wake. We note the asymmetry of the far wake, which is skewed towards the right rotor, causing increased inflow and a smaller average thrust.

4. Validation of the method with experimental data

Table 4.4: Mean thrust values [N], comparison between NASA experimental values⁶ and numerical simulation results. Load cell bias uncertainty is ± 0.2 N.

Configuration	experimental	numerical (UPM)
single propeller	4.9	5.3
counter-rotating, $\Delta\Psi = 0^\circ$	9.3	10.6
counter-rotating, $\Delta\Psi = 90^\circ$	9.8	10.5
co-rotating, $\Delta\Psi = 0^\circ$	10.0	10.6
co-rotating, $\Delta\Psi = 45^\circ$	10.0	10.5
co-rotating, $\Delta\Psi = 90^\circ$	10.0	10.5

above. The radiation in-plane is similar to that of a still monopole source.^a

When two rotors are corotating in phase ($\Delta\Psi = 0^\circ$, figures 4.7d, 4.8d) they also emit as a still monopole (in-plane) with an SPL increase of nearly 6dB, which would be the theoretical difference for two coincident in-phase monopoles. This is due to the compactness of the sound source, in this case the two rotors, which allows for sound waves to be nearly in-phase for all emission angles. The greater SPL reduction averaged around the azimuth is obtained when the phase shift is set at 90° for the corotating propellers, creating an 8-shaped emission pattern which resembles the one of a still dipole, see 4.7f and 4.8f. We remind that a dipole source is obtained superimposing a monopole with another one of equal intensity but completely out of phase^a.

In the case of counter-rotating rotors, the distance between propeller blades, and thus of sound sources, is constantly modulated during one rotation. A different pattern is created with local maxima, where sound waves are in-sync and thus form constructive interference, and local minima, where sound waves nearly perfectly cancel out due to destructive interference. The resulting sound directivity forms a characteristic quadruple lobe shape^a, as can be seen in figure 4.7b, 4.7c, 4.8b and 4.8c. Those lobes can apparently be rotated, up to a certain amount, by tuning the phase shift, without affecting much their shape or amplitude. This was the first inspiration to the work presented in this thesis, raising the question of whether it was possible, and to what extent, to exploit this directional control with more rotors in real flight maneuvers.

4.2.3 Radiated sound power

The calculation of the total sound power radiated through the hemisphere was performed, as described in section 4.1.2, multiplying the local value of the sound intensity by the corresponding element area and summing the results. However measurements were only taken down to -45° from the rotors' plane thus resulting in an incomplete hemisphere. Numerical simulations were instead performed for all elevation angles. To ensure that data was comparable the sound power value was normalized w.r.t. double the one of the isolated rotor, obtaining a difference of sound power level as seen below:

$$\Delta PWL = 10 \log \left(\frac{P}{2P_{single}} \right) [\text{dB}]$$

A positive value means an increase of radiated sound power with respect to an unsynchronized double propeller configuration, a negative value on the contrary means that a reduction has been achieved, a value of 0 represents no change. Results are reported in table 4.5.

Due to the way the data is normalized, the single rotor value is -3dB , or 3dB under the baseline, since the radiated power is exactly half of the reference. The counter-rotating case does not cause

^a See Rienstra and Hirschberg⁵ for an in depth discussion on the radiation pattern of acoustic sources.

4. Validation of the method with experimental data

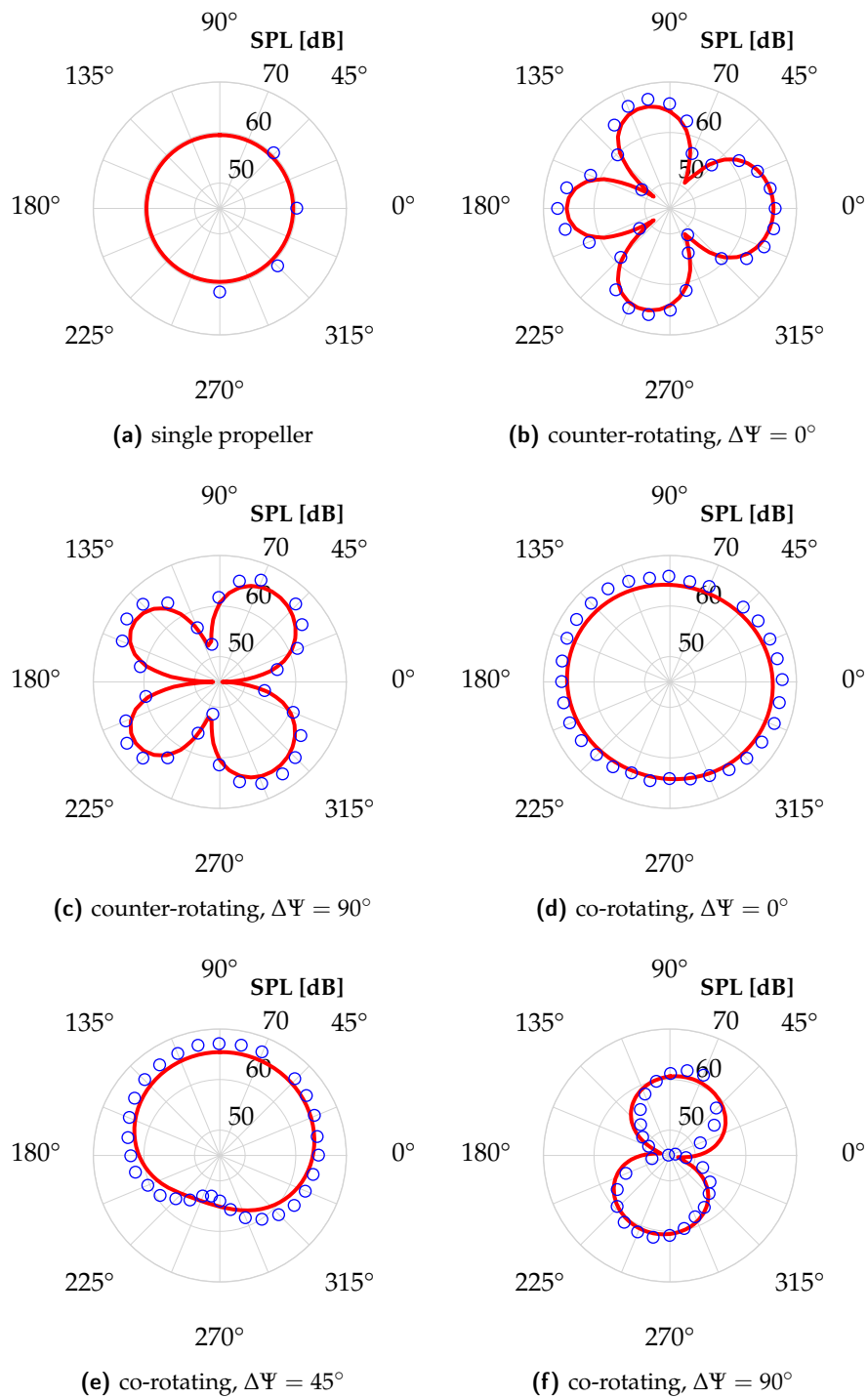


Figure 4.7: Sound pressure level in [dB], plotted as a polar line against the azimuthal angle, at an elevation angle of 0° thus on the rotors plane. The values predicted by the numerical simulation (solid red line) are compared to the experimental data (blue circles, NASA⁶) for each of the test cases.

4. Validation of the method with experimental data

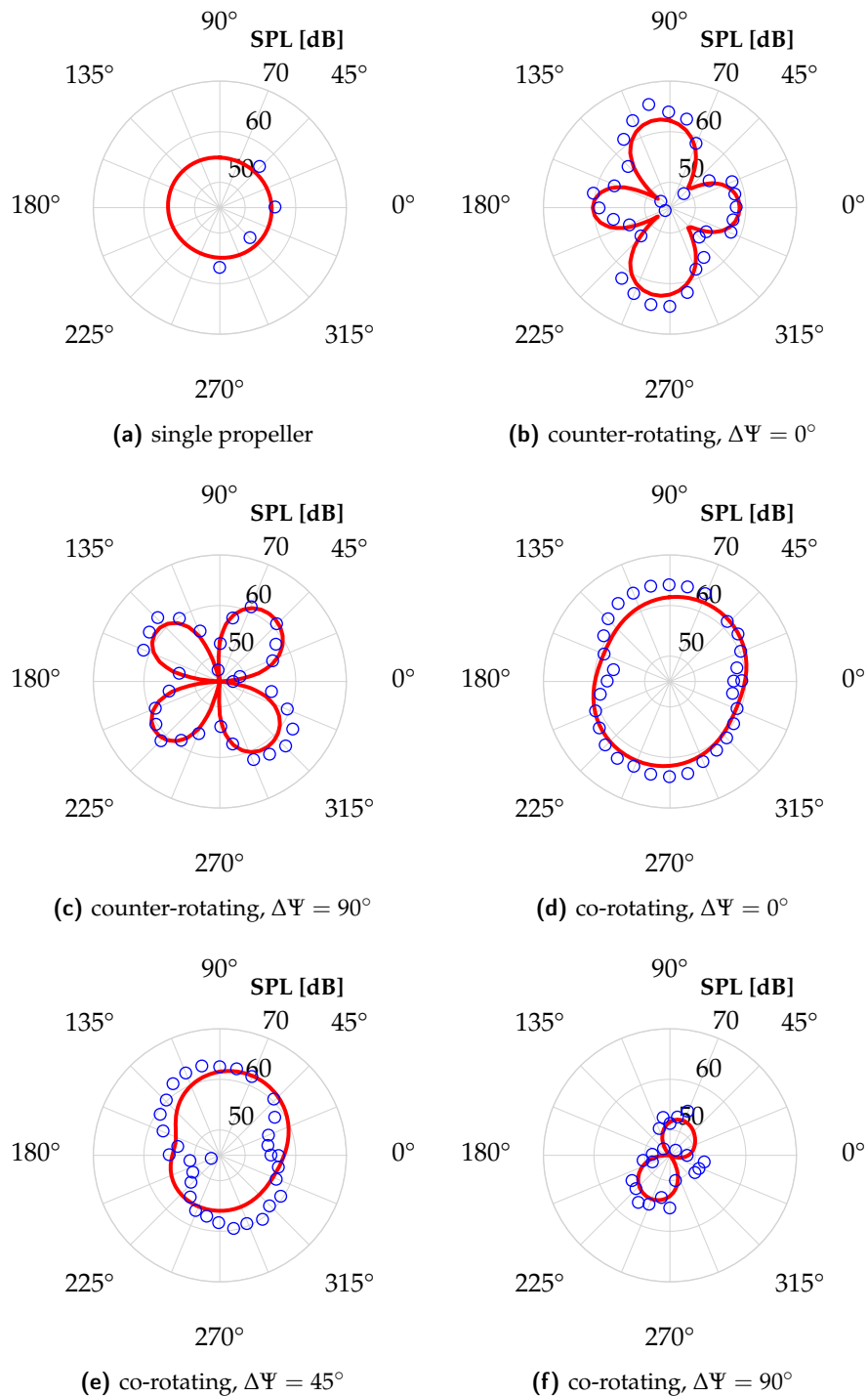


Figure 4.8: Sound pressure level in [dB], plotted as a polar line against the azimuthal angle, at an elevation angle of -45° thus out and under the rotors plane. The values predicted by the numerical simulation (solid red line) are compared to the experimental data (blue circles, NASA⁶) for each of the test cases.

4. Validation of the method with experimental data

Table 4.5: Radiated sound power level [dB] normalized with double the power radiated by single propeller, comparison between NASA experimental values⁶ and numerical simulation results.

Configuration	experimental	numerical (APSIM)
single propeller	-3.0	-3.0
counter-rotating, $\Delta\Psi = 0^\circ$	+0.4	+0.2
counter-rotating, $\Delta\Psi = 90^\circ$	-0.3	+0.1
co-rotating, $\Delta\Psi = 0^\circ$	+2.5	+2.5
co-rotating, $\Delta\Psi = 45^\circ$	-0.2	0.0
co-rotating, $\Delta\Psi = 90^\circ$	-5.8	-5.6

great deviation from the reference, which means that zones where sound is attenuated are balanced by others where it is increased. The co-rotating rotors increase the value by 2.5dB when they are in phase and instead decrease it by almost 6dB when they are shifted by 90° , which means that the sound power was reduced by almost three quarters.

4.3 Effect of compactness ratio on radiated sound power

The mathematical model developed by Schiller as described in section 4.1.3 was used to explore the design space with respect to the problem of minimizing the radiated sound power. The first obvious variable at play is the phase shift $\Delta\Psi$, but the other one needs to be constructed and is the compactness ratio. Let's first define the concept of acoustic compactness.

The Helmholtz number is a dimensionless parameter given by the ratio of the characteristic length scale of an object (a source or obstacle in the sound field) and the acoustic wave length of the problem:

$$H_e \triangleq \frac{l}{\lambda} = \frac{l \cdot k}{2\pi} \quad (4.1)$$

where l is the characteristic length, λ is the wave length and k is the wave number. The Helmholtz number is a measure of the compactness of the source, and we say that a source is compact if it is small compared to unity. A point source by definition would have a value of zero. It is apparent that this definition is dependent on the geometry of the body but also on the frequency considered.

Now we can define a compactness ratio for the problem of the synchronized propellers as the product between the hub to hub distance and the wave number calculated on the BPF: $k \cdot d_{hh}$. This parameter then embeds the effect of not only the separation distance but also the speed and number of blades of the propeller, and makes it easier to draw generalized conclusions on the problem.

The study on the effect of phase shift and compactness ratio on radiated sound power was reproduced in the current work with the simulation toolchain obtaining the same result as in the reference paper. In figure 4.9 we can see two contour plots of the parameter ΔPWL : the one on the left refers to a pair of co-rotating rotors and the one on the right to a counter-rotating pair. The values of phase shift angle were kept at a maximum of 90° , since after that the effective shift is recursive as each rotor has two blades at 180° from one another.

We can observe how the maximum reduction is obtained for the co-rotating pair at 90° of phase shift and the minimum possible value of kd_{hh} . Ideally, the theoretical minimum would be obtained by superposing the two rotors, which would mean to increase the number of blades from 2 to 4. The resulting propeller would radiate sound less efficiently in the same way a dipole does with respect to an acoustic monopole. It is also interesting to note that for the same phase shift angle, varying the compactness ratio can result in either increasing or decreasing the sound power. Since the product kd_{hh}

4. Validation of the method with experimental data

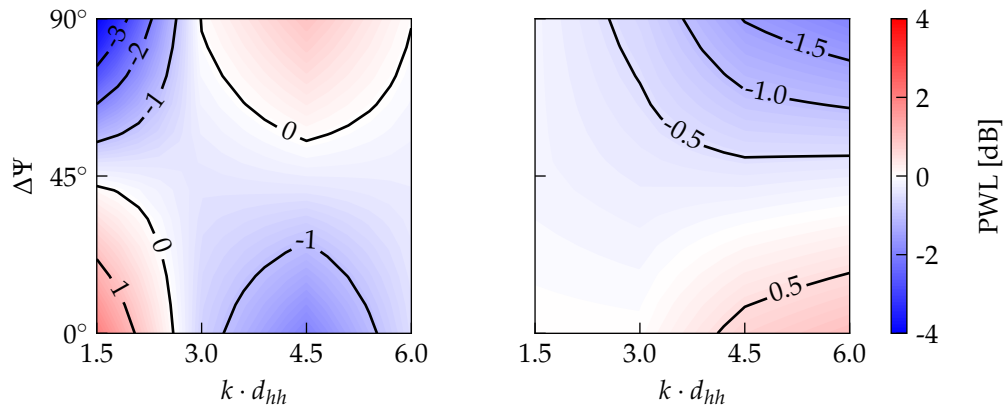


Figure 4.9: Sound power level contours for a pair of co-rotating rotors (left) and counter-rotating (right). The sound power level is calculated as the logarithmic ratio between the double rotor sound power and two times the value for a single rotor. The variable space is given by the phase shift angle in degrees on the y axis and the compactness ratio (wave number times the hub separation distance) on the x axis.

varies with the acoustic frequency considered, it is possible that some multiples of the blade passing frequency would actually be enhanced while only the first harmonic, albeit the most important, is silenced.

Results for the counter-rotating configuration are quite different. The maximum possible reduction in sound power is less than for co-rotating rotors, and location of maxima and minima are different. This suggests that a different physical mechanism is involved. We can note non the less, that for the value of kd considered of 1.2, there is little change in emitted power but the directionality of emitted noise is still greatly affected as we saw from the polar plots. This was also investigated by Pascioni.⁷ For this reason, the optimum value of kd_{hh} for directional sound cancellation of counter-rotating rotors was not investigated further in this thesis work, but it would certainly be an interesting development.

5 | Results of phase shifting for directional noise reduction in forward flight

This chapter presents and discusses the main findings of this research. The simulation methodology described in chapter 3 was applied to the quad-rotor and hexa-rotor configurations under trimmed level forward flight conditions. The aim was to adjust rotor phase angles to control the noise footprint and achieve local minima in the overall sound pressure level within targeted ground regions. As outlined in section 3.4, the optimization problem was formulated with the average SPL in specified regions as the objective function, and the rotor phase angles as the variable space.

The optimized phase angles were the input for the complete aeroacoustic simulation. The trimmed flight condition and the simulation parameters for both the quad-rotor and the hexa-rotor are reported in table 5.1. The wake in forward flight was restricted to a length of 2 rotor diameters behind the vehicle, under the hypothesis of it being of negligible influence at that distance. The simulation setting is as explained in section 3.3. In what follows we present and discuss the results from the acoustic simulations. To avoid overcomplicating the discussion, data from the free-wake aerodynamic simulations are not included in this chapter and are provided in appendix A.1.

5.1 Source directivity and noise carpets

In figure 5.2 we see the ground noise contours for different optimization regions, together with the estimated unsynchronized case (see section 3.1.3 for the computation of the reference acoustic emission), for both the quad-rotor and the hexa-rotor. The zones of the ground plane considered, highlighted in red, are circular sectors centered with the orthogonal projection of the vehicle, with

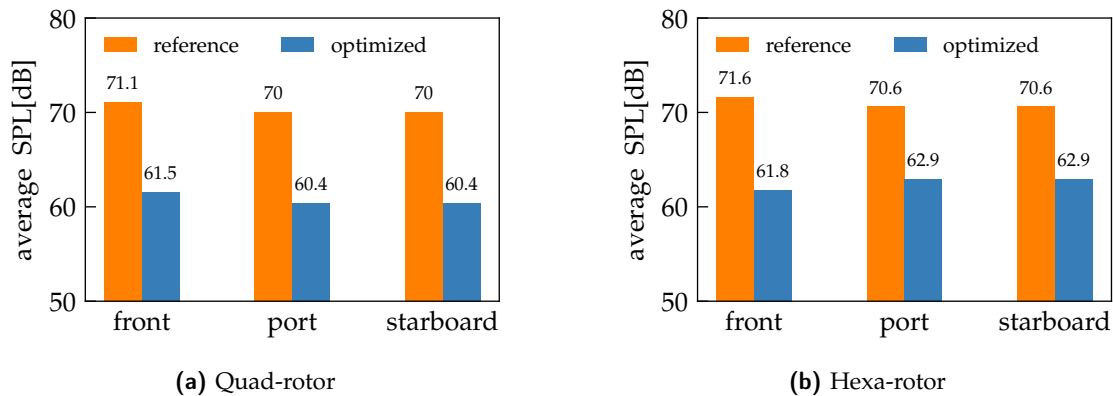


Figure 5.1: Comparison of the average noise level calculated over the considered ground regions between the reference and the result of optimized phase shifting.

5. Results of phase shifting for directional noise reduction in forward flight

Table 5.1: Parameters for the flyover test case. The collective angle is relative to the preset geometric twist. Attitude pitch angle is positive nose up.

flight parameters		
flight condition	level forward flight	
$ T\vec{A}S $	28.33m/s	
advance ratio μ	0.23	
tip Mach number M_t	0.43	
environment	150mISA + 23°C	
UPM parameters		
time step size	2°	
number of revolutions	12	
vortex core radius	0.8 · c_{75}	
wake size	restricted	
trim parameters	quad-rotor	hexa-rotor
attitude pitch angle	-9.3°	-12.1°
rotor collective angles θ_0 [deg]	[1.0, 2.5, 2.5, 1.0]	[2.1, 2.5, 2.9, 2.9, 2.5, 2.1]
mean rotor thrust [N]	[742.4, 777.6, 774.0, 743.3]	[751.1, 772.5, 760.8, 761.6, 772.7, 750.9]

Table 5.2: Radiated sound power level [dB] on the hemispherical microphone grid, normalized with the power corresponding to the unsynchronised reference, for each of the optimization cases.

Sound Power Level: $PWL = 10 \log (P / P_{ref})$ [dB]		
	quad-rotor	hexa-rotor
front	-0.16	-0.93
port	-1.49	+0.78
starboard	-1.49	+0.82

a radius of 200m and spanning through a range of 40°. Considering our usual convention for the azimuth angle being 0 on the x axis and positive counterclockwise from above, the front region goes from -20° to 20°, the port (left) region from 70° to 110° and the starboard (right) region from -70° to -110°. The vehicle flight direction goes from left to right, in the positive x axis direction.

We must remind that, as explained in the methodology, the optimization procedure analyzes only the specified set of observers and not the entire plane. While the objective function:

$$\min \left(\frac{1}{N_{obs}} \sum_{i=1}^{N_{obs}} SPL_i \right) \quad (5.1)$$

potentially describes an absolute minimum with respect to the variable space given by the phase angles, the mean value of SPL in the minimized region may only be a local minimum of the entire observation plane.

The noise carpets indicate how the optimization algorithm succeeded in finding the relative phase shift angles which would steer noise away from the specified region. Those are indicated on top of

5. Results of phase shifting for directional noise reduction in forward flight

Table 5.3: Calculated values of SPL [dB] and radiated sound power [W] on the hemispherical microphone grid in the flyover test case for the reference unsynchronized test and for the optimized case for each considered ground zone.

Quad-rotor				
	reference	front	port	starboard
max SPL	94.8	95.2	96	96
min SPL	73.0	73.2	62.3	62.3
average SPL	89.4	89.0	86.2	86.2
sound power [W]	1.298	1.250	0.920	0.922
Hexa-rotor				
	reference	front	port	starboard
max SPL	95.4	96.8	99.9	99.9
min SPL	78.3	69.5	74.5	74.6
average SPL	90.3	87.0	88.1	88.1
sound power [W]	1.595	1.293	1.916	1.934

each contour plot and comply with the convention explained in section 3.1.2. We can observe that the baseline noise carpet is similar for the two configurations, both with respect to the directivity (hexarotor footprint is a bit more expanded) and to the absolute SPL levels. The noise is concentrated slightly in front of the vehicle and is symmetrical about the flight direction, due to the symmetry in the rotors configuration. It is important to remind that vehicle weight was scaled so that each rotor has similar loading between configurations. One would thus reasonably assume that the hexa-rotor would be noisier due to the presence of two more equivalent sound sources, and while this is not evident from the ground contour, it is clear from the SPL and radiated sound power values on the hemisphere, as shown in table 5.3.

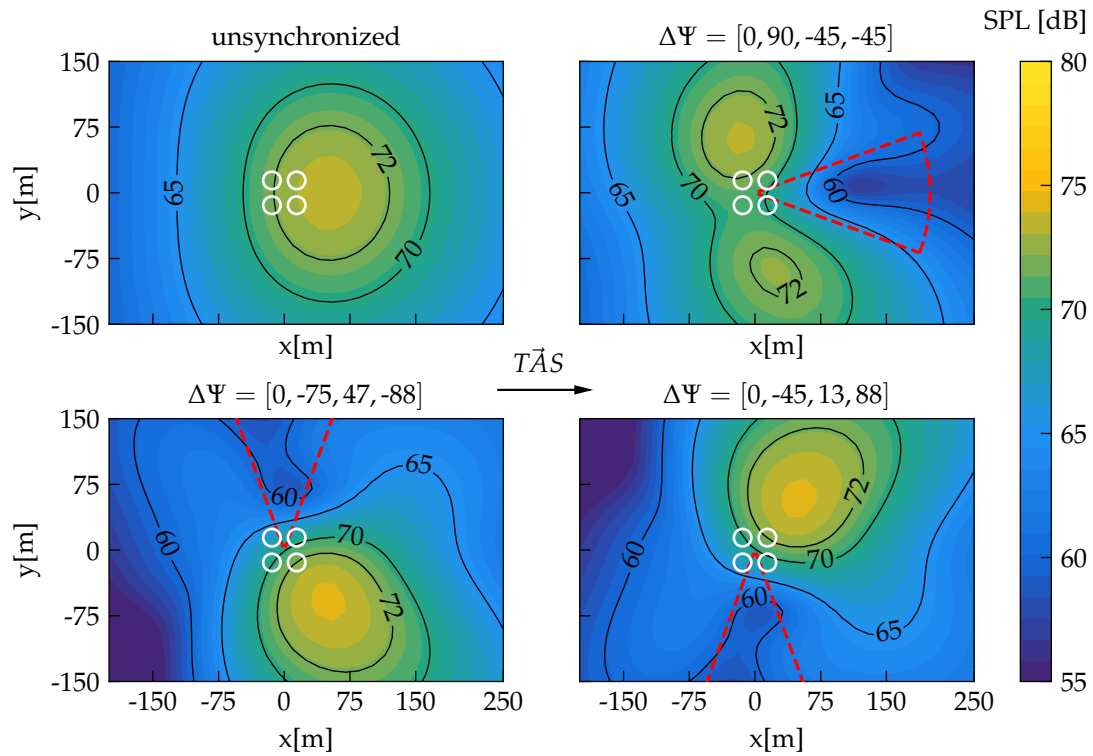
The front optimization for the quad-rotor produced two-lobes of high noise level right at the sides of the vehicle, while reducing it for basically the whole right side of the plane, and not only for the specified region delimited in red. The side optimization instead moved the single concentration spot away from either the port or starboard side. We can note how the contours for those two cases look flipped around the x axis with respect to one another. In fact, the optimized phases are exactly mirrored between the two cases, producing in turn a mirrored noise carpet. This symmetry property will be further discussed in a following section.

Looking at the hexa-rotor case, the optimization of the frontal region created four lobes of noise concentration on the ground, two stronger ones at the back and the other weaker two in the front, at the sides of the prescribed noise minimization zone. A stronger reduction is also obtained right under the vehicle with respect to the quad-rotor case. The side optimization produces results similar to the quad-rotor, steering noise away from the interest region where a local minimum appears, but in this case it also produces a strong constructive interference in the front increasing considerably the maximum SPL value.

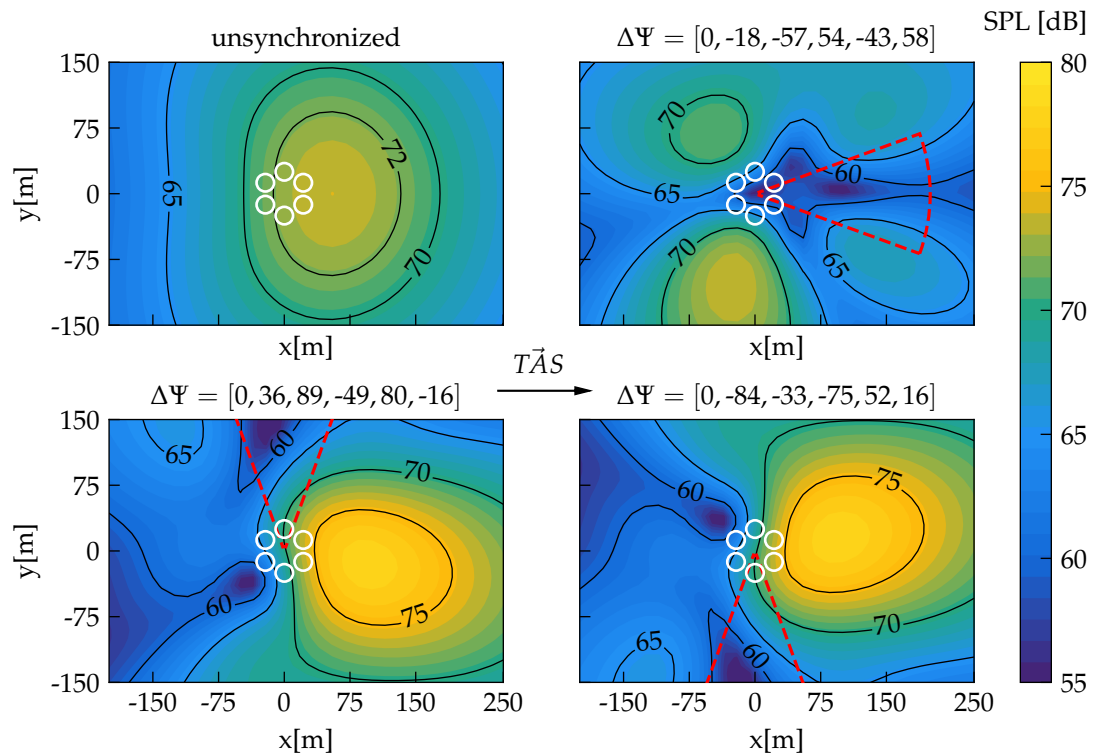
The bar chart in figure 5.1 shows the difference in the average value of SPL in the considered ground regions for the reference (no synchronization) case and the optimized one. A reduction of around 10dB is achieved in all cases.

From figures 5.3 and 5.4 we can have a better understanding of the sound directivity. They depict, for the quad-rotor and hexa-rotor respectively, the SPL polars over the hemisphere measurement

5. Results of phase shifting for directional noise reduction in forward flight



(a) Noise footprint of the quad-rotor



(b) Noise footprint of the hexa-rotor

Figure 5.2: Contours of the SPL over the ground plane for the reference case with unsynchronized rotors, and for test cases conducted with optimized rotor phases to obtain a minimum of SPL over the specified ground zone, which is highlighted with a dotted red line. The white circles indicate the rotors positions and are not to scale. The vehicle flight direction goes from left to right, in the positive x axis direction.

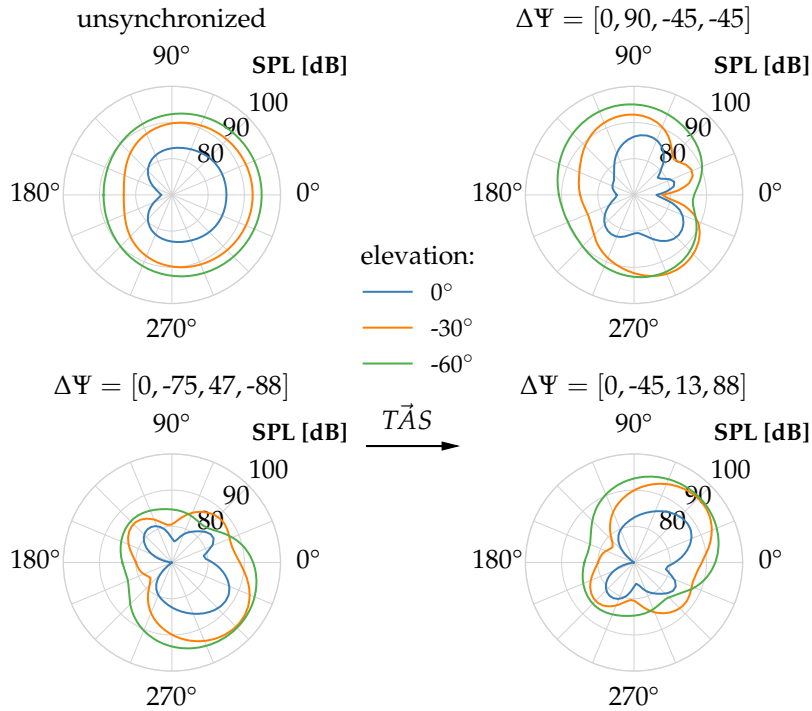


Figure 5.3: Polar SPL directivity of the quad-rotor. Values of the SPL on the hemispherical microphone grid are plotted as polar lines against the azimuthal angle, for different elevation angles from the rotors plane. A value of 0° reports the in-plane noise, while negative values indicate out of plane measurements under the rotors.

surface around the azimuth and for different elevations from the rotors plane. A value of 0° reports the in-plane noise, while negative values indicate out of plane measurements under the rotors. To aid in understanding how the directivity at different elevations affects the ground noise carpet, consider that sound waves propagate radially from the source and elevations of -30° and -60° correspond to ground locations distant respectively 260m and 86m from the vehicle projection.

The higher SPL levels out of plane indicate that the loading noise sources become predominant in forward flight, as would be expected. For the quad-rotor, we can then observe how the trend in directivity is generally preserved between the in-plane and out-of-plane measurements, but the achieved reduction of sound levels decreases for the loading noise. This would indicate that the forward flight velocity, which affects the directivity of loading noise, is partly diminishing the effect of phase shifting, as also shown by Smith.¹¹ Looking at the hexa-rotor, we notice a slightly different behavior. The position of valleys in the SPL level around the azimuth sensibly changes between elevation levels, but the minimum values of SPL are now of comparable magnitude between the in-plane and out-of-plane measurements.

5.2 Pressure time series and frequency spectra

In figures 5.5 and 5.6 we find a deeper analysis on acoustics for the quad-rotor simulation. For the front and port side ground region optimization cases, two observer positions were selected at points of local maximum and minimum of the SPL on the ground plane. At those locations, the acoustic spectrum and the pressure fluctuations time series were extracted and shown in the figures. The same procedure was done in figures 5.7 and 5.8 for the hexa-rotor.

5. Results of phase shifting for directional noise reduction in forward flight

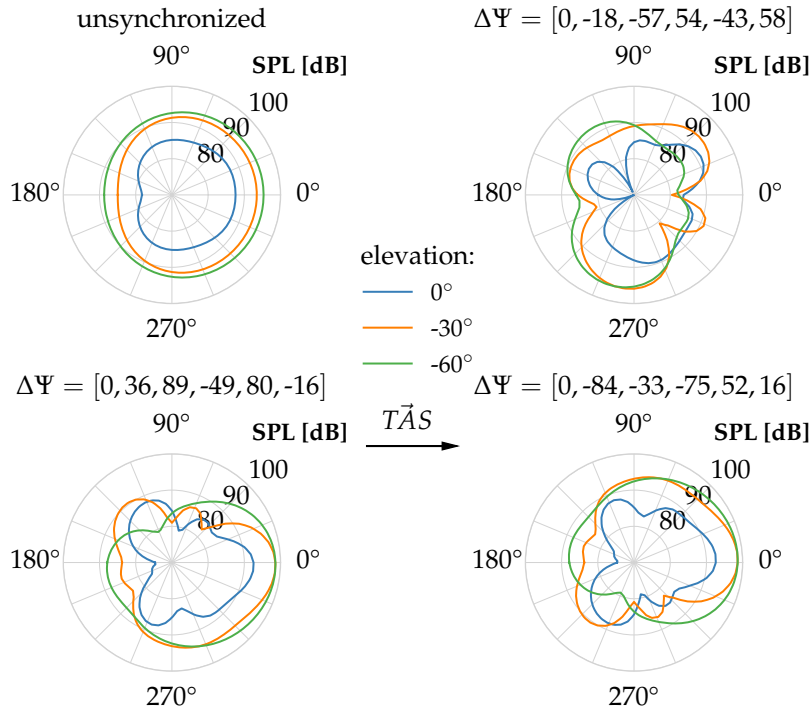


Figure 5.4: Polar SPL directivity of the hexa-rotor. Values of the SPL on the hemispherical microphone grid are plotted as polar lines against the azimuthal angle, for different elevation angles from the rotors plane. A value of 0° reports the in-plane noise, while negative values indicate out of plane measurements under the rotors.

Let us look first at the acoustic spectra. It is important to remind that in the simulations performed in this work only tonal sources of noise, namely the thickness and loading noise of the blades, were captured and no estimation of the broadband component was done. Thus, the acoustic spectrum shows the SPL contribution of narrow bands of frequency corresponding to integer and half-integer multiples of the blade passing frequency. As expected, the strongest component in all spectra corresponds to the BPF, followed by its first few multiples. After that, the sound pressure level decreases initially fast and then more slowly as it approaches higher frequencies. The main contribution to tonal noise in forward flight is given by periodic unsteady loading events, which are caused primarily by the dissymmetry of lift, and secondly by rotor to wake interference. Those events cause the change in pattern of the spectrum from the hovering case.

The estimated spectrum corresponding to a configuration of unsynchronized rotors, or better in which the relative phase is random, is calculated by summing the pressure fluctuations of each of the rotors in frequency domain, and serves as a baseline. We notice by comparing to the baseline that the phase optimization has its largest influence on the first three multiples of the BPF, decreasing the corresponding values on microphone 2 in all cases. For the hexa-rotor, in figure 5.7, some higher frequencies are apparently enhanced in the minimization zone. The absolute values are still low (under 40dB), but the relative increase is not negligible.

Finally, in the spectrum plots we also find the A-weighting curve, which represents a common correction applied in acoustics to highlight frequencies to which the human hearing is more sensible. We can see that due to the low blade passing frequency, this type of weighting would render the benefits from phase shifting basically imperceptible. Non the less, the same procedure applied to smaller, faster rotating rotors is expected to bring the same benefits at a higher BPF, which would then be more relevant even under A-weighting.

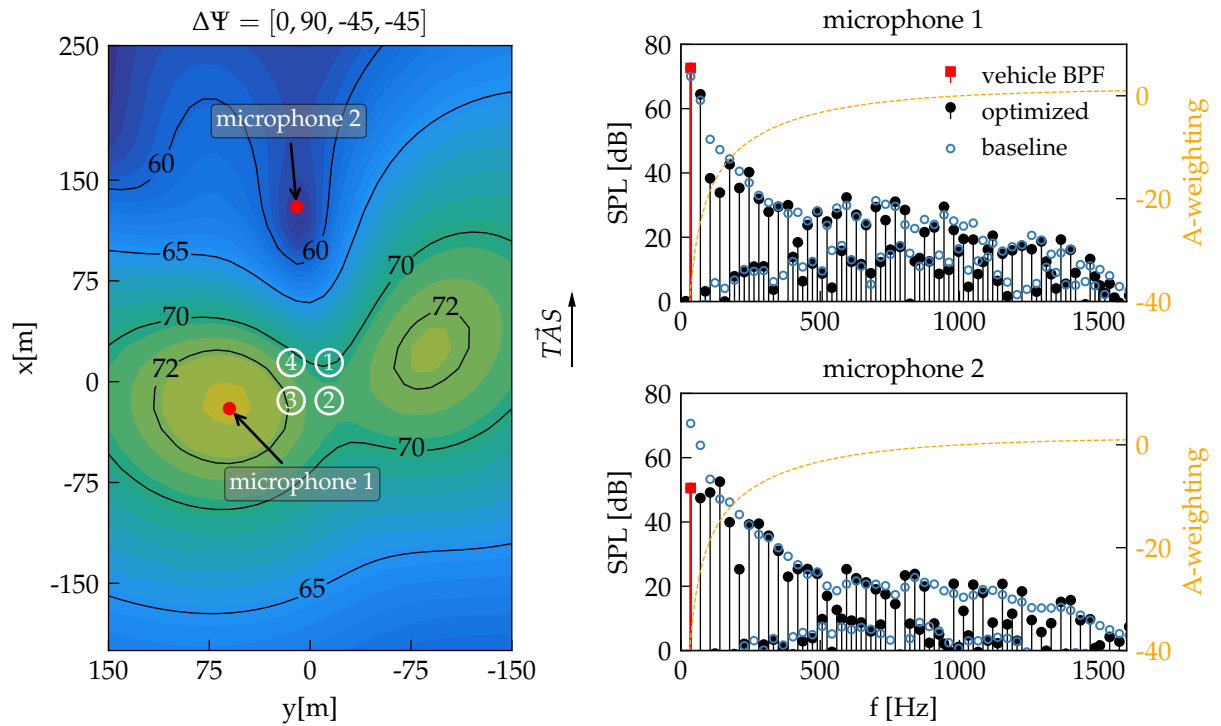
5. Results of phase shifting for directional noise reduction in forward flight

Turning to the pressure fluctuations time series immediately reveals the mechanism behind the phase synchronization method. The plots show the waves generated by each rotor and the resultant wave obtained by coherent summation, over one rotation period. For the points of minimum SPL the pressure waves are out of phase and positive peaks are attenuated by negative ones, generating a coherent sum of smaller amplitude, hereby reducing the rms value. The drawback is that the waves can be in phase in other locations and produce constructive interference increasing the SPL, which is also clearly visible for microphones taken at the highest noise location.

In general, for microphones located in front of the vehicle, the pressure fluctuations are very similar for all rotors and resemble the classic shape given by low frequency unsteady loading harmonic noise. The contribution of the periodic variation of flow velocity for the blade in forward flight is the main factor here. This results in good performance of phase synchronization which is able to exploit the uniformity in wave form between rotors to create near perfect cancellation.

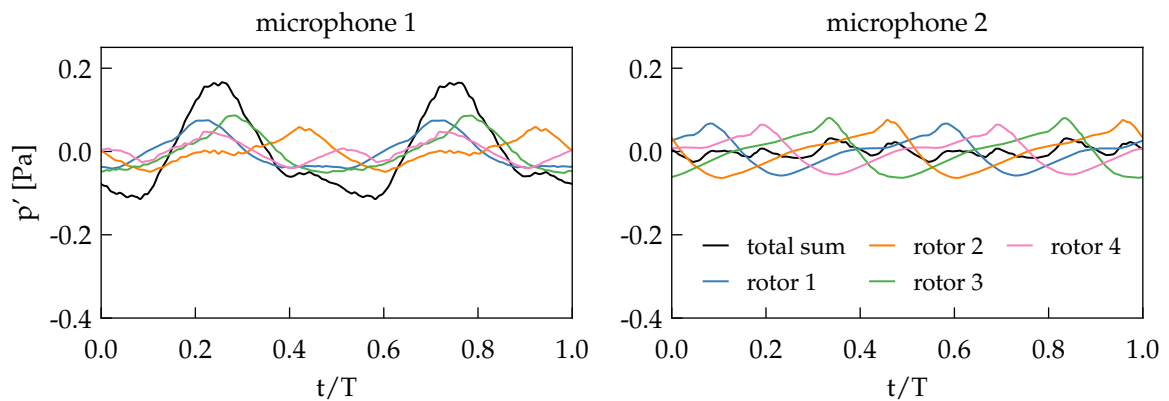
When dealing with observers located on the side of the vehicle instead we note some differences. Looking for example at microphone 2 in figure 5.8, it is evident that rotors 1,3 and 5 contribute with higher amplitudes to the resulting wave. Those are the counterclockwise rotating rotors. We note this behavior for the quad-rotor as well. The cause is probably the fundamental dissimetry in the noise emitted by the single rotor in forward flight with respect to the flight direction. For a rotor with fixed blades (meaning without flapping or cyclic pitching motion) the highest values of SPL is shifted towards port-front side for a counterclockwise rotation and to starboard-front side for a clockwise one. This was noted in the current research and is also shown in the works of Yin²¹ and Kostek.¹⁵ The reason is that the non-flapping blade experiences a peak of loading at around $280 - 290^\circ$ (0° in front) and thus the direction of maximum Doppler amplification points towards the port-front side (see chapter 2).

5. Results of phase shifting for directional noise reduction in forward flight



(a) Ground SPL contour. White circles indicate rotor position and number, not to scale. Flight direction bottom-up. Observer points (microphones) indicated in red correspond to maximum and minimum of SPL.

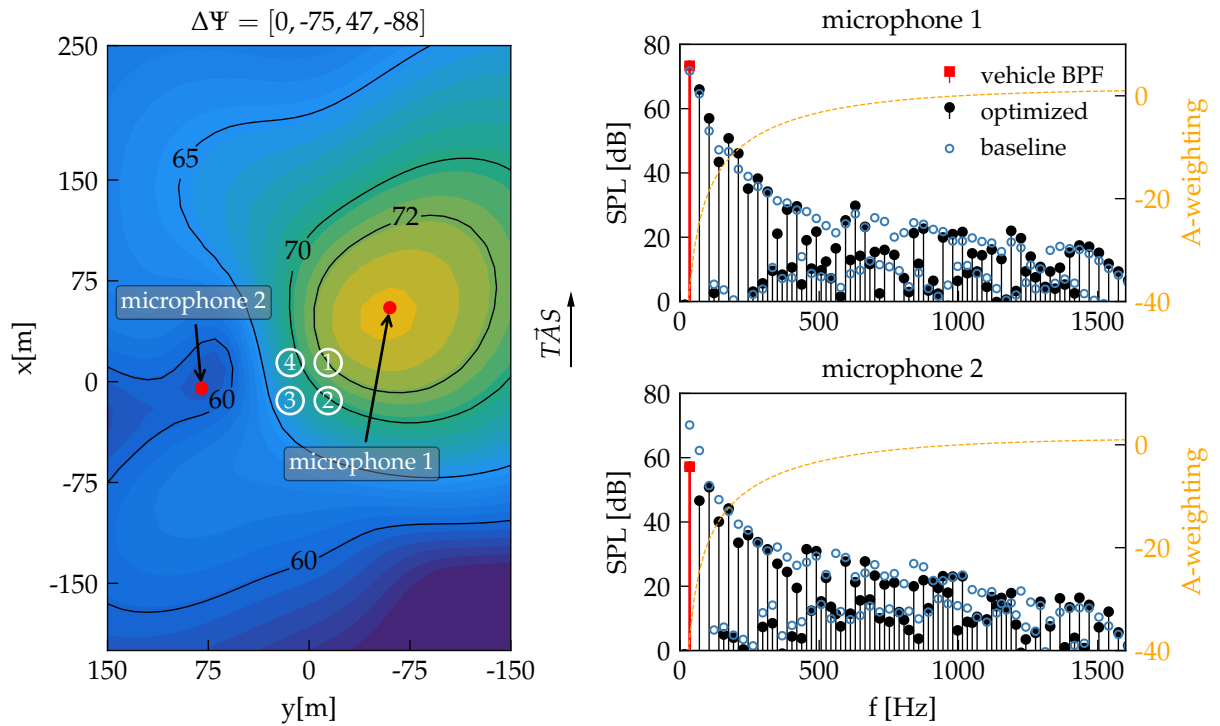
(b) Acoustic frequency spectrum of the total vehicle emission with optimized phase angles and the estimation of the unsynchronized baseline, for the indicated microphone positions. The BPF for optimized phases is highlighted in red. The orange dotted line represents the A-weighting curve.



(c) Acoustic pressure fluctuations over one rotation period of the total vehicle emission and of the isolated emission of each rotor, for the indicated microphone positions.

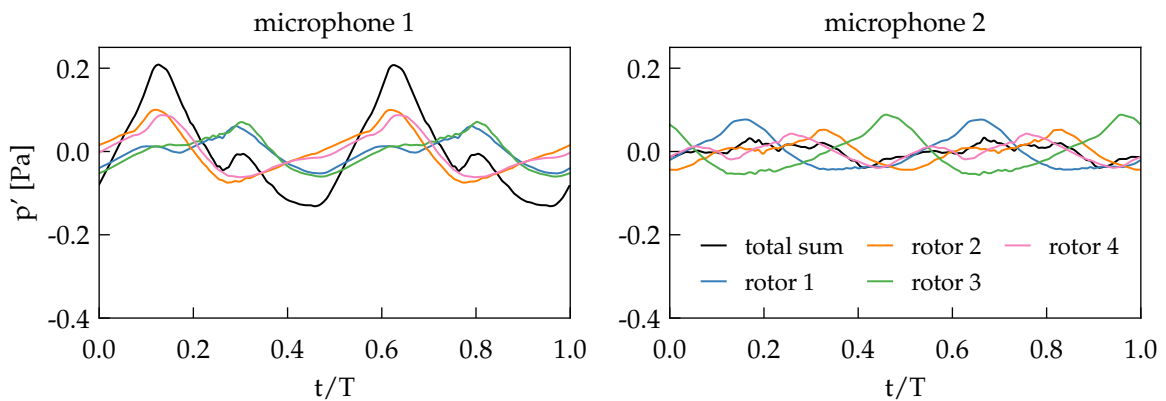
Figure 5.5: Acoustic spectrum and pressure fluctuations over one rotation period at chosen observer locations for the quad-rotor in forward flight with rotor phases optimized to reduce noise in the front ground region. In the ground contour plot are indicated the microphone positions chosen for the analysis. The color scale is consistent with figure 5.2.

5. Results of phase shifting for directional noise reduction in forward flight



(a) Ground SPL contour. White circles indicate rotor position and number, not to scale. Flight direction bottom-up. Observer points (microphones) indicated in red correspond to maximum and minimum of SPL.

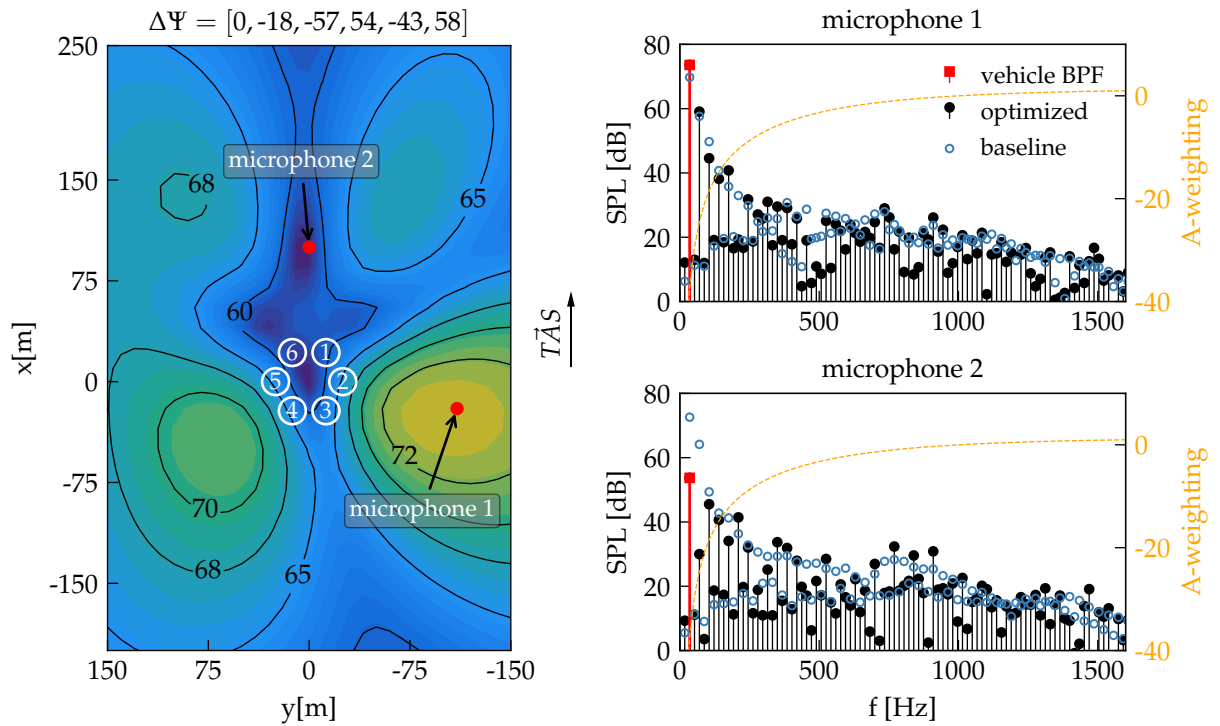
(b) Acoustic frequency spectrum of the total vehicle emission with optimized phase angles and the estimation of the unsynchronized baseline, for the indicated microphone positions. The BPF for optimized phases is highlighted in red. The orange dotted line represents the A-weighting curve.



(c) Acoustic pressure fluctuations time series of the total vehicle emission and of the isolated emission of each rotor, for the indicated microphone positions.

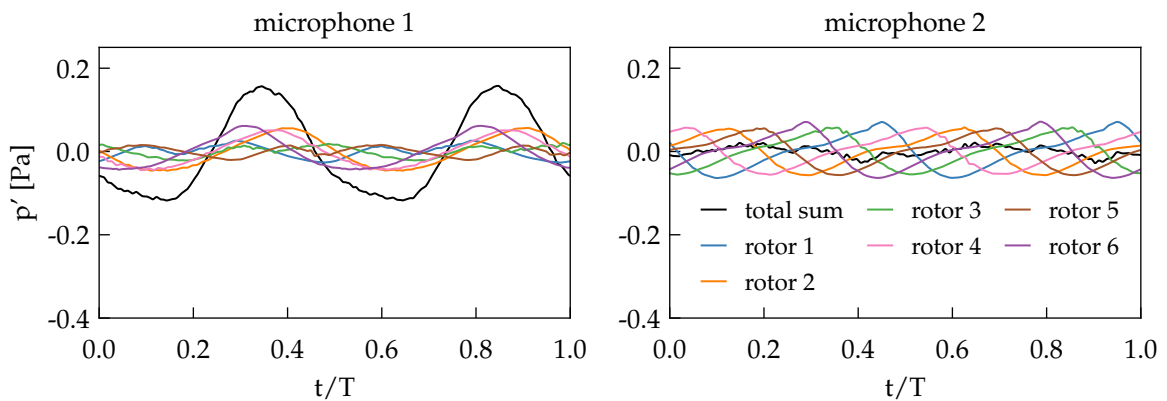
Figure 5.6: Acoustic spectrum and pressure fluctuations over one rotation period at chosen observer locations for the quad-rotor in forward flight with rotor phases optimized to reduce noise in the port side ground region. In the ground contour plot are indicated the microphone positions chosen for the analysis. The color scale is consistent with figure 5.2.

5. Results of phase shifting for directional noise reduction in forward flight



(a) Ground SPL contour. White circles indicate rotor position and number, not to scale. Flight direction bottom-up. Observer points (microphones) indicated in red correspond to maximum and minimum of SPL.

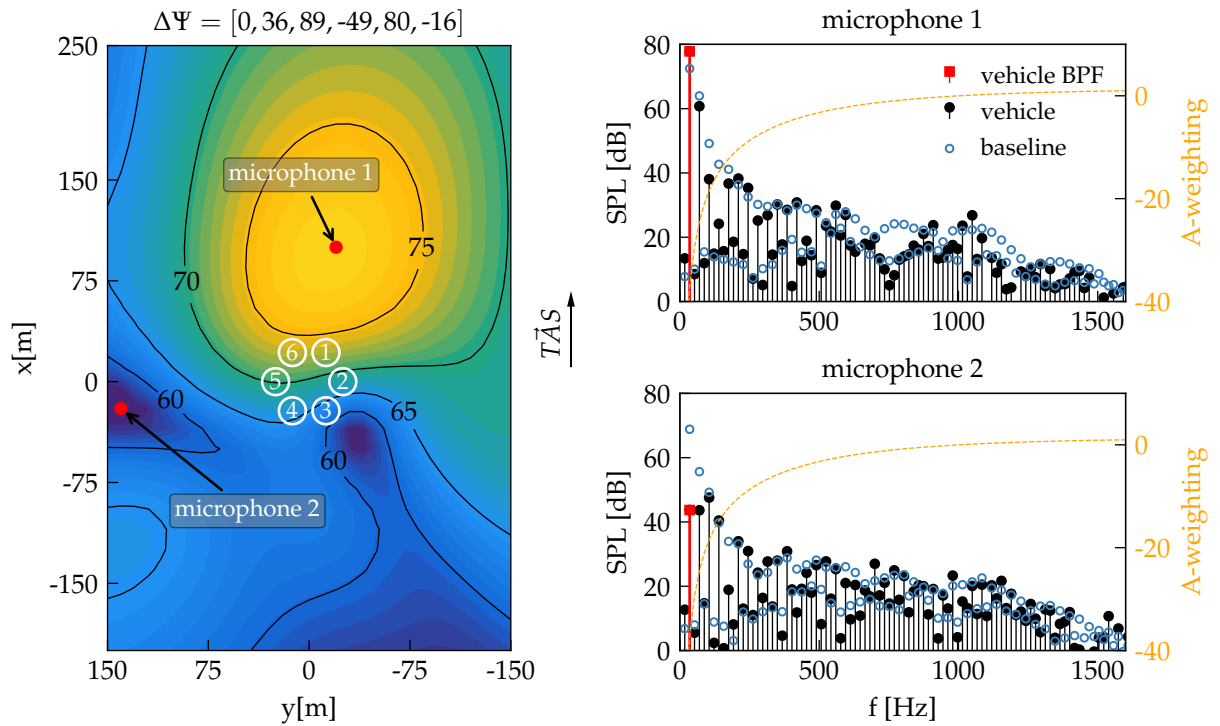
(b) Acoustic frequency spectrum of the total vehicle emission with optimized phase angles and the estimation of the unsynchronized baseline, for the indicated microphone positions. The BPF for optimized phases is highlighted in red. The orange dotted line represents the A-weighting curve.



(c) Acoustic pressure fluctuations over one rotation period of the total vehicle emission and of the isolated emission of each rotor, for the indicated microphone positions.

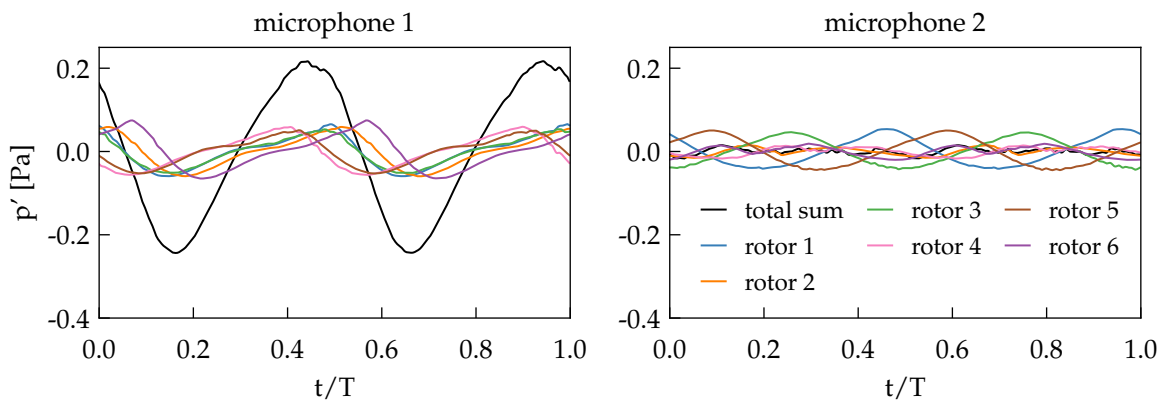
Figure 5.7: Acoustic spectrum and pressure fluctuations over one rotation period at chosen observer locations for the hexa-rotor in forward flight with rotor phases optimized to reduce noise in the front ground region. In the ground contour plot are indicated the microphone positions chosen for the analysis. The color scale is consistent with figure 5.2.

5. Results of phase shifting for directional noise reduction in forward flight



(a) Ground SPL contour. White circles indicate rotor position and number, not to scale. Flight direction bottom-up. Observer points (microphones) indicated in red correspond to maximum and minimum of SPL.

(b) Acoustic frequency spectrum of the total vehicle emission with optimized phase angles and the estimation of the unsynchronized baseline, for the indicated microphone positions. The BPF for optimized phases is highlighted in red. The orange dotted line represents the A-weighting curve.



(c) Acoustic pressure fluctuations time series of the total vehicle emission and of the isolated emission of each rotor, for the indicated microphone positions.

Figure 5.8: Acoustic spectrum and pressure fluctuations over one rotation period at chosen observer locations for the hexa-rotor in forward flight with rotor phases optimized to reduce noise in the port side ground region. In the ground contour plot are indicated the microphone positions chosen for the analysis. The color scale is consistent with figure 5.2.

5.3 Discussion

The obtained results are promising and indicate that rotor phase shifting could be an effective mechanism to obtain directional noise control even in forward flight. Here, we present additional considerations, including discussions of a more speculative nature and ideas for future research developments.

Rotor-wake interactions

First of all, we have to address in some more detail the reason for adopting an advance ratio of 0.23 for the optimization and how it relates to the aerodynamic interactions between rotors and wakes. At lower flight speeds, the vehicle's attitude is more leveled, and the wake from the front rotors is convected very close to the aft ones. A strong interaction between the two rolled-up wakes, which become basically intertwined, causes a strong modification of the inflow on the back rotors, and this affects the acoustic emission pattern, thus invalidating simulations in which this interaction is neglected. For lower flight speeds the optimization would then need to be done employing the complete simulation toolchain, which for the present work was not possible due to time constraints. The author believes non the less that it should be possible to apply the procedure even in those flight conditions, since the modification in acoustic emission of the aft rotors is probably due mainly to the modification of inflow distribution around the azimuth, affecting directivity but not the wave form and thus frequency content of the source. Non the less, additional investigations are required to asses the effect of rotor to wake interaction on noise directivity and phase shifting.

Symmetry properties

Some symmetry properties of phase shifting applied to counter-rotating rotors were observed. A single couple of counter-rotating rotors with either tip-to-tip ($\Delta\Psi = 0^\circ$) or orthogonal ($\Delta\Psi = 90^\circ$) phasing emits sound waves symmetrically w.r.t. the plane between the rotors. Then any configuration involving couples of counter-rotating rotors all in either tip-to-tip or orthogonal phasing will show a symmetric noise emission, and this holds for forward flight if the flight direction lies on the plane of symmetry. A consequence is that for any phase distribution, inverting the values side to side w.r.t. the plane of symmetry causes the sound emission to be mirrored.

Influence of the flight maneuver

One important aspect of the obtained results is the inclusion into the simulation of the trim procedure via blade pitch variation, which made it possible to evaluate the influence of realistic flight conditions on the proposed method. The main factor at play is the variation in loading necessary to achieve the control moments. In forward flight, this effect is modest and as the results demonstrate how it does not pose much of an issue, but during non-symmetric maneuvers, large variations in thrust may be requested and could affect the efficacy of the proposed method.

Localized increase of SPL

The amplification of sound in some zones outside of the one of interest was an anticipated effect, regarded from the beginning as a necessary compromise. However, there could be some margin to reduce this effect by performing a multi-objective optimization, including additional constraints on the radiated power or the maximum SPL level on ground, for example.

Amplification of higher frequencies

Another aspect which was speculated to potentially be a significant side effect of phase shifting was the alteration of higher frequency content in the noise emission. This was not observed to be a relevant effect. As noted, in only one case for the hexa-rotor (figure 5.7) we observed some amplification of higher frequencies, although their amplitude remained negligible. With a different spectrum, with a larger content of high frequencies this effect could become important. Contribution to higher frequencies could come from blade-vortex interaction or unsteady loading related to wake ingestion, and the evaluation of their effect on the phase shift method calls for additional investigations.

Conclusions

In this thesis, the performance of a phase shift method for directional noise reduction was evaluated for quad-rotor and hexa-rotor configurations with collective blade pitch control. A numerical toolchain was developed for the aeroacoustic simulation of parametric multirotor configurations, which operates the unsteady free-wake panel code UPM²⁵ as the aerodynamic solver and uses its output to compute linear sound propagation at the observer locations through the Ffowcs William-Hawkings acoustic solver APSIM.²¹

The simulation toolchain was validated by reproducing the results of a fundamental research on rotor phase shifting conducted by NASA⁶ with fixed-pitch hovering rotors. The polar distribution of sound pressure level measured around a double rotor configuration, for different values of phase shift angle, was correctly predicted by the simulations along with the radiated sound power and the effects of compactness ratio.

Subsequently, the methodology was applied to quad-rotor and hexa-rotor configurations in trimmed level forward flight. Acoustic pressure was computed on a ground plane located 150m below the vehicle. Rotor phase angles were optimized to control the noise footprint and achieve local minima in the overall sound pressure level within designated ground regions. The average sound pressure level (SPL) in these regions was defined as the objective function, while the rotor phase angles formed the variable space. A surrogate-based optimization algorithm³⁵ was employed to determine the rotor phase configurations that steered noise away from regions in front and at the sides of the vehicle.

To reduce computational effort and examine the effect of rotor-to-wake interaction on multirotor sound directivity, a noise prediction approach based on a single-rotor flow solution was developed. This approach was used in the optimization process, and the results of full simulations confirmed that, under certain flight conditions, neglecting aerodynamic interactions introduces negligible error in ground noise predictions.

The simulation results with optimized rotor phase angles were compared with a reference case with unsynchronized rotors, i.e. with random phase, and led to the following findings:

- the noise footprints showed how in all cases, the optimized configurations achieved up to 10dB reduction in average SPL over the targeted ground region from a baseline value of 70dB. While noise was effectively redirected away from critical areas, it became concentrated in other locations. For the hexa-rotor, the maximum SPL increased in some cases.
- the SPL polar distribution over the measurement hemisphere revealed that out-of-plane loading noise dominates in forward flight. For the quad-rotor, the directivity trends were generally consistent between in-plane and out-of-plane measurements, though the achieved noise reduction was less effective for loading noise. In the hexa-rotor case, the positions of SPL valleys varied significantly across different elevation levels, but the minimum SPL values were of comparable magnitude between in-plane and out-of-plane measurements.
- sound spectra and acoustic pressure time series, analyzed at microphones located in the minimization region and at the point of maximum SPL, highlighted how the phase shift method

5. Results of phase shifting for directional noise reduction in forward flight

primarily influenced the blade passing frequency and its first three integer harmonics. A slight amplification of higher frequencies was observed for the hexa-rotor, suggesting that additional studies considering sources of higher-frequency content are necessary to evaluate this effect.

- pressure fluctuation analysis in the front region indicated that the contributions from individual rotors to the resultant wave were similar, with loading symmetry aiding destructive interference. In the side optimization, the asymmetric directivity of rotors in forward flight caused some of them to have a greater influence than others. Overall, achieving noise minimization in side regions proved more challenging than in front regions.

In summary, the phase shift method proved effective in directionally reducing sound levels produced by a multirotor in forward flight, though with certain limitations.

This study also highlights several aspects that warrant further investigation:

- the optimization was performed at a relatively high advance ratio, at which the interaction of the aft rotors with the wake shed by the front ones was negligible. Further analysis is necessary to assess if this method can be employed even when this interaction is strong, thus for small values of forward speed.
- the effect of compactness ratio, proportional to the blade passing frequency and the rotors separation distance, was observed for the double propeller configuration with respect to the radiated sound power. Considering it with respect to noise directivity for a multirotor configuration could lead to interesting results, since an optimum value could exist for maximizing performance of the noise canceling method.
- the effect of non-symmetric and more aggressive maneuvers, causing higher thrust imbalances between rotors and larger collective pitch actuation could affect the distribution of emitted sound and the efficacy of phase shifting. They were not considered in the current study and are surely worth further analysis.
- a natural step following the presented research would certainly be an experimental campaign aimed at reproducing the results obtained numerically, either in the acoustic wind tunnel or with field tests. Experimental validation would both assess the accuracy of the simulation procedure for the specific application and give insights into the practical limitations and weaknesses of the phase shift method.

Bibliography

- [1] J. Katz, A. Plotkin, "Low-speed Aerodynamics: from wing theory to panel methods", *McGraw-Hill*, 1991
- [2] G. Buresti, "Elements of Fluid Dynamics", *Imperial College Press*, 2012
- [3] J.G. Leishman, "Principles of Helicopter Aerodynamics", *Cambridge University Press*, 2006
- [4] J. Delfs, "Lecture notes of Grundlagen der Aeroakustik (Basics of Aeroacoustics)", *Braunschweig Technical University*, a.y. 2022/23
- [5] S.W. Rienstra and A. Hirschberg, "An introduction to acoustics", *Eindhoven University of Technology*, 2017
- [6] N.H. Schiller et Al., "Tonal noise control using rotor phase synchronization", *75th Vertical Flight Society's Annual Forum and Technology display*, 2019
- [7] K.A. Pascioni et Al., "Noise Reduction Potential of Phase Control for Distributed Propulsion Vehicles", *AIAA Scitech forum*, 2019
- [8] A. Patterson et Al., "Propeller Phase Synchronization for Small Distributed Electric Vehicles", *AIAA SciTech forum*, 2019
- [9] V.T. Valente, "Implementation of a Phase Synchronization Algorithm for Multirotor UAVs", *IEEE/AIAA 41st Digital Avionics Systems Conference*, 2022
- [10] V.T. Valente, "An Experimental Evaluation of an Electronic Rotor Phase Synchronization System for Multirotor Aircraft Noise Control", *Vertical Flight Society's 80th Annual Forum*, 2024
- [11] B. Smith et Al., "An Assessment of Multi-copter Noise in Edgewise Flight", *Vertical Flight Society's 77th Annual Forum & Technology Display*, 2021
- [12] B. Smith et Al., "A Comparison of Tonal Noise Characteristics of Large Multicopters with Phased Rotors", *Journal of the American Helicopter Society*, 2023
- [13] B. Smith et Al., "Quadcopter Noise Variation Due to Relative Rotor Phasing", *Vertical Flight Society's 80th Annual Forum & Technology Display*, 2024
- [14] S. Guan et Al., "Noise attenuation of quadrotor using phase synchronization method", *Aerospace Science and Technology* 118, 2021
- [15] A. Kostek et Al., "Experimental investigation of UAV rotor aeroacoustics and aerodynamics with computational cross-validation", *CEAS Aeronautical Journal*, 2023
- [16] E.J. Alvarez et Al., "Rotor-on-Rotor Aeroacoustic Interactions of Multirotor in Hover", *Journal of the American Helicopter Society*, 2020

BIBLIOGRAPHY

- [17] F. Farassat, "Theory of Noise Generation from Moving Bodies with an Application to Helicopter Rotors", *NASA TR-R-451, Langley Research Center*, 1975
- [18] F. Farassat, "Derivation of Formulations 1 and 1A of Farassat", *NASA TM-2007-214853, Langley Research Center*, 2007
- [19] M.J. Lighthill, "On Sound Generated Aerodynamically: I. General Theory", *Proceeding of the Royal Society of London, Series A Volume 211*, 1952
- [20] J.E. Ffowcs Williams and D.L. Hawkings, "Sound Generation by Turbulence and Surfaces in Arbitrary Motion", *Philosophical Transactions of the Royal Society of London, Series A, Vol. 264*, 1969
- [21] J. Yin et Al., "Numerical studies on small rotor configurations with validation using acoustic wind tunnel data", *CEAS Aeronautical Journal*, 2023
- [22] J. Yin, F. Le Chuiton, M. Schmidt, T. Schwarz, "DLR Free Wake Unsteady Panel Method (UPM): Userguide", *DLR Institute of Aerodynamics and Flow Technology, Helicopter Division (AS-HEL)*, 2024
- [23] J. Yin, B.G. van der Wall, G.A. Wilke, "Investigation of a simplified aerodynamic modeling technique for noise predictions using FW-H propagation", *CEAS Aeronautical Journal*, 2016
- [24] J. Yin, J. Delfs, "Improvement of DLR rotor aeroacoustic code (APSIM) and its validation with analytic solution", *29th European Rotorcraft Forum*, 2003
- [25] P. Kunze, "A Panel Free-Wake Code with Boundary Layer Method for Helicopter Simulations", *45th European Rotorcraft Forum*, 2019
- [26] S.R. Ahmed and V.T. Vidjaja, "Unsteady Panel Method Calculation of Pressure Distribution on BO105 Model Rotor Blades", *Unsteady Panel Method Calculation of Pressure Distribution on BO105 Model Rotor Blades*, 1998
- [27] J. Yin, "Prediction - and its Validation - of the Acoustics of Multiblade Rotors in Forward Flight Utilising Pressure Data from a 3-D Free Wake Unsteady Panel Method", *20th European Rotorcraft Forum*, 1994
- [28] J. Yin, "Simulation of Tail Rotor Noise Reduction and Comparison with HeliNovi Wind Tunnel Test Data", *67th Annual Forum of the American Helicopter Society*, 2011
- [29] J. Yin and S.R. Ahmed, "Helicopter Main-Rotor/Tail-Rotor Interaction", *Journal of the American Helicopter Society*, 2000
- [30] J. Yin and S.R. Ahmed, "Treatment of Unsteady Rotor Aerodynamics Using a 3D Panel Method", *DLR technical report IB 129-94/21*, 1994
- [31] A. Segalini, P.H. Alfredsson, "A simplified vortex model of propeller and wind-turbine wakes", *Journal of Fluid Mechanics*, 2013
- [32] H. Lee et Al., "Review of vortex methods for rotor aerodynamics and wake dynamics", *Advances in Aerodynamics*, 2022
- [33] D. Donnini, "VTOL Directional Noise Reduction via Rotor Phase Synchronization: A Numerical Trim Procedure and Flight Mechanics Investigation", *Alma Mater Studiorum Università di Bologna*, a.y. 2023/24
- [34] A. Chella, "Analytical tool development for sound directivity simulation and control in a multi-copter configuration", *Alma Mater Studiorum Università di Bologna*, a.y. 2023/24

BIBLIOGRAPHY

- [35] G.A. Wilke, "Aerodynamic Optimization of Helicopter Rotor Blades using Variable Fidelity Methods", *PhD Thesis, Braunschweig Technical University*, 2017
- [36] H.H. Hubbard, "Aeroacoustics of Flight Vehicles: theory and practice, Volume 1: Noise Sources", *NASA Reference Publication 1258*, 1991
- [37] M. Blunt and B. Rebbechi, "Propeller Synchrophase Angle Optimisation Study", *13th AIAA/CEAS Aeroacoustics Conference*, 2007
- [38] FAA Federal Aviation Administration, "Noise Standards: Aircraft Type and Airworthiness Certification, Title 14 CFR Part 36", available at: <https://www.ecfr.gov/current/title-14/chapter-I/subchapter-C/part-36/appendix-Appendix%20J%20to%20Part%2036>
- [39] Jordi Pons-Prats et Al., "On th understanding of the current status of urban air mobility development and its future prospects: Commuting in a flying vehicle as a new paradigm", *Transportation Research Part E*, 2022
- [40] J. Su et Al., "eVTOL Performance Analysis: A Review from Control Perspectives", *IEEE Transactions on Intelligent Vehicles*, 2024
- [41] D.R. Vieira, "Electric VTOL aircraft: the future of urban air mobility", *Sustainable Aviation vol.5*, 2019
- [42] A. Bacchini, " Electric VTOL Configurations Comparison", *Aerospace*, 2019
- [43] Vertical Flight Society, "eVTOL News", available at: <https://evtol.news/>
- [44] Volocopter, "Volocity Urban Air Taxi", available at: <https://www.volocopter.com/en/solutions/volocity>
- [45] Jetson, "Jetson One: the first affordable eVTOL on the market", available at: <https://jetson.com/jetson-one>
- [46] Airbus, "CityAirbus NextGen: Airbus' electric vertical takeoff and landing (eVTOL) prototype", available at: <https://www.airbus.com/en/innovation/energy-transition/hybrid-and-electric-flight/cityairbus-nextgen>
- [47] Vertical Aerospace, "VX4 tilt-rotor eVTOL", available at: <https://vertical-aerospace.com/meet-the-vx4/>
- [48] Joby Aviation, "Joby s4 tilt-rotor eVTOL", available at: <https://www.jobyaviation.com/>

A | Appendix

A.1 Results of the aerodynamic simulations in forward flight

This appendix contains some results of the unsteady panel method (UPM) simulations performed in the forward flight optimization study of chapter 5. Due to time constraints, further analysis dedicated specifically to the aerodynamics of the multirotor and their effect on noise emission were not included in this work, but relevant data is reported here for completeness.

In figure A.1 and A.2 we find a snapshot of the rotor wakes in the forward flight condition described in table 5.1. The wakes from the front and back rotors of one side were colored differently to distinguish them.

In figure A.3 and A.4 are reported the disc contour plots for loading and inflow on the rotors of the two configurations. The normal force coefficient C_n refers to the component of the blade sectional force parallel to the rotor axis, or perpendicular to the rotor disc. $C_n M^2$ is the normal force coefficient multiplied by the local Mach number squared, which results in adimensionalizing w.r.t. the speed of sound and not the local flow speed, in order to confront coefficients from various radial stations which experience largely different flow velocities. The distribution of loading ($C_n M^2$) and its derivative around the azimuth are closely related to the sound emission due to the time differentiation in the Farassat equation 2.44 for the rotor loading noise.

We note how the quad-rotor exhibits more rotor-to-wake interaction, this is mainly due to the different geometry between configurations:

- i) in the quad-rotor configuration the aft rotors are closer to the front ones.
- ii) the hexa-rotor generates more drag due to the increased rotor number, thus requires a higher pitch down angle.

Non the less, for a flight velocity of 28.33m/s the interactions are modest for both the configurations.

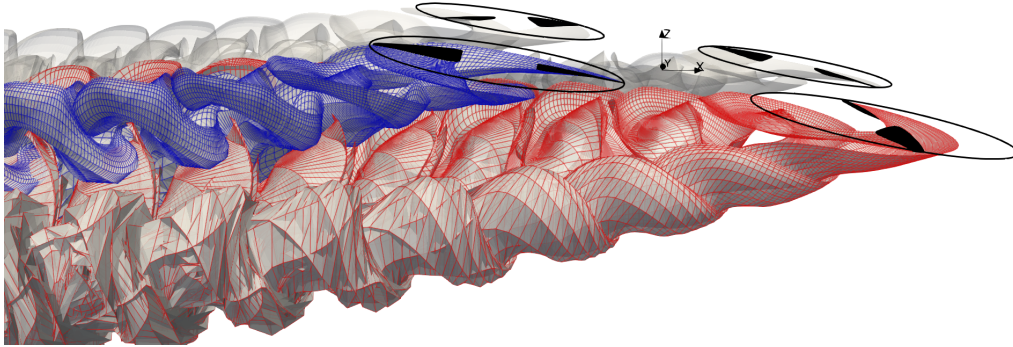


Figure A.1: Snapshot of the calculated free-wake of the quad-rotor configuration in level forward flight, with phase vector $\Delta\Psi = [0, 90, -45, -45]$ optimized for noise reduction in the front ground region. The wakes are colored to distinguish them from one another and the tip-path-planes of the rotors are indicated by black circles for clarity. Flight direction is from left to right. The axis represent the local horizontal reference frame.

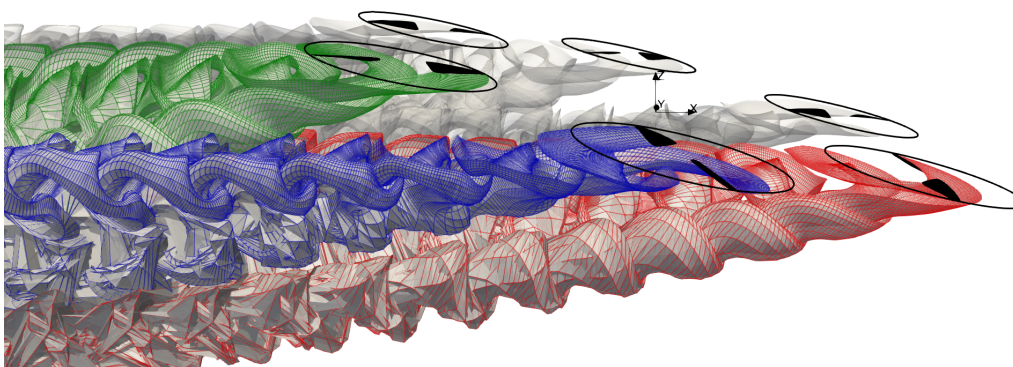
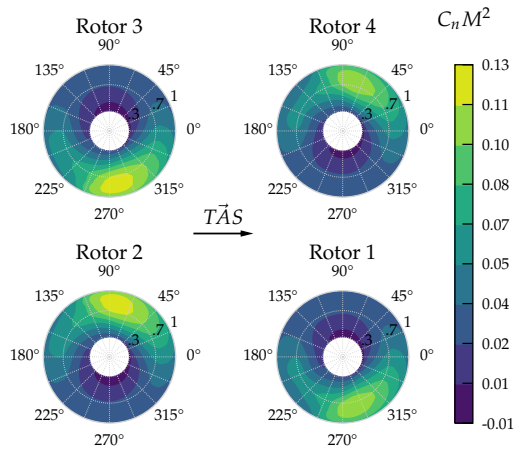
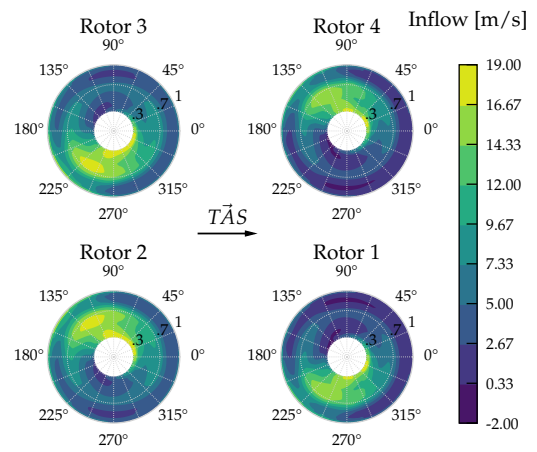


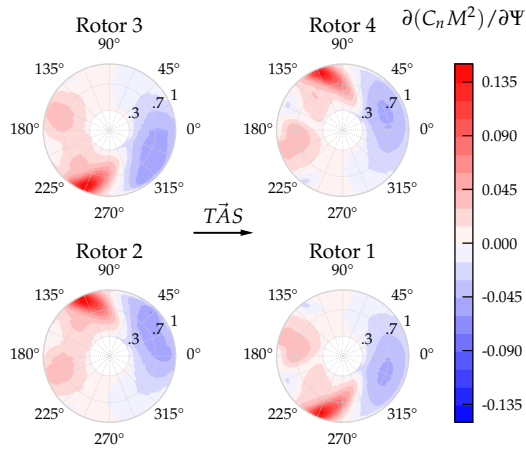
Figure A.2: Snapshot of the calculated free-wake of the hexa-rotor configuration in level forward flight, with phase vector $\Delta\Psi = [0, -18, -57, 54, -43, 58]$ optimized for noise reduction in the front ground region. The wakes are colored to distinguish them from one another and the tip-path-planes of the rotors are indicated by black circles for clarity. Flight direction is from left to right. The axis represent the local horizontal reference frame.



(a) Normal force coefficient over the radius and the azimuth of rotors, at the last rotation.

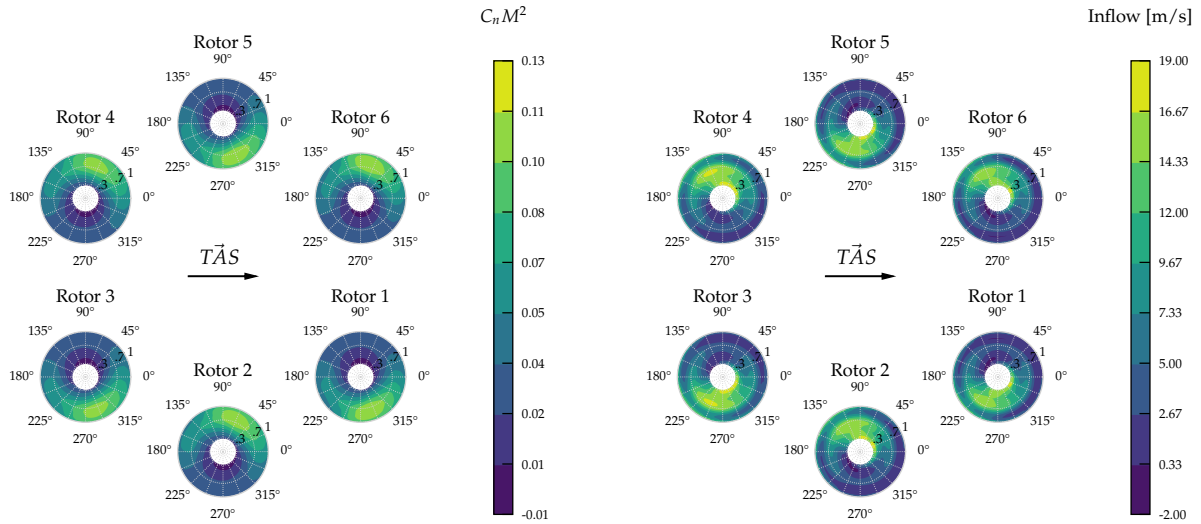


(b) Inflow velocity over the rotor discs at the last rotation.



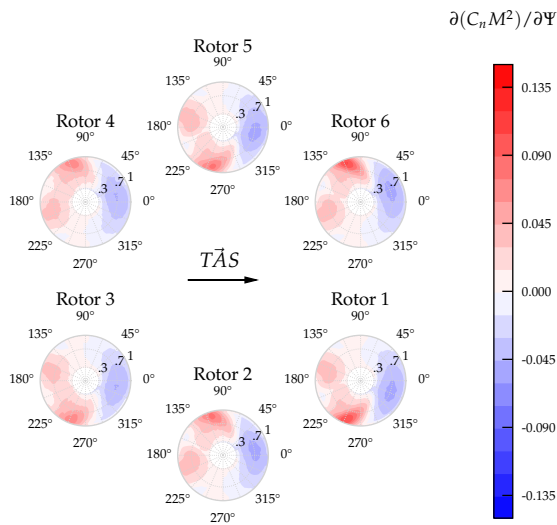
(c) Derivative of the normal force coefficient w.r.t. the azimuth.

Figure A.3: Disc plot contours representing loading and inflow on the rotors for the quad-rotor configuration in level forward flight, with phase vector $\Delta\Psi = [0, 90, -45, -45]$ optimized for noise reduction in the front ground region.



(a) Normal force coefficient over the radius and the azimuth of rotors, at the last rotation.

(b) Inflow velocity over the rotor discs at the last rotation.



(c) Derivative of the normal force coefficient w.r.t. the azimuth.

Figure A.4: Disc plot contours representing loading and inflow on the rotors for the hexa-rotor configuration in level forward flight, with phase vector $\Delta\Psi = [0, -18, -57, 54, -43, 58]$ optimized for noise reduction in the front ground region.